

ENVIRONMENTAL APPLICATIONS OF HYPERSPECTRAL ANOMALY AND
TARGET DETECTION ALGORITHMS

A THESIS SUBMITTED TO
THE GRADUATE SCHOOL OF NATURAL AND APPLIED SCIENCES
OF
MIDDLE EAST TECHNICAL UNIVERSITY

BY
HİLAL SOYDAN

IN PARTIAL FULFILLMENT OF THE REQUIREMENTS
FOR
THE DEGREE OF DOCTOR OF PHILOSOPHY
IN
MINING ENGINEERING

DECEMBER 2017

Approval of the thesis:

**ENVIRONMENTAL APPLICATIONS OF HYPERSPECTRAL ANOMALY
AND TARGET DETECTION ALGORITHMS**

submitted by **HİLAL SOYDAN** in partial fulfillment of the requirements for the degree of **Doctor of Philosophy in Mining Engineering Department, Middle East Technical University** by,

Prof. Dr. Gülbin Dural Ünver
Dean, Graduate School of **Natural and Applied Sciences** _____

Prof. Dr. Celal Karpuz
Head of Department, **Mining Engineering** _____

Prof. Dr. Celal Karpuz
Supervisor, **Mining Engineering Department, METU** _____

Dr. Alper Koz
Co-supervisor, **Center for Image Analysis, METU** _____

Examining Committee Members:

Prof. Dr. Aydın Alatan
Electrics and Electronics Eng. Dept., METU _____

Prof. Dr. Celal Karpuz
Mining Engineering Dept., METU _____

Prof. Dr. Bahtiyar Ünver
Mining Engineering Dept., Hacettepe University _____

Assist. Prof. Dr. Seniha Esen Yüksel
Electrics and Electronics Eng. Dept., Hacettepe University _____

Prof. Dr. Yasemin Yardımcı Çetin
Informatics Institute, METU _____

Date: 13/12/2017

I hereby declare that all information in this document has been obtained and presented in accordance with academic rules and ethical conduct. I also declare that, as required by these rules and conduct, I have fully cited and referenced all material and results that are not original to this work.

Name, Last name: Hilal Soydan

Signature :

ABSTRACT

ENVIRONMENTAL APPLICATIONS OF HYPERSPECTRAL ANOMALY AND TARGET DETECTION ALGORITHMS

Soydan, Hilal

Ph.D, Department of Mining Engineering

Supervisor: Prof. Dr. Celal Karpuz

December 2017, 128 pages

The objective of this thesis study is to understand the capacity of hyperspectral anomaly detection and target detection algorithms for contamination mapping, with a focus on developing a new methodology for environmental problems related to coal mining operations. Considering the data availability, specific chemical structure and reflectance properties as well as being one of the common contaminants in mining operations, hydrocarbon induced problems are studied for water and soil medium separately. Having developed the algorithms and implemented new methodologies, the research is focused on understanding the potential of anomaly detection for identifying topographical changes in temporal manner and mapping secondary iron minerals related to acid mine drainage, which is a commonly encountered problem in coal mine sites. On the top of the developed expertise of the definitions and mathematical implications of anomaly and target detection algorithms, soils' spectral features with regard to their chemical and physical relation is elaborated. The research contributes to literature by presenting the success of hyperspectral anomaly and target analysis algorithms to differentiate oil slicks in water medium. In addition to the capacity of anomaly and target analysis to determine hydrocarbon induced alterations, unmixing techniques are also proved to resolve the characteristic features in relation with surface manifestations of hydrocarbon seeps by means of multispectral data sets.

This novel approach is adapted to determine the iron oxide mineral contents associated with acid mine drainage problems in mining areas with one of the latest imaging missions of European Space Agency (ESA), Sentinel-2. The theoretical background and experiments on synthetic data to map iron related features so far are combined to analyze the downloaded Sentinel-2 image with the help of the developed methodologies.

Keywords: Hyperspectral, hydrocarbon, target detection, unmixing, acid mine drainage

ÖZ

HİPERSPEKTRAL ANOMALİ VE HEDEF TESPİTİ ALGORİTMALARININ ÇEVRESEL UYGULAMALARI

Soydan, Hilal

Doktora, Maden Mühendisliği Bölümü

Tez Yöneticisi: Prof. Dr. Celal Karpuz

Aralık 2017, 128 sayfa

Bu tez çalışmasında, kömür madenciliği ile ilgili çevresel problemleri tespit ve çözümlenmeye yönelik olarak, hiperspektral anomali tespiti ve imzaya dayalı tespit algoritmalarının kirlilik haritalama potansiyelinin değerlendirilmesi amaçlanmıştır. Veri elde edilebilirliği, spesifik kimyasal yapısı ve yansıma özellikleri göz önüne alınarak, madencilik operasyonlarında da sıklıkla kirliliğe neden olan hidrokarbon kaynaklı sorunlar, hem su hem de toprak ortamında değerlendirilmiştir. Geliştirilen yöntemler çerçevesinde, anomali tespit algoritmaları, madencilik faaliyetleri ile ilişkili olarak, zamansal anlamda topoğrafya değişimlerini tespit etmede ve kömür madenlerinde sıkça karşılaşılan asit kaya drenajı potansiyelinin belirlenmesi amacı ile ikincil demir minerallerinin haritalanmasında kullanılmıştır. Araştırma öncelikle hiperspektral anomali ve hedef tespit algoritmalarının su üzerinde bulunan ince petrol tabaklarının belirleme başarısını ortaya koymuştur. Bununla birlikte, anomali ve hedef tespit algoritmalarının hidrokarbon etmenli alterasyonları tespit etme kapasitesine ek olarak, hiperspektral ayrıştırma yöntemlerinin sözü edilen yüzeysel değişimleri multispektral uydu görüntüleri aracılığı ile ortaya çıkarmadaki performansını açığa çıkarmıştır. Bu yenilikçi yaklaşım Avrupa Uzay Ajansı'nın en yeni uydu görüntülerinden olan Sentinel 2 üzerinde uygulanarak, demir oksitli minerallerin tespit

edilmesinde kullanılmıřtır. řimdiye kadar geliřtirilen teoriler ve sentetik grntler zerinde denenen yntemler deęerlendirilerek, bu yntemler kmr madeni alıřma alanına ait gerek grntler zerinde uygulanmıřtır.

Anahtar Szckler: Hiperspektral, hidrokarbon, hedef tespiti, hiperspektral ayrıřtırma, asit kaya drenajı

To My Family

ACKNOWLEDGMENTS

My doctoral research consists of the inquiries of applicability and efficiency of several anomaly and target detection methods on contamination mapping. This effort required expertise and guidance of several parties from these distinct yet related academic areas, RS/GIS, Mining, Geochemistry, Sustainability and so on. I would like to express my deepest gratitude to Prof. Dr. Şebnem Düzgün who had supervised my thesis from the beginning to the very last months to its completion. It was only for her meticulous guidance, orientation and encouragement, I could dare to initiate and complete this study. In addition to her academic competence, her exceptional character of bringing researchers together enabled me accessing these diverse skills and guidance from collaborators of research projects we were involved in. This is the part I want to express my second but not the lesser gratitude and appreciation to my Co-supervisor Dr. Alper Koz who is a mentor, advisor and friend for me during this study. This thesis is written by means of his close supervision, criticism and support and his extraordinary expertise in image analysis. Not only about the specializations of the subject matter, had he also made a perfect example for me, of a rigorous researcher and a hardworking-fun-decent person.

I am also grateful to Prof. Dr. Yasemin Yardımcı Çetin, for her guidance, help, and support throughout every phase of the study.

I would like to thank the Head of Department Prof. Dr. Celal Karpuz, for his kind efforts to help me complete my thesis during the administrative processes after the very recent leave of my supervisor and his undertaking the supervisor duties during the defense process.

I must mention the significance of the constructive and supporting attitude of my co-worker and friends Onur Gölbaşı, Esra Nur Tanrıseven and Okan Bilge Özdemir. I am

thankful to my friend Ulaş Canatalı for his help in preparing the text of the dissertation, which was a lifesaver at the final and most stressful last stages of this story.

I am also grateful to Fulbright Commission for the scholarship at Lamont-Doherty Earth Observatory/ in Columbia University, and experiencing NYC, during my PhD study.

This study is supported by the Scientific and Technological Research Council of Turkey (Project Number: 115M712).

TABLE OF CONTENTS

ABSTRACT	v
ÖZ.....	vii
ACKNOWLEDGMENTS.....	x
TABLE OF CONTENTS	xii
LIST OF TABLES	xiv
LIST OF FIGURES.....	xv
LIST OF ABBREVIATIONS	xvii
CHAPTERS	
1 INTRODUCTION.....	1
1.1 The Basics of Hyperspectral Imaging Spectroscopy.....	9
1.2 Hyperspectral Sensing and Its Remote Sensing Applications.....	15
1.3 Spectral Properties of Soils.....	17
1.4 Environmental Applications of Hyperspectral Analysis	21
1.4.1 Hyperspectral Sensing of Hydrocarbon-Induced Anomaly Detection.....	22
1.4.2 Hyperspectral Sensing of Coal Mining Induced Contaminations.....	29
2 HYPERSPECTRAL IMAGE ANALYSIS ALGORITHMS.....	37
2.1 Hyperspectral Anomaly and Target Detection Methods	37
2.1.1 Anomaly Detection Algorithms	41
2.1.2 Signature Based Detection Algorithms	42
2.2 Unmixing Algorithms.....	45
2.2.1 Fast Autonomous Spectral Endmember Determination (N-FINDR)...	46
2.2.2 Vertex Component Analysis (VCA)	47
2.2.3 Minimum Volume Simplex Analysis (MVSA)	48
2.2.4 A Simplex Identification via Split Augmented Lagrangian (SISAL) ..	50
3 APPLICATIONS OF ANOMALY AND TARGET DETECTION ALGORITHMS TO DETERMINE OIL SPILLS.....	53
3.1 Utilized Data and Methodology	54
3.2 Experimental Results and Comparisons	56
4 MAPPING HYDROCARBON INDUCED ANOMALIES WITH HYPERSPECTRAL TECHNIQUES.....	63

4.1	Utilized Data and Methodology	65
4.2	Experimental Results.....	66
5	MAPPING TOPOGRAPHICAL ANOMALIES FOR AN ABANDONED COAL MINE.....	75
5.1	Utilized Data and Methodology	77
5.2	Experimental Results and Comparisons.....	78
6	MAPPING SECONDARY IRON MINERALS FOR DETERMINING ACID MINE DRAINAGE POTENTIAL FOR AN ABANDONED COAL MINE.....	85
6.1	Utilized Data and Methodology	90
6.1.1	Validation with ASD Library Spectra and Laboratory Analysis	92
6.2	Experimental Results of Implementation of Unmixing Algorithms	97
7	CONCLUSION AND RECOMMENDATIONS.....	107
7.1	Conclusions	107
7.2	Recommendations	110
	REFERENCES.....	113
	APPENDICES	
A.	SISAL ALGORITHM - REPRESENTATIVE ABUNDANCE MAPS FOR HYDROCARBON MICROSEEPAGE – (ASTER).....	123
B.	TRACE ELEMENT LEVELS OF COLLECTED SOIL SAMPLES.....	125
	CURRICULUM VITAE	127

LIST OF TABLES

TABLES

Table 4-1 Error terms calculated using the reference signature and extracted endmembers with SAM algorithm	69
Table 4-2 Root Mean Square Error Metrics between SISAL and other algorithms ..	71
Table 6-1 Sentinel 2A Spectral Band Properties.....	86
Table 6-2 XRD Laboratory Experiment Results.....	95
Table 6-3 Spectral Angle Errors [Extracted Endmembers (SISAL) and USGS Hematite Spectra].....	98
Table 6-4 Spectral Angle Errors [Extracted Endmembers (MVSA) and USGS Hematite Spectra].....	98
Table 6-5 Minimum Wavelengths For Extracted Endmembers.....	100

LIST OF FIGURES

FIGURES

Figure 1-1 Electromagnetic Spectrum (EMS) (Modified from Velez Reyes, 2007).	11
Figure 1-2 Optical Infrared Region with Atmospheric Transmission Window (Irradiance, 2017).....	12
Figure 1-3 Atmospheric transmission window with utilized images in this study	12
Figure 1-4 Hyperspectral Data Cube and Spectral Signature (Elowitz, 2015)	13
Figure 1-5 Spectral signatures of some minerals	14
Figure 1-6 Hyperspectral Data Cube and Reflectance Signature Representation.....	16
Figure 1-7 Wavelength positions related to some constituents of soil (Viscarre Rossel and Chen, 2011)	19
Figure 1-8 Soil Spectral Reflectance Curves (Stoner and Baumgardner, 1981) A: organic affected soils, B: minimally altered soils, C: iron-affected soils, D: iron dominated soils, E: organic dominated soils.....	19
Figure 1-9 Mineralogical Composition of Soils, illustrating relative abundance of each mineral (Modified from Irons, 1989).....	20
Figure 1-10 Generalized form of soil and sediment geochemical alterations (Schumacher, 1996)	22
Figure 1-11 Hydrocarbon Migration Process (Modified from (Schumacher, 1996) .	24
Figure 1-12 Hydrocarbon Index (Kuhn et al., 2004)	27
Figure 1-13 a) Absolute spectra of powdered samples of macromolecular organic bearing minerals (COAL01 [coal], Oils10(Oil Shale), TAR17 [Oil sand], CTE191 [Coal tar] (Cloutis et al., 1994)	31
Figure 1-14 Photographs Taken from the coal mine sites of Acid Rock Drainage (Çanakkale-Balıkesir) (Twinning Project Report, 2014).....	34
Figure 1-15 Open pit area, Çankırı, Ovacık Mine (Soydan, 2013).....	36
Figure 1-16 Acid Mine Drainage in Çankırı, Ovacık Mine (Soydan, 2013)	36
Figure 2-1 Double-concentric window for spectral anomaly detection.....	39
Figure 3-1 AVIRIS image and anomaly detection algorithm outputs (Zare-Baghbidi and Humayouni, 2013).....	56
Figure 3-2 SPECTIR image and anomaly detection algorithm outputs (Baghbidi and Humayouni, 2013)	57
Figure 3-3 Algorithm Results on SPECTIR Imagery a) True Color Composite b) Global RX c) Local RX d) Gaussian RX e) SMF f) DTDCA	57
Figure 3-4 Algorithm Results on AVIRIS Imagery a) True Color Composite b) Global RX c) Local RX d) Gaussian RX e) SMF f) DTDCA	58
Figure 3-5 SMF (left image) and DTDCA (right image) Results on (a) SPECTIR Imagery and.....	59
Figure 3-6 DTDCA Error Metrics (a) SPECTIR (b) AVIRIS	60
Figure 3-7 Oil bearing pixels, shown in white color, after thresholding operation (a) SPECTIR (b) AVIRIS.....	60

Figure 3-8 Radiance signatures of pixels with and without oil content (SPECTIR) .	61
Figure 3-9 Radiance signatures of pixels with and without oil content (AVIRIS)....	62
Figure 4-1 a) Spectral Signatures of Hydrocarbon Microseepage Samples Collected with ASD b) Signature Resampled to ASTER Spectral Resolution	67
Figure 4-2 Signature Based Target Detection Algorithm Outputs.....	67
Figure 4-3 Endmember outputs corresponding the microseepage regions	68
Figure 4-4 Abundance fractions corresponding to microseepage endmember of each unmixing algorithm.....	70
Figure 4-5 The algorithm outputs a) Crosta b) SMF c) DTDCA d)VCA e)MVSA f)SISAL	71
Figure 5-1 The Flowchart of the Methodology	78
Figure 5-2 RX Anomaly Algorithm Outputs in Multi-Temporal Landsat Images	80
Figure 5-3 a) True Color Image - 2011 b) Global RX Output with high score anomaly pixels- 2011	81
Figure 5-4 ROC Curves of Anomaly Detection Outputs	82
Figure 5-5 Landsat True Color (321) Image and Unsupervised Change Detection Output (Taşkesen, 2017)	83
Figure 6-1 Hematite Spectra and 900 nm Absorption Feature for Different Grain Sizes (Clark, 1999).....	88
Figure 6-2 Spectral Fingerprints of Secondary Iron Minerals (Clark, 1999).....	88
Figure 6-3 Flowchart of the Methodology	92
Figure 6-4 Hematite Spectral Signature with Fitted Model	93
Figure 6-5 ASD Spectra of Soil Samples on which XRD Analysis Performed.....	94
Figure 6-6 XRD Results of Soil Samples.....	95
Figure 6-7 The Parabola Model Fitted to ASD Spectral Samples of Soils	96
Figure 6-8 Hematite spectra resampled to Sentinel-2 resolution with the endmembers with minimum errors (Left column: Overall spectrum, Right column: Iron absorption bands, 745-945 nm).....	99
Figure 6-9 Parabola fitting techniques for capturing absorption feature due to iron content for each endmember Left Column: Sisal Endmembers, Right Column: Mvsa Endmembers a) 5-m b) 30-m c) 60-m.....	99
Figure 6-10 Mine layout with total iron content	102
Figure 6-11 Enrichment factors of measured heavy metals.....	103
Figure 6-12 Unmixing algorithm output plots (a) 5-m (b) 30-m(c) 60-m	103
Figure 6-13 Abundance Maps Representing the Iron Bearing Spectral Endmember (First Row: 5-m, Second Row: 30-m, Third Row: 60-m).....	104

LIST OF ABBREVIATIONS

EMS	Electromagnetic Spectrum
VNIR	Visible Near Infrared
SWIR	Short Wave Infrared
SISAL	A Simplex Identification via Split Augmented Lagrangian
MVSA	Minimum Volume Simplex Analysis
VCA	Vertex Component Analysis
N-FINDR	Fast Autonomous Spectral Endmember Determination
SMF	Spectral Match Filter
SAM	Spectral Angle Mapping
DTDCA	Desired Target Detection Algorithm
RX	Reed-Xioli
AMD	Acid Mine Drainage
XRD	X-Ray Diffraction
ICP	Inductive Coupled Plasma
ASD	Analytical Spectral Devices
NDVI	Normalized Difference Vegetation Index

CHAPTER 1

INTRODUCTION

Hyperspectral imaging is practically remote sensing application of near infrared spectroscopy via airborne or satellite platforms. The capability of the sensors to capture hundreds of contiguous bands ensures that a detailed spectrum for each pixel can be derived, which then will be utilized for identification of materials on Earth's crust. The hyperspectral images are usually collected between 400 – 2500 nm in electromagnetic spectrum, due to the high atmospheric transmittance percentages in that specified region. In spite of the challenges on data acquisition, storage, correction in mid-seventies, the advances on the imaging platforms have promoted practical and feasible means to analyze the environment in several contexts so far. The extant literature of hyperspectral imaging or imaging spectrometry covers agricultural applications, military applications, mineral mapping, geological applications, marine applications and so forth. Remote sensing analysis, including exploitation of both multispectral & hyperspectral imageries, have been successful to determine environmental problems from different perspectives by means of the advances on earth observation satellites. In the recent two decades, with its potential of spectrally & spatially high-resolution image acquisition, hyperspectral images have especially been examined to develop new algorithms to determine problematic regions.

Hyperspectral target detection methods have until now progressed mainly on two paths in remote sensing research. The first approach, anomaly detection methods, use the difference of a local region with respect to its neighborhood to analyze the image without using any prior information of the searched target. The second approach on the other hand uses a previously obtained signature of the target, which uniquely represents the target's reflection characteristics with respect to the spectral wavelengths. The signature of the target is matched with the pixels of the acquired image to decide on the existence and location of the searched target. These two

approaches provide crucial information to detect environmental implications of pollution in different mediums.

Contaminations are of a paramount importance to both environment and human health welfare in relation to their relative quantities and distribution in the existent surrounding. How these contamination agents dissolved or spread in that ambient is greatly dependent on the chemical and physical properties. The environmental challenges due to high industrialization and the inevitable human interference accompanied with that, unveil overwhelming land, water and air problems worldwide. These ecosystems are strongly related/integrated with each other and they are endangered with the anthropogenic effects in developing countries as well as the highly industrialized ones. Regardless of the pollution agent, organic or inorganic, its influx to ecosystem changes the ambient medium despite the fact that it can't be visible at the surface. In fact, the invisible pollutions occurring subsurface are detected by tracking their surface manifestations or their impact on the existent vegetation, i.e. vegetation stress (Winkelmann, 2005).

In line with the above-mentioned information, Van Der Weerf and his colleges (2016) studies on the hydrocarbon contamination due to human induced activities as well as natural sources itself. Due to dynamic pressure differences, hydrocarbons migrate upwards from reservoirs to surface, inducing negative effects on the surrounding media. Some local pollutions because of migrated heavy hydrocarbons as well as upwelling gasses, light hydrocarbons, are pointed out as to their pollution potential in neighboring soil and water environment. Following their statement, the authors remarks the natural seepages not only being related to potential source of hazards, but also of an interest for hydrocarbon exploration as well (Van Der Weerf et al., 2016). Furthermore, considering the large-scale industrial operations, hydrocarbon contaminations can be faced with during production of crude oil from wells, transportation with pipelines or vehicles, leakage from underground storage tanks or simply accidents of vehicles transporting fuels in worldwide. The surface manifestations, of course, vary depending on the source of the contamination, such as

while a linear pattern can be observed for a pipeline leak, while point contamination can be observed in accidental oil spills or a halo shape is encountered for a natural seepage.

In his thesis study focused on fuel contaminations in soils, Winkelmann (2005) groups the sources of contamination as industrial facilities, mining areas, spill site and finally burial of wastes. In industrial facilities, as the operations are commenced, may be small amounts of pollutants are leaked to soil and water for longer durations, slowly altering the ambient conditions. Spill sites, on the other hand, are usually the locations where large amounts of contaminant agent is influxed in a very short time, typically as a result of an accident. In the case of mining areas, the potential of acid mine generation and heavy metal leaching dumps due to acidic environment, mostly in overburden dumps, causes the contamination of both soil and water in mining sites that requires costly and time-consuming rehabilitation activities. Finally, the waste burial scenes are referred as the landfills or burials including commercial, household or industrial wastes.

In the context of mining engineering applications, one of the foremost and abundant contamination type is known as Acid Mine Drainage (AMD) generation. According to the World Coal Association report (2015), Acid Mine Drainage (AMD) is defined as the metal rich water, which is product of successive chemical reactions between sulphur bearing minerals and water/oxygen. As the name implies, the water flow is acidic and it is generated by typically the exposed pyrite, a sulphur-bearing mineral, during coal mining activities. This acidic solution is generated mostly in the form of sulfuric acid, accompanied with high quantity of total dissolved solids and heavy metal ions that are leached from the surrounding minerals. This runoff penetrates the ecosystem through surface and underground water, endangering all living creatures around it. For the case of coal mining areas, as both the coal and host rock contains pyrite inherently, regardless of whether the operation is underground or open cast, the acid generating potential is considerably high, destroying natural groundwater regime and radically alters the nature of groundwater–surface water interactions. During the

course of mining operations, especially around underground openings, waste piles or open pit walls, or even after rehabilitation, the exposed pyrite can generate acidic solutions easily with a perpetual direct/indirect physiochemical process in the existence of rainwater or groundwater interaction (McCarthy, 2001; Keating, 2001, Singh, 2006). In addition to acid mine drainage potential, environmental problems regarding with polycyclic aromatic hydrocarbons (PAHs) in burnt and unburnt coal are takes part in the existing literature. Shafy and Mansour (2016) explains the natural sources of PAHs as open burning, natural losses or seepage of petroleum or coal deposits, and volcanic activities. These ubiquitous contaminants are related to incomplete combustion of organics like coal, oil, petroleum. Achten and Hofman (2009) state that there is a lack of literature about the native polycyclic sources of hydrocarbons in coals, even if exact source distribution is hardly possible. However, it is further elaborated in the study that PAH concentrations in coals depend on the original organic matter type together with temperature/pressure conditions during coalification. Ribeiro and his colleagues (2012) are also concentrated on coal waste material for identification of primary polycyclic aromatic hydrocarbon pollutants, proving the petrogenic contribution in unburned samples to total identified content, as an environmental contaminant.

According to a recent project conducted within the harmonization with European Union Legislations by Ministry of Environmental Affairs of Turkey reveals that, a wide-spread Acid Mine Drainage (AMD) problem is observed especially in visited lignite mines which are actually designated as in critical conditions. In the scope of the project, around 300 mine sites are reported to be visited, and several problems regarding with their current state of waste management requiring legislative action are identified. Although it is stated that geological factors might mitigate the AMD generation in some metal mines, it is emphasized that the problem remains as a highly problematic issue, specifically regarding with the coalmines. Considering the coal power plants are vital for Turkey's current and prospective energy policies, it is of a

great importance to match this demand with proper environmental improvement policies (Twinning Project Report, 2014).

In the extant literature of remote sensing applications for detecting contamination agents, reflectance signatures of aforementioned pollutants and their usage for determining the existing and potential contaminated areas has been investigated frequently. While Salem (2001) investigates the potential of hyperspectral images to determine oil spill methods in Chesapeake Bay, he emphasizes the spectral similarity of oil to materials with similar chemical compositions, such as coal. During his analysis, the spectral techniques resulted in a coal storage area in Maryland Power Stations, proving his conclusions. Cloutis (1994) also attempts to differentiate the spectral signatures of carbon bearing materials with near infrared spectroscopy. He compares four different macro-carbon bearing materials, i.e. oils shale, oil sand, coal tar, coal grinded to 2mm within the spectral interval of 0.3 – 2.3 micrometers. The reflectance spectrum of coal is described as red sloped, meaning starts to increase around 550 nm, similar with oil sand spectrum. However, he mentions the lack of absorption of oil shales. This observation is reasoned with the non-existent C-H bands, which is congruent with low H-C ratios. The study emphasizes the fact that as the degree of aromatization increases, the ultraviolet—visible absorption feature is observed to be broader and more intense, particularly when carbon content exceeds over 90 percent. Cloutis (2003), further elaborates his research with different coal samples, stating the fact that distinct absorption characteristics of coals appears only in lowest rank samples around 1.4, 1.9 and 2.1–2.6 micrometer region. Absorptions around 1.7 and 2.3-2.5 are attributed the organic combinations and overtone bands (C-H stretching). For the identification of polycyclic aromatic hydrocarbons, Izawa (2014) reports three diagnostic absorption features around 880 nm, 1145 nm and 1687 nm. To continue with acid mine drainage potential, secondary iron bearing minerals are typically utilized in the literature. Mielke et al. (2004) state that the most common secondary iron minerals, which are also associated with mine wastes and acid mine generation (i.e. goethite, hematite and jarosite) have also a minimum reflectance

absorption around 900 nm, which is explained in detail by Clark, 1999. The ubiquitous nature of iron oxides, hydroxides and sulfides make them special for researchers as well as their special characteristics in VNIR region. The larger grain sizes are reported to exhibit broader reflections together with a shift to longer wavelengths and saturation. The 900 nm absorption feature is emphasized as a common property as to iron bearing minerals, which is due to similar electronic absorption features in the visible and near-infrared region.

Traditional techniques for determining the potential contaminated regions requires determining existing risk factors, methodological sample collection and implementing the rehabilitation activities with monitoring activities (Winkelmann, 2005). Given the information above, this approach is time consuming, labor intensive and highly expensive, especially when the contamination is spread over vast areas. Here, near infrared spectroscopy and its remote sensing applications present a significantly efficient alternative, narrowing the contaminated regions to considerably smaller extents and serving as a cost effective tool. The analysis drastically decrease the area that is required for sample gathering, dropping the sample collection and analysis budgets significantly.

The objective of this thesis study is to understand the capacity of hyperspectral anomaly detection and target detection algorithms for contamination mapping, with a driving force on developing a new methodology for environmental problems related to coal mining operations. With the limitations of currently available data sets, similarities in chemical structure and reflectance properties as well as being one of the common contaminants in mining operations, hydrocarbon induced problems are studied for water and soil medium separately. Having developed the algorithms and implemented new methodologies, the research is focused on understanding the potential of anomaly detection methods for topographical change in the abandoned mine site study area and mapping secondary iron minerals related to acid mine drainage, which is a commonly encountered problem in coal mine sites.

Besides the developed expertise of the definitions and mathematical implications of anomaly and target detection algorithms, a comprehensive literature study on reflectance spectroscopy of soils and how their chemical and physical structure relate to diagnostic absorptions is completed for a better understanding. Along with these complementary endeavors, this study contributes to the literature as follows:

- It presents the success of hyperspectral anomaly and target detection algorithms to differentiate oil slicks in water medium. Both anomaly detection methods and target detection algorithms are proven to be successful to determine the oil contaminated pixels, even providing information about the content, establishing their potential for further studies.
- introduces the capacity of anomaly and target detection methods to determine hydrocarbon induced alterations with a novel methodology. Applications of hyperspectral detection techniques on multispectral data sets are recognized as a resourceful approach, specifically considering the hyperspectral image acquisition challenges and limitations.
- discloses the prospective of integrating signature based target detection methods with unmixing algorithms for alteration mapping by proposing the possibility to take advantage of collected ground truth signatures. Performance of the algorithms can be demonstrated based on generated error metrics for overall assessments.
- puts forward the capability of the latest imaging missions of European Space Agency (ESA), Sentinel-2, for mapping secondary iron minerals with near infrared spectroscopy, even for the case studies with small quantities. Unmixing and abundance mapping techniques are able to identify the iron-bearing endmember by means of comparisons with hematite reference spectra.

This dissertation consists of the following chapters:

- A comprehensive literature survey on the basic principles of infrared spectrometry ($0.4 \mu\text{m} - 2.5 \mu\text{m}$) and its remote sensing applications with a focus on anomaly and target detection methods, and environmental applications of hyperspectral imaging with a focus on hydrocarbon and mining induced anomalies (Chapter 1).
- A detailed information about utilized hyperspectral image analysis algorithms (Chapter 2): Hyperspectral Anomaly and Target Detection Algorithms (Chapter 2.1), Hyperspectral Unmixing Algorithms (Chapter 2.2).
- An application of anomaly and target detection algorithms to determine oil spill positions in Gulf of Mexico, by presenting the details about the methodology and utilized data sets (Chapter 3).
- A study on mapping hydrocarbon induced anomalies on soil surface by means of unmixing and target detection method, offering an approach for a complete performance evaluation (Chapter 4).
- An implementation of Reed-Xioli (RX) anomaly detector, to measure its ability to designate the topographical changes due to mining operations temporally (Chapter 5).
- An approach to produce secondary iron mineral maps for determining acid mine drainage potential and their relation for an abandoned coal mine by using Sentinel-2 data (Chapter 6).
- Conclusions and recommendations for applications of hyperspectral anomaly and target detection algorithms on contamination mapping and future research visions (Chapter 7).

1.1 The Basics of Hyperspectral Imaging Spectroscopy

Imaging spectroscopy is simply defined as the study focused on light, which is reflected or emitted from the materials, and its distinctive characteristics across the electromagnetic spectrum (EMS). Remote sensing is mainly concentrated on the scattered sunlight from the Earth's surface, providing invaluable and extensive information about the crust in a timely and cost effective manner. With the advancements in technology in the last two decades, digital imagers are able to collect simultaneous image patches with the same geometric pattern, capturing small areas subsequently, enabling to create large extent assembled imageries. Aside from the developing satellite technology, the proximal sensing techniques have also been utilized to collect laboratory or field samples from the test materials, presenting high spectral resolution data across a predetermined wavelength interval, usually between 0.4 to 2.4 micrometers. Recent advances in satellite systems have introduced cutting edge sensors, making available several high spectral-spatial resolution images for researchers to elaborate on (MicroImages, 2012).

In his study, Baumgardner (1986) describes the reflective optical radiation as the electromagnetic energy propagation within the defined wavelength interval of 0.4 – 3 micrometers. As in energy balance equation, once the incoming light interacts with the surface, the material absorbs some portion of incoming energy, while transmitting another. The remaining is the amount of radiation reflected from the surface of interest. That is, keeping the energy preservation in mind, the incoming radiation or energy is the sum of transmitted energy, absorbed energy and reflected energy from the interacted surface. The ratio of reflected radiation to total radiation is named as reflectance.

The same conditions are also viable for photons that might originate from the surface itself, which is called as emission. All materials emit photons, which are dependent on the same physical laws as optical radiation. When a photon interacts with a mineral surface, it might be reflected from the grains directly or refracted through the mineral

grains, resulting in a scattered output from the surface to the receiver. The absorption processes and their dependent mechanisms leads the researchers to acquire information about the materials chemical properties through the reflective or emitted light. In line with that information, the capability of the spectrometers to measure detailed information across a wider range in electromagnetic radiation presents a great knowledge to scientists to carry out extensive research opportunities (Clark, 1999). In Figure 1-1, electromagnetic spectrum is given along with the aforementioned energy regions.

The capacity of hyperspectral imaging sensors is dependent on four significant parameters namely spectral range, spectral sampling, spectral bandwidth and signal to ratio. Starting from the last, signal o ratio is simply related to noise created by the sensor itself and it is the ratio of the measured radiance to the noise due to instrument electronics. The spectral range is the wavelength interval through the measurements are conducted. In general, imaging spectrometry instruments take measurements that covers the 0.4 – 2.5 micrometer region and spectral sampling is actually the of data collection frequency on this defined range. The spectral sampling is critical for resolving the absorption parameters for the sample in interest. The last parameter, spectral bandwidth, stands for the spectral channel width that is also of a high importance for capturing subtle spectral details with the frequency of collecting neighboring spectral samples as well. As the bandwidth gets narrower, the more detailed the spectrum is resolved by the spectrometer.

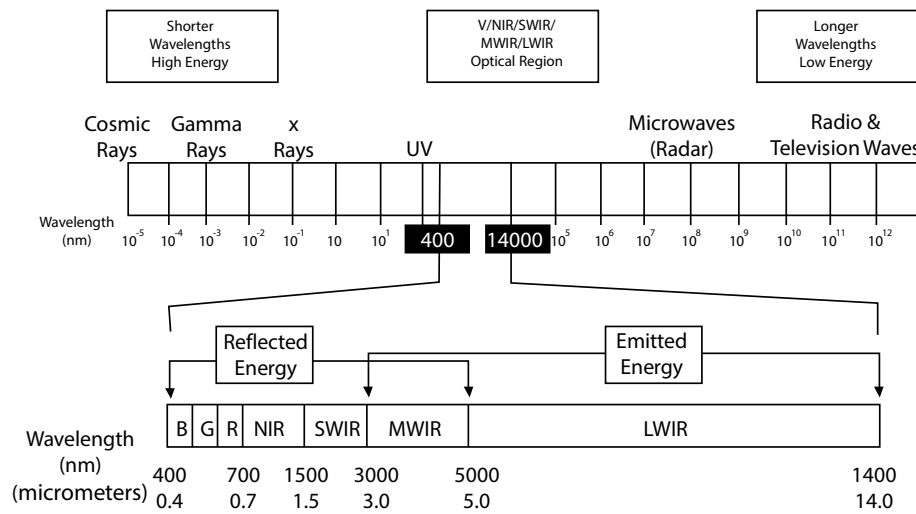


Figure 1-1 Electromagnetic Spectrum (EMS) (Modified from Velez Reyes, 2007)

As can be seen in Figure 1.1, the spectral ranges utilized in imaging spectroscopy, called as optical infrared region, can be grouped as follows:

- Visible: 0.4 to 0.7 μm ,
- Near infrared (NIR): 0.7 to 3.0 μm ,
- Mid-wave infrared (MIR): 3.0 to 5 μm ,
- Long-Wave infrared (LWIR): 5 μm to 14 μm

The hyperspectral imaging literature the region between ~ 0.4 to 1.0 - μm wavelength range is usually called as visible-near-infrared (VNIR), while the 1.0 to 2.5 - μm range is stated as short-wave infrared (SWIR) region, not in compliance with the general terms in use for these regions. The wavelength locations of the mentioned intervals are given on atmospheric transmission window for better understanding in Figure 1-2.

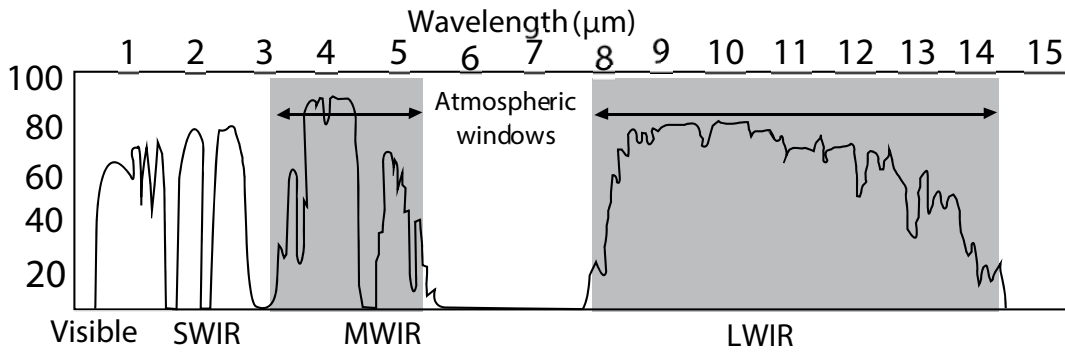


Figure 1-2 Optical Infrared Region with Atmospheric Transmission Window (Irradiance, 2017)

When the imaging from the airborne or satellite imageries are in consideration, it is imperative to account for the atmospheric absorption of the incoming radiation. The atmosphere consists of several gases with specific absorption features such as oxygen (0.76 μm), ozone (0.35 μm), carbon dioxide (2.01, 2.06 and 1.6 μm), blocking the radiation to be transmitted to earth surface. In addition to the gases, water is also another constituent preventing the light transmission through the atmosphere, i.e. 1.4 μm and 1.9 μm major water absorption bands. In short, each molecule owns a particular set of absorption characteristics in different parts of the electromagnetic spectrum, which results in only the windows outside the main absorption bands of the atmospheric constituents to be available for optical remote sensing purposes. Figure 1-3 illustrates the atmospheric transmission window together with the data sets utilized in the scope of this thesis (Clark, 1999).

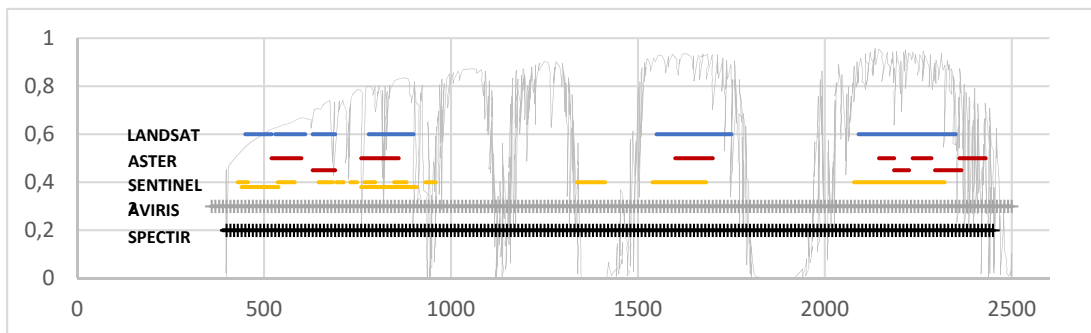


Figure 1-3 Atmospheric transmission window with utilized images in this study

Hyperspectral imaging provides the opportunity of not only qualitatively but also quantitatively evaluate the features related to interactions of light with both organic and/or inorganic materials. The resulting interaction is represented with a spectral signal, or signature, specified with contiguous energy levels within the defined spectral range. This signature demonstrates spectral information about the physical-chemical properties, which is strictly related to atomic, molecular and crystal structures, of the material in interest. The reflectance spectrum of an investigated material is defined as the overall radiation-matter interactions of its constituents within the field of view of the sensor in a defined wavelength region.

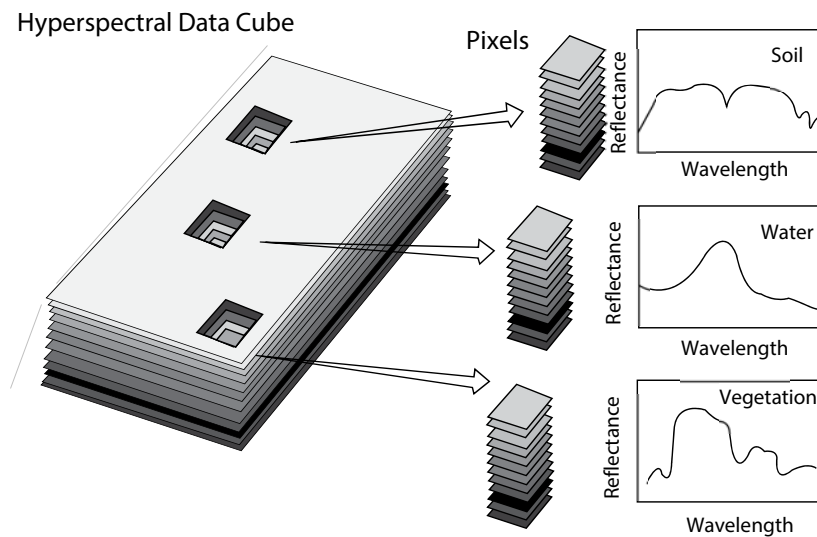


Figure 1-4 Hyperspectral Data Cube and Spectral Signature (Modified from Elowitz, 2015)

In the case of inorganic materials such as minerals, in addition to chemical composition, crystalline structure also is responsible for the spectral reflectance curve characteristics. In fact, certain absorption features are caused due to specific elements, their ionic state or chemical bond structure related to the crystalline structure (Microimages, 2017). In his study, Hunt (1977) states that the spectra of minerals are caused by several electronic and vibrational processes. He details these processes as ionic charge transfers, overtone or combination of vibrational transitions, crystal field effects and conduction band transitions in his research attempting to explain the

particular features at a specific wavelength location in the reflectance spectrum of a mineral. Spectral signatures of some minerals are given in Figure 1-5.

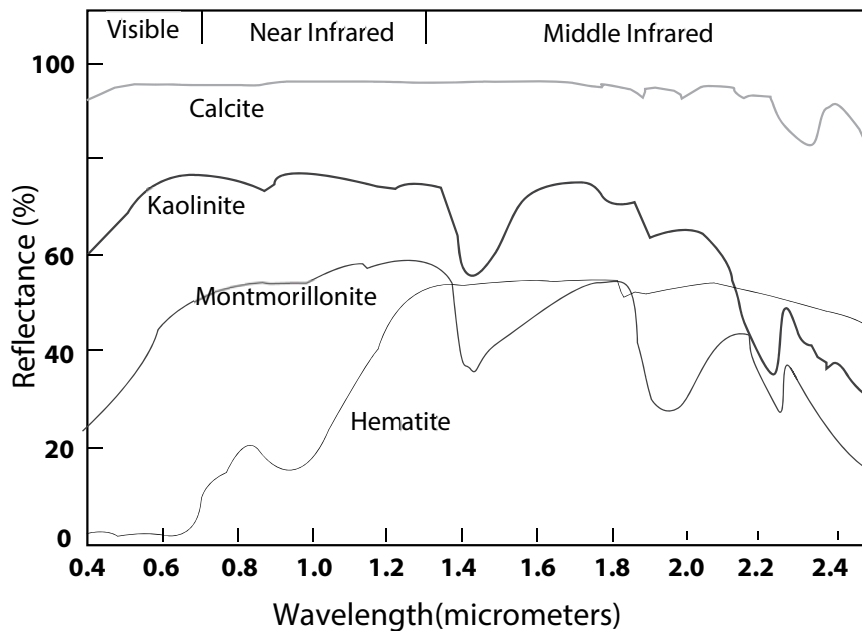


Figure 1-5 Spectral signatures of some minerals

Hunt and Ashley (1979) also specifies the electronic and vibrational processes as the reasons for band absorption, particularly related to each mineral. These processes mainly involve iron or hydroxyl group minerals, which are exclusively related to the mineral constituents of each investigated materials.

According to Hunt and Ashley (1979), the iron-bearing minerals produce absorption minimums in VNIR region, around 0.43, 0.65, 0.85, and 0.93 μm . Clay and water bearing minerals, on the other hand, exhibit absorption features in SWIR region, around 1.4, 1.75, 1.9, 2.2, and 2.35 μm due to vibrational processes. Minerals most abundantly presenting these absorption characteristics are listed as hematite, goethite, and alunite whereas jarosite, kaolinite, potassium micas, montmorillonite, and gypsum are mentioned as frequently possessing these features in their reflectance spectrum. All in all, the extant literature proves the viability and reliability of imaging

spectroscopy for mineral identification, especially the clay and iron bearing ones. As these minerals forms the altered rocks, remote sensing applications of imaging spectroscopy presents an invaluable resource in a time and cost efficient manner.

1.2 Hyperspectral Sensing and Its Remote Sensing Applications

Remote sensing platforms started to make use of near infrared spectroscopy at seventies, due to the capability of sensors to record the incoming radiation from the sun to Earth's crust between 0.2 – 2.5 micrometers, i.e. atmospheric transmission window. In spite of the challenges on data acquisition, storage, correction etc., the advances on the imaging platforms have promoted improved and feasible means to analyze the environment in variant contexts.

The transition of near infrared spectroscopy to airborne or satellite remote sensing platforms enabled the acquisition over several hundreds of high resolution contiguous bands rather than getting multispectral or panchromatic images from the Earth surface. Presenting such a high information, hyperspectral remote sensing data cubes provides not only spectral signatures for each pixel, but also makes available an image for each spectral band simultaneously. However, the systems comes with its challenges, such as data redundancy, data storage problems or complicated pre-processing operations depending on the remote sensing platform. What makes it rather difficult to utilize hyperspectral imaging instead of near infrared spectroscopy is the dynamic nature of the atmosphere and the investigated parameters that can't be controlled or optimized quite easily in comparison with laboratory environment. For this reason, ground truth signature collection is of a high importance for quantitative analysis of the target materials that additionally will help to analyze the remotely sensed data both qualitative and quantitative purposes (Winkelmann, 2005).

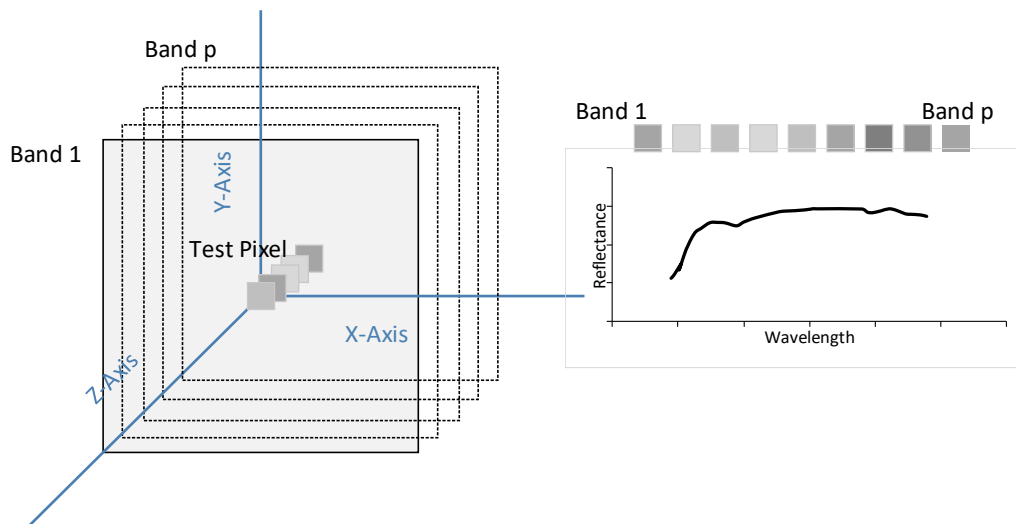


Figure 1-6 Hyperspectral Data Cube and Reflectance Signature Representation

Spectral signature is defined as the result of the interactions of light with organic and/or inorganic materials, characterized by sequences of recorded energy values in a defined wavelength interval with the spectral sampling interval of the investigated sensor (Seranti and Bonifazi, 2017). The collected spectral information is the function of chemical and physical properties of the material in interest, presenting a reliable and time efficient application for remote sensing analysis of Earth surface. The detailed information can be utilized up to the research motivation and the scale of the collected data by means of economical and time efficient way.

The research topics for the time being is primarily focused on developing automated methods and novel approaches for hyperspectral imagery analyses, including modelling collected spectral samples, extraction of detailed surface information pf Earth crust. Geological exploration that include minerals, rare earth elements and base metals detection and mapping, mine waste mapping and monitoring, soil characterization and monitoring, digital soil mapping, quantitative soil spectroscopy for sustainable management of renewable resources, soil erosion and land degradation

mapping are some of the ongoing projects on determination of Earth surface compositional information for geosciences (Chabrillat, 2017).

From the perspective of environmental applications of hyperspectral imaging with regard to contamination mapping, Winkelmann (2005) classifies the applications under main subjects of : oil spill detection on water, oil contamination mapping of soil and detection of geogenic hydrocarbon micro-seepage and macro-seepage in hydrocarbon exploration ,analysis of mining operation related contaminations, vegetation stress mapping as an indicator for soil contamination that is induced by metals, salt and organic contaminants due to hazardous wastes.

In scope of this study, the potential of hyperspectral signature based algorithms and anomaly detection techniques to determine the environmental implications of contaminations is investigated. With the existing data limitations, the applications are performed on an oil spill region, a natural microseep area for methodology development, which then implemented to monitor the potential of acid mine drainage in a coal mining area. Accordingly, a comprehensive literature survey is conducted on hyperspectral signatures of hydrocarbons and their surface implications associated to specified spectral behavior. Based on this line of work, spectral properties of soils that will be useful for determining the surface manifestations of altered minerals are also elaborated. This conducted survey is linked with the altered iron minerals which determines the acid mine drainage potential of the mining sites in detail.

1.3 Spectral Properties of Soils

Soil is the complex mixture of weathered rocks and minerals composing the earth's crust, which is extremely variable in its physical and chemical composition. The differentiated nature of soils is explained by the variable interaction in a soil-forming factors including climate, time, organisms, topography, and parent materials (Ben Dor et al., 2009). As mentioned previously, soil's chemical, physical and mineralogical

structure is associated with the wavelength specific absorption across electromagnetic radiation (Clark, 1990). In addition to chemical composition of soils, some physical parameters are reported to be significantly affecting the soil spectral fingerprint such as particle size distribution, moisture or water content, the texture (i.e. silt, sand, clay) or soil salinity.

According to study conducted by Baumgardner and his colleges (1981), soil constituents effecting the reflectance properties are listed as moisture, organic matter, particle size, iron oxides, , mineral composition, soluble salts and parent rocks. Generally speaking, soil reflectance spectra demonstrates a concave shape between the wavelengths of 0.4 – 2.5 μm and the reflectance values increase towards SWIR wavelength. The most prominent absorption features are the water absorption bands at 1.4 μm and 1.9 μm . Several minerals can be discriminated between 2.1 μm - 2.5 μm due to the inherent vibrational processes, while some small absorption features can be observed in VNIR region due to electronic transition in minerals, organic matter contents or water absorption bands. Viscarra-Rossel and Chen (2011) also identifies the contributing factors to overall soils spectra with the contents of iron oxides, organic matter, carbonate, the water amount together with particle size distribution as well. Figure 1-7 illustrates some significant absorption features associated with contributing soil constituents.

Stoner and Baumgardner (1981) investigates soil reflectance signatures of 240 soil samples, collected from 48 different states having 17 different temperature-moisture regimes, in order to understand whether they can be grouped under some categories. Their research yields to five major spectral signature categories representing all collected soil sample compositions as illustrated in Figure 1-8.

Among the parameters that is influential on soil spectra, moisture is one of the significant ones with several absorption features in specific locations of electromagnetic spectrum.

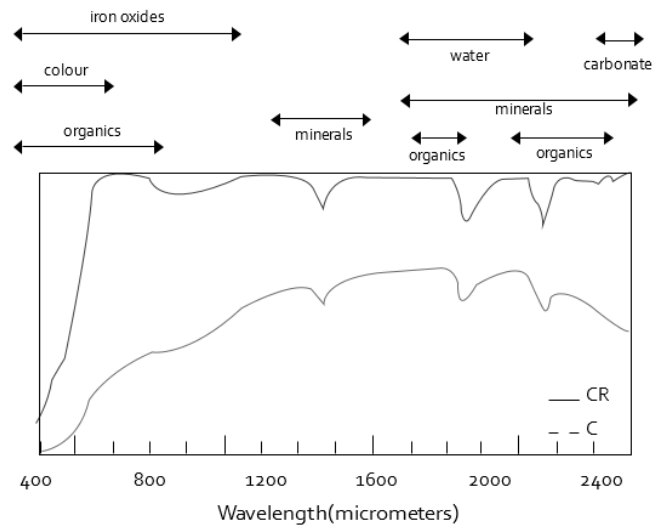


Figure 1-7 Wavelength positions related to some constituents of soil (Viscarre Rossel and Chen, 2011)

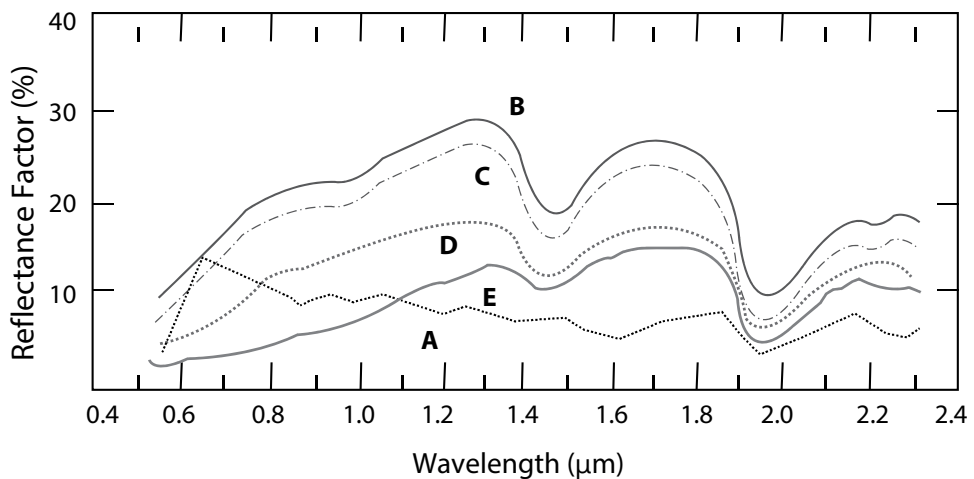


Figure 1-8 Soil Spectral Reflectance Curves (Stoner and Baumgardner, 1981) A: organic affected soils, B: minimally altered soils, C: iron-affected soils, D: iron dominated soils, E: organic dominated soils

Hunt (1977) reported the presence of molecular water with the diagnostic absorption feature around 1.4 μm and 1.9 μm and additionally referring the absorption pairs of 2.2-2.3 μm or 2.3-2.4 μm as to associate with the existence of OH ion bending.

Soil organic matter content is also known to lower the overall reflectance of soil spectra noticeably as its concentration gets higher. Baumgardner (1970) also mentions this effect by stating the fact that this decrease is noticeable only when the organic matter content exceeds 2.0%. Iron content is mentioned as another important soil component demonstrating absorption features around 0.9 μ in VNIR region due to electronic transitions of metal ions (Hunt, 1977). In addition, the absorption feature at 0.87 μ m is indicated as an evident of iron oxide coatings on sand grains in fine sandy soils. Iron oxides and hydroxides that are ample in many soils display broad absorption features in the visible and near infrared wavelength regions between 0.5 μ m and 1.3 μ m. (Baumgardner, 1985).

Another feature influencing the overall spectra as well as the absorption depth is particle size distribution of soils. As the particle size distribution decreases, the overall reflectance tend to get higher due to the fact that the smooth surfaces have smaller voids (Stoner et al., 1979). Because of the scattering caused by the existing voids, the absorption bands demonstrates shallower depths in comparison with the surfaces with coarse grains.

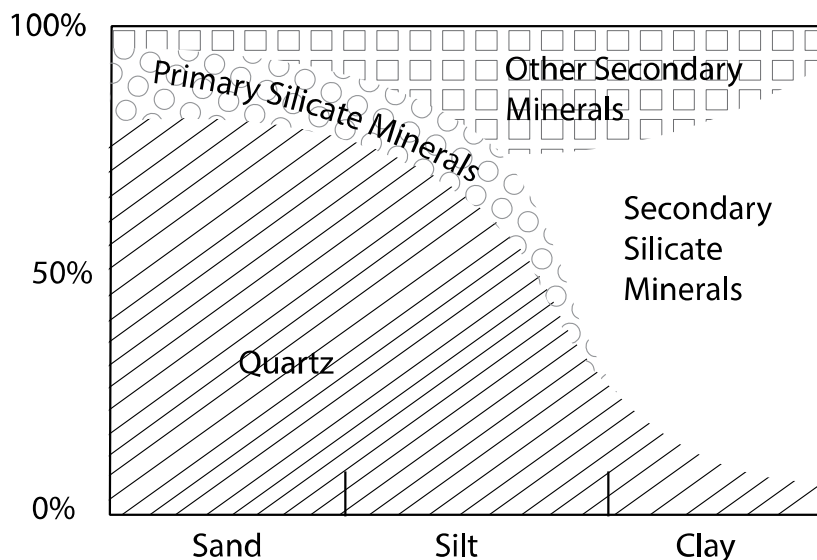


Figure 1-9 Mineralogical Composition of Soils, illustrating relative abundance of each mineral (Modified from Irons, 1989)

Figure 1-9 gives the mineralogical compositions of soils including relative abundance information. Quartz, the most ample mineral in soils, unfortunately do not show any absorption features between the interval of 0.4 μm – 2.5 μm region. Other ubiquitous minerals like clays, iron oxides, carbonates or feldspar do have specific absorption characteristics, mostly identified in SWIR region between 2.2 μm – 2.5 μm OH- ions, presenting an opportunity for their identification through hyperspectral analysis. Among the others, clay minerals, mica, carbonate, dolomite, gypsum and hematite are mostly referred minerals as to their unique absorption features in the 0.4 μm – 2.5 μm domain of electromagnetic spectrum.

1.4 Environmental Applications of Hyperspectral Analysis

In this subsection, an extensive survey on direct/indirect detection of hydrocarbon induced and mining induced anomalies, and their remote sensing applications are presented. The previous work conducted in the field of detection and mapping of anthropogenic contaminations of ambient media with the help of satellite images and hyperspectral images are elaborated. Both direct and indirect detection of hydrocarbon pollutions or generation of iron mineral indices in soil and water matrixes are considered in addition to the detection of anthropogenic deposits, such as waste dumps, overburden dumps, and mine tailings.

The concentration of this literature survey revolves around direct and indirect detection of contaminated sites by means of hyperspectral and multispectral images, with a focus on hydrocarbon and coal mining related anomalies. For evaluating indirect implications of hydrocarbon seepages, considering the limited number of publications and our application field, detection of natural hydrocarbon seepages is detailed, as they are in some aspects related to soil hydrocarbon contaminations of anthropogenic origin.

1.4.1 Hyperspectral Sensing of Hydrocarbon-Induced Anomaly Detection

Tracing the micro- and macro- seepages has been an invaluable approach for the exploration of oil and gas reservoirs as can be a tool for identifying large fuel contaminated areas. The alterations of surface sediments overlying the gas/oil reservoirs due to in situ long term seeps along the mitigation pathways exhibit surface anomalies which facilitate the exploration of the reservoirs (Shi et al., 2010). The hydrocarbon-induced anomalies are vastly recognized in remote sensing literature, indicating the existent absorption features of hydrocarbon bearing minerals in electromagnetic spectrum. Knowing the well-known hydrocarbon absorption characteristics at 1.73 μm and 2.31 μm , the target region of the hydrocarbon microseeps is considered to be differentiated from the background with the spectral signatures of the reference valley (Kuhn et al., 2004). Band ratio of the images of specified altered minerals, the feature oriented principal components, and the false color composites with original bands or band ratios are some of the mostly utilized techniques in remote sensing studies for hydrocarbon microseepage mapping. However, utilization of only a few bands in these techniques contradicts the idea of handling the most information we can get from image for target detection. The high dimensionality of spectral data can provide significant evidence for the identification of mineral in interest, as in signature based algorithms or even better in unmixing techniques.

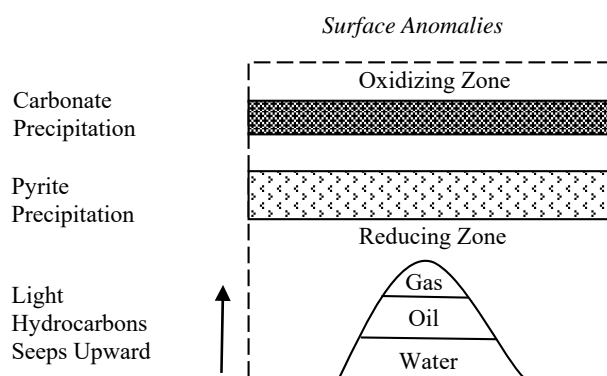


Figure 1-10 Generalized form of soil and sediment geochemical alterations (Modified from Schumacher, 1996)

a. Remote Sensing Literature on Hydrocarbon Induced Alteration Detection

Comprehension of the mechanism of the geochemical and geophysical processes as well as the microseepage processes with their indicators on soil surface is required to identify the abnormalities due to macro/microseepage systems using earth observation satellites. In this section, the mechanisms of hydrocarbon microseepage process and the related anomalies are summarized. The literature survey indicate the alterations on surface sediments and soils overlying the oil/gas reservoirs are traceable with remote sensing techniques due to the fact that these variations have particular spectral signatures. The applications and their capability for detection of hydrocarbon microseeps are elaborated in the second part of this section.

Bacterial or microbial activities are accounted as one of the main reasons of hydrocarbon microseepage alterations generating surface oxidation-reduction zones, which also facilitate both mineralogical and chemical changes. Schumacher indicates that oxidation of hydrocarbons are mostly related to bacteria or microbe activities with the reaction of the free oxygen or chemical bound oxygen (i.e. sulfates, nitrates) (Schumacher., 1996). In addition, to the alteration of the redox potentials, soil alkalinity and acidity changes are reported as causing the mineral alterations. In his study, he refers carbonate cementation, bleached red zones and pyrite mineralization as main alteration variations due to hydrocarbon microseepage process, especially for red beds or sediments overlying the oil fields. Carbonate minerals, sulfide minerals, bleached red beds, clay alteration, existence of some trace elements, change in electrochemical characteristics and finally the magnetic minerals are the main headings dwelled on regarding with the alterations due to hydrocarbon micro/macro seeps. Methane oxidations, interaction of hematite with sulfide minerals, removal of hematite and alterations due to the reducing environment can be appointed as the leading reasons of the prominent alterations stated earlier, which are simply illustrated in Figure 1-11(Schumacher, 1996).

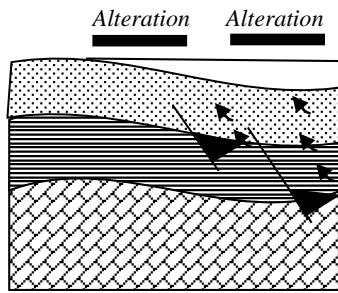


Figure 1-11 Hydrocarbon Migration Process (Modified from Schumacher, 1996)

The mitigation of hydrocarbons through the rock columns are described in Khan and Jacobson's study as the movement of light hydrocarbons vertically through the connected fractures or microfracture systems, which might be induced by respective reservoirs. The microseepage pathways along these fractures or faults and their vertical mitigation routes, namely chimneys, are shown with different stratigraphic layers in Figure 1-11. In the study, the capability of hyperspectral sensing to put forward the hydrocarbon related abnormalities is stated as a great potential for further studies (Khan and Jacobson, 2008).

Another study conducted by van der Meer et al. (2002) concentrates on the surface indicators of hydrocarbons as well as their recognition by earth observation satellites. Reservoir leaks are classified regarding to their visibility to human eye as macroseeps and microseeps, earlier is the visible. The seepages are also divided into two groups regarding with their formation as active and passive. Subsurface leaks of the reservoirs with low and high molecular hydrocarbons in large amounts of are named as active, whereas the intermittent/minor leaks with low molecular weight hydrocarbons are passive. The study also emphasizes the significance of the generation of gasses, i.e. methane, butane, carbon dioxide, to alter the minerals usually confronted in the hydrocarbon microseep areas. These gasses are mitigated through the fractures or microfracture systems with effusion, diffusion or vertical ascent of hydrocarbons with low molecular weights which are explained with the chemical and hydrodynamic potential variations in the system (Van der Meer, 2006).

The surface manifestations of hydrocarbons are classified into four categories, which are halo anomalies, fault related anomalies, local trappings, and no anomaly. In halo anomalies, the edges commonly include high concentration of hydrocarbons, while the center contains low hydrocarbon levels. The faults or major cracks are basically gates for the mitigation of hydrocarbon from the gas/oil reservoirs. The final abnormality, local trappings, are formed due to the existence of localized subsurface barriers that is also described as a facilitator for methane separation with bacterial activities. The bacterial findings are also pointed out to lead the generation of hydrogen sulfides and carbon dioxide in deep oil fields, which also increases the acidity of the environment for mineral alterations. To investigate the behavior of the change in mineral signatures, the montmorillonite spectral signature, as one of the most common clay minerals in altered zones, with differing organic compounds are presented to observe the changes in absorptions and reflectance trend. The study emphasizes the fact that hydrocarbon seepage related indicators on the surface can be sensed by analyzing the absorption features regarding with the alterations, especially at a given specific wavelength intervals defined for bleached red bands, clay mineral alterations and carbonate precipitations is emphasized.

In the view of the given literature, the mineral alterations related to the hydrocarbon macro/micro seeps, which are generated by near surface oxidation-reduction zones due to microbial, bacterial activities, low molecular weight hydrocarbon seeps and the gases enable the traceability of hydrocarbon induced soil & sediment manifestations. The vertical movement of the seeps is assisted with the existing subsurface faults or microfractures which also can alter the ascend direction. This vertical movement of hydrocarbon through the fracture systems, i.e. chimneys, lead some anomalies usually visible as halos, fault related abnormalities or local trappings usually containing bacterial activities. Bearing in mind the given indicators, researchers are encouraged to investigate new methodologies and innovative technologies to explore the oil/gas resources, one of them is being the remote sensing analysis.

According to conducted studies, making use of the satellite imageries for oil/gas reservoir exploration has been highly popular offering a great potential to analyze information about macro- and micro-seepage related surface manifestations. Hyperspectral sensors, in particular, have a greater capability comprising subtle responses across electromagnetic spectrum with higher spectral&spatial resolutions. The ability and utilization of cutting edge sensors enable the recognition of the alteration zones as well as the mentioned anomalies in hydrocarbon micro- and macroseepage regions, offering an economical & fast analysis for oil exploration. Next part of the literature study focuses on the remote sensing applications for hydrocarbon macro- and micro- seepage detection.

b. Detection of Hydrocarbon Induced Anomalies with Remote Sensing

Remote sensing analysis on hydrocarbon induced anomalies are applied with simple band ratioing or generation of some color composites to highlight the searched indicator (Shi et al., 2010), producing mineral indexes for altered layers (Kuhn et al., 2004), or simply calculating principal components analysis (Crosta et al., 2003; Petrovic et al., 2008; Freeman, 2010). In addition to the advances on the techniques for geochemical/geophysical analysis, the developments in earth observation satellites have increased the technical capabilities of the sensors as much as the attention on the algorithms to be developed benefitting from them. Fusion of several images from different sensors, pansharpening and classification algorithms can be regarded as some of the state of art techniques improved with the advanced technology. In compliance with that, the research on supervised and unsupervised detection algorithms on satellite/airborne images have started to get significant attention in the last decade.

Crosta technique, which is regarded as a corner stone for mapping mineral alteration, is basically one of the methodologies referred in several studies (Crosta et al., 2003). This technique identifies the significant bands for the searched target considering its spectral fingerprint. Then, the eigenvalue statistics are calculated for the selected bands using principal component analysis. The most relevant principal component is

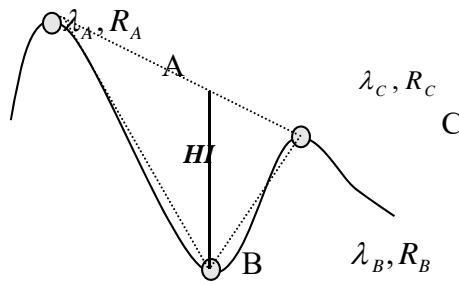


Figure 1-12 Hydrocarbon Index (Kuhn et al., 2004)

determined by observing the eigenvector loadings, which is exhibited by the highest opposition values regarding with the diagnostic characteristics of the target mineral. That is to say, the opposite signs of eigenvectors stand for the abundance of the target minerals that can be exhibited as dark or bright pixels according to the diagnostic behavior of the target and specified bands (Crosta et al., 2003).

One of the baseline studies to detect hydrocarbons is the research conducted by Kühn and his colleges (Kuhn et al., 2004) to identify a hydrocarbon index with HyMap imagery. In the research, the specific absorption features of the hydrocarbon bearing materials are stated as 1.73 μm and 2.31 μm . The index is generated in the form of Normalized Difference Vegetation Index (NDVI) with the unique characteristics of specific absorption band of hydrocarbons @1.73 μm . The hydrocarbon index, *HI*, is defined as:

$$HI = (\lambda_B - \lambda_A) \frac{R_C - R_A}{\lambda_C - \lambda_A} + R_A - R_B$$

where λ_i and R_i stand for wavelength and radiance values respectively as illustrated in Figure 1-12. This index not only can be applied to reflectance images but also radiance ones which favors its common utilization. The oil contaminated regions as well as hydrocarbon bearing materials can be detected efficiently without a prior atmospheric correction operation as well. Judging from the index equation, it is obvious that the higher the index gets, the higher the hydrocarbon content is. As the hydrocarbon content ascends, the A, B, C index points are expected to form a triangle

rather than a triangle, suggesting the absorption depth is proportional to the amount of existent hydrocarbons (Figure 1-12). The index performance is suggested to be affected by the flight altitude, radiometric quality and spatial resolution of the hyperspectral sensor in consideration (Kuhn et al., 2004).

A study conducted by Shi and his colleagues utilized ASTER data to designate hydrocarbon microseepage induced anomalies with the application of band ratios & color composites, also supported by the laboratory analysis of collected samples (Shi et al., 2010). The altered rocks are differentiated by calculating the ratio of band four to band nine of ASTER image, which is also supported by the ratio of band two to band one highlighting the unaltered class. The study often makes use of RGB false color composite images to interpret the microseepage related alterations in the study area. The value of interpreting ASTER data to determine the microseepage induced alterations such as iron oxide bearing rocks, carbonate bearing rocks, and bleached beds, which points out the deep hydrocarbon bearing systems, is emphasized in the conducted study.

The research conducted by Petrovic and his colleagues applies classification and fusion techniques to determine the alterations regarding to hydrocarbon microseeps. Bleached beds, high clay contents, abnormality in weathering patterns and finally carbonate precipitations are the designated abnormalities in the field. The classified ASTER data is fused with the radar image to delineate the anomalies, which also is confirmed by the geochemical analysis proving the presence of bleaching zones as well as the other alterations in the study area (Petrovic et al., 2008). Moving from this point, as a representative research of signature based algorithms using USGS library to map hydrocarbon related alteration minerals, Freeman performed several experiments utilizing Spectral Angle Mapper (SAM) and Spectral Feature Fitting (SFF) methods to determine the algorithms performance as well as the most promising mineral indicator with the present signatures. According to the study, SAM algorithm performs better than SFF to designate the hydrocarbon microseepage related

alterations and jarosite is determined as the most promising mineral as hydrocarbon indicator among all the searched endmembers which are siderite, kaolinite, alunite & calcite (Freeman, 2003).

1.4.2 Hyperspectral Sensing of Coal Mining Induced Contaminations

Active or abandoned, mining is regarded as one of most profoundly influencing industrial operations the environment. Although the environmental impacts of mining activities vary with regard to the type of the mineral and the selected mining method, deposition of gangue/waste minerals, mine effluents and leachates released from the waste piles during and after the operations can be mentioned as some of the most common effects (EO-Miners, 2013). Disposing the waste material improperly might contaminate not only surface drainage routes but also can leach to ground water table, which also might have been disturbed by the operations, creating a basis for polluted and extremely acidic waters. In addition, the percolation of water through these waste piles induces an acceleration in total dissolved solids rate, which include carbonate, calcium, bicarbonates and sulfates, contaminating waters to such an extent that it can't be used even for industrial or agricultural purposes (EO-Miners, 2013; Johnston et al., 2008).

Coal mining, as typical in all mining activities, causes drastic landscape alterations by presenting large-scale surface openings, i.e. open pits, subsidence in underground operations, waste dumps, storage areas, which can change water courses inevitably. Along with the change in landscape and water routes, acid mine drainage presents itself as a severe byproduct in the presence of pyrite mineral within the chemical structure of coal seams. The reaction of pyrite to exposed water and air causes sulfuric acid generation in addition to high dissolved iron contents. This acidity facilitate the dissolution of other heavy metals in the environment, escalating the toxicity levels of enclosed water bodies. Unless preventive measures are taken, this system will increasingly contaminate the surrounding habitat as soon as the calcite or other

carbonate minerals are dissipated (Keating, 2001). The impact of mentioned problems can create long-term environmental and socio-economic outcomes, which requires tremendously complicated and expensive remediation plans. Thus, coal-mining sites ought to be managed appropriately to achieve lasting stability and to minimize any water and soil pollution

One of the prominent studies on spectral reflectance properties of macro carbon-bearing materials is conducted by Cloutis and his colleagues (1994). The study concentrates on spectral behavior of several carbon bearing samples including carbides, graphite as well as oil shales, oil sands, coal and coal tar between the range of 0.3 – 2.3 micrometers. The comparison between the collected spectra reveals that reflectance spectrum of coal is red sloped demonstrating similarity with oil sand spectrum, but not with the oil shales. The lack of absorption features in coal spectra, differing from oil shales, is explained with the absence of C-H band, which is in fact in congruent with calculated low H-C ratios of coal samples. It's another significant result that as the aromatization of coal increases, the observed absorption bands are flattened, causing basically a flat line. Cloutis (2004), further elaborates his research with different coal samples, stating the fact that distinct absorption characteristics of coals appears only in lowest rank samples around 1.4, 1.9 and 2.1–2.6 micrometer region. Absorptions around 1.7 and 2.3-2.5 are attributed the organic combinations and overtone bands (C-H stretching). Figure 1-13 gives the observed spectra for coal and related samples with their detailed explanations.

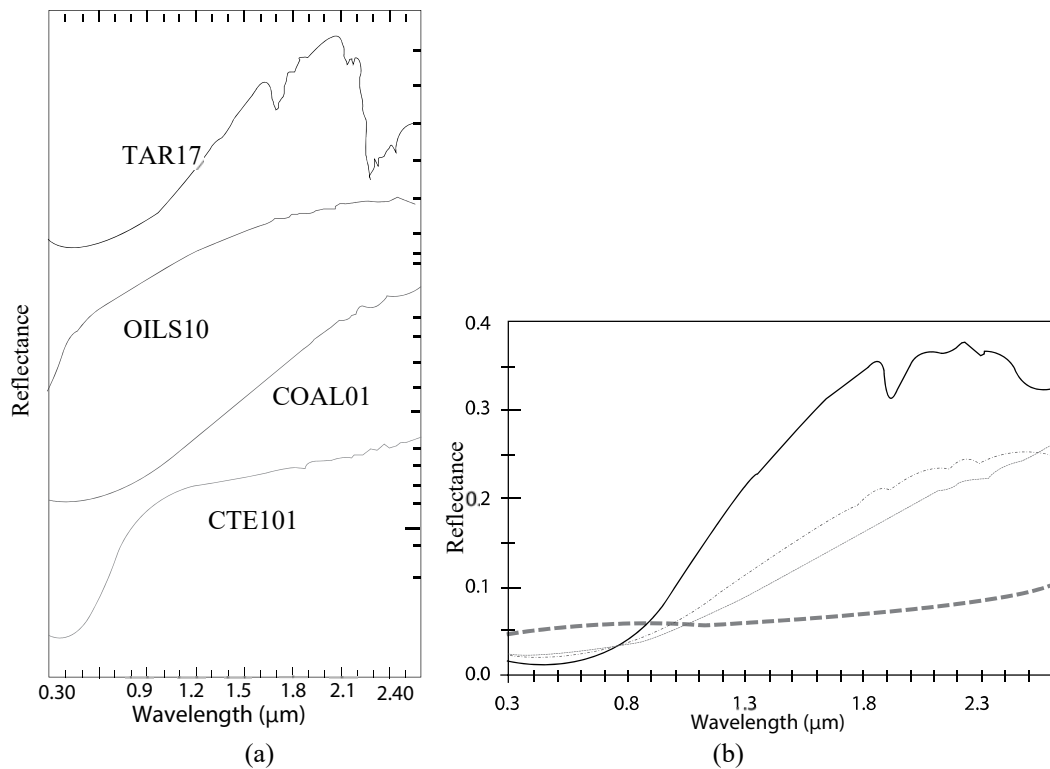


Figure 1-13 a) Absolute spectra of powdered samples of macromolecular organic bearing minerals (COAL01 [coal], Oils10(Oil Shale), TAR17 [Oil sand], CTE191 [Coal tar] (Cloutis et al., 1994)
 b) Reflectance spectra (0.3–2.6 mm) of a number of coal samples. From top to bottom at 2 mm: COAL10 (lignite), COAL14 (high volatility C/B bituminous), COAL21 (low volatility bituminous), and COAL22 (anthracite) (Cloutis, 2003)

In relation to the research on near infrared spectral characteristics of coal samples, their chemical structure and constituents, one of the most prominent studies for the evaluation of environmental impacts of mining operations using airborne hyperspectral sensors is the European Union (EU) MINEO project (MINEO, 2003), namely “Assessing and monitoring the environmental impact of mining activities in Europe using advanced earth observation techniques”. In this extensive research, several types of mines were investigated to elaborate on the levels of contamination, determine the wind directions, potential acid mine drainage producing minerals, water drainage systems, slope stability problems or to monitor the subsidence mitigation processes (MINEO, 2003). Another EU project (EO-Miners, 2013), which focuses on the sustainable exploitation of minerals resources, was also started in 2009. Three

mining fields, two coal mines (Sokolov and Whitbank) and one gold mine (Makmal), are studied to collect ground truth field samples as well as field spectral data to produce physical soil property maps and acid mine drainage producing mineral maps (especially secondary iron oxide minerals) by analyzing HyMap hyperspectral images. The project aimed to produce indicators to recommend new policies as well as pointing out the required changes on the current ones in both corporate and government levels for the sustainable mining purposes (EO-Miners, 2013).

Both of these forthcoming, comprehensive projects makes use of satellite data collected by conventional sensors (Landsat, SPOT and ASTER, Worldview-2) and airborne data acquired by hyperspectral airborne surveys, LIDAR survey, thermal infrared surveys. Furthermore, in situ measurements including field spectrometers gathering data in VNIR, SWIR, and TIR regions of electromagnetic spectrum, in situ point measurements (pH, temperature), street dust sampling and analysis, information and/or measurements about vegetation, soils, surface and groundwater, dust are also performed. Given the extensive methodology of the projects and the utilized tools, both financial and application challenges, demanding the support of policy changes, especially for country scale investigations, considering the exorbitant sums associated with it.

In the scope of environmental effects of mining wastes, Turkish government conducted a project called ‘‘ Technical Assistance for Mining Waste Management’’ project during 2012-2014, which is conducted under the harmonization with European Union Legislations (i.e. Twinning Projects), on environmental protection in order to prepare the necessary regulations with regard to the mining waste management. The project has covered almost 300 mines, spread all around Turkey.

The objective of a twinning project is to support new EU member states and EU candidate countries in adopting community law and in establishing the necessary administrative capacities. Experts from the administrative authorities of the EU

Member States pass on their know-how and experience in implementing community law to colleagues in their respective partner country within the framework of the EU's Instrument for Pre-Accession (IPA) and the European Neighborhood Policy Instrument (ENPI). The Resident Twinning Advisor (RTA) is referred to as the backbone of any project and works in the partner authority throughout the entire project, usually one to two years, and supports colleagues on site in achieving concrete project objectives.

The membership requirement of “Mining Waste Directive” states that “Member states shall ensure that an Inventory of closed waste facilities, including abandoned waste facilities which cause serious negative environmental impacts or have the potential of becoming in the medium or short term a serious threat to human health or to the environment is drawn up and periodically updated.”

This unique project, unlike most of the countries, has conducted 300 mine site visits, collected extensive field information including sampling in order to establish a country wide risk-based inventory to technically support the implementation of EU legislations. Within each commodity group, scores were assigned to each mine waste site based on the following criteria:

- Active or abandoned site
- Host rock geology
- Largest mine waste dimension
- Type of environmental receptor
- Distance to nearest environmental receptor
- Presence or otherwise of a pit lake

A risk score is calculated based on the total sum of the aforementioned criteria and their correspondence scores. For instance, if the mine site exhibits acid mine drainage during the site visits, the highest score is noted.

It is important to note that as all the mine regions are classified as in potential danger in the report prepared within this project. Based on this outcome, the results of the projects was not announced by the government of Turkey. The analysis results were planned to be publicly available in the beginning, though because of the contradictions they were not utilized and were not released to public.



Figure 1-14 Photographs Taken from the coal mine sites of Acid Rock Drainage (Çanakkale-Balıkesir) (Twinning Project Report, 2014)

Some of the results achieved at the end of the project are as follows:

- Extractive industries may alter the composition of the landscape, disrupting land use and drainage patterns, contaminating soil and water resources, removing habitats for wildlife, and generate huge amounts of waste. This

particular waste must be managed in specialized facilities in accordance with specific rules.

- Regarding the observed land degradations, it is concluded that the competent authorities should pay more attention particularly at lignite mines and small mines. In addition, there was some obvious land degradation at some iron and chrome mines both at abandoned or inactive ones. While coal power plants are essential for Turkish energy supply an environmental improvement at lignite mines should also be matched to this demand.
- An unexpected experience of the site visits is the observed lack of wide-spread Acid Mine Drainage (AMD) problems. Due to favorable geological conditions, especially at the visited copper and gold mines, there was very limited acid mine leachate generation and associated environmental degradation.
- The most critical areas were lignite mines where AMD phenomena is abundant such as those observed during the Çanakkale and Balıkesir Trips.
- There is room for lot of improvement of mine waste facility management but the 300 mine site visits have confirmed the most important and urgent actions have to do with the improvement of the legislative environment and the proper improvement of the constructive relationship between the competent authority and private mine operating sector.
- Finally, it is suggested that the Turkish Mine Bureau MIGEM should also have local/provincial officers. This would enable a better daily communication between the operators and the authorities including keeping the mine site management information updated, providing due training and knowledge transfer to the mine managers and monitoring mine site development waste management. This organization scheme is expected to minimize the current information scarcity in the sector.

Within the scope of this dissertation, an abandoned lignite mine site located in Central Anatolia in the province of Çankırı, Turkey is selected. The region has been of an interest in the last decade due to its availability for site visits and data collection as a non-operating mine, avoiding the potential conflict with authorities. The abandoned mine site possesses major environmental problems such as non-rehabilitated open pits (Figure 1-15), uncontrolled excavated areas and voids, abandoned buildings, disturbed drainage networks, dumpsites with steep angles and most importantly acid mine drainage generation (Figure 1-16). That's why, this region is studied in Chapter 5 and Chapter 6 for analyzing the topographical changes as well its AMD generation potential in detail.



Figure 1-15 Open pit area, Çankırı, Ovacık Mine (Soydan, 2013)



Figure 1-16 Acid Mine Drainage in Çankırı, Ovacık Mine (Soydan, 2013)

CHAPTER 2

HYPERSENSPECTRAL IMAGE ANALYSIS ALGORITHMS

In this chapter, the utilized algorithms within the scope of thesis study is presented in detail. In the Section 2.1, a general information about hyperspectral anomaly and target detection algorithms is reported, including mathematical definitions of applied methods of RX and Kernel RX algorithm, Desired Target Detection Algorithm, Spectral Match Filter, Correlation and Normalize Correlation Algorithms. This section is followed by the unmixing methods (Section 2.2), which includes the detailed definitions of Fast Autonomous Spectral Endmember Determination (N-FINDR), Vertex Component Analysis (VCA), Minimum Volume Simplex Analysis (MVSA) and finally A Simplex Identification via Split Augmented Lagrangian (SISAL).

2.1 Hyperspectral Anomaly and Target Detection Methods

Target detection for remote sensing applications has been a great focus area in the last decade with the developments in hyperspectral imaging systems. Hyperspectral sensors provide contiguous spectral bands over electromagnetic spectrum with narrow wavelength intervals in spectral domain as well as high pixel resolutions in spatial domain, enabling to identify the searched targets in several contexts. The capability of sensors delivering detailed information about a pixel within a data cube enable the scientists to differentiate the focused object from the surrounding area (Monalokis et al., 2012). These developments have provided new applications ranging from vegetation, geological, mineralogical detection to defense and military object detection. Environmental assessment using hyperspectral target detection stand as a challenge for the scientists with its potential impacts on communities and species living nearby, especially where such a large amount of oil mitigation is in consideration. The oil contaminated wetlands on coastal regions, the distress on vegetation and polluted soil require a quick and comprehensive evaluation as it may

affect environmental and public health in a short span of time (Salem and Kafatos, 2001).

As mentioned earlier, target detection techniques in hyperspectral image analysis have been regarded with respect to the existence of a pre-knowledge about the searched target. The target detection methods without any information of the object of interest are mainly falls into the group of anomaly detection methods (Monalokis et al., 2012; Alam and Sidike, 2012), which are searching for the anomalies in an acquired image. Statistically, anomaly can be defined as the data or observation which does not fit into the general characteristics of a given data set. Matteoli (2007) defines the anomaly detection concept as a binary classification problem in which the target is scarcely populated. However, the background clutter is heterogeneous and highly populated, which makes the classification error calculation impractical, as it would mean to label almost each pixel in the image. No matter what the application is, the investigated target is scarce, constituting very small portion of the data set justifying the primary definition of the author.

Among these methods, Reed-Xiolo (RX) method has taken a significant attention in the literature with its pioneer aspect and simplicity (Nasrabadi, 2014; Malpica et al., 2011). The algorithm is considered to be a benchmark as an anomaly detector, on which several modifications have been implemented so far. The method produces Mahalanobis metrics to describe the similarity between the target pixel and the background to differentiate the abnormal objects. The RX method, which uses the whole image as a background, is then improved by defining the background within a local neighborhood surrounding each pixel, called as local RX. In later approaches, Kernel based RX methods defining the similarity of two pixels by using nonlinear mapping techniques, namely ‘kernel trick’, have shown significant performance gains in terms of detection rates (Zare-Baghbidi and Humayouni, 2013).

A visual describing the logic behind the sliding window operation in local-RX algorithm is drawn for a case of multispectral data cube in Figure 2-1. Here, the outer

window is utilized to model the background cloud while the inner window is appropriately selected in consideration with the searched target size. It should be noted that both of these window sizes have a significant role in the performance of local-RX method (Nasrabadi, 2014; Zare-Baghbidi and Humayouni, 2013). While larger windows might cause to miss the searched target, smaller one can lead to abundant high scores revealing the local variances in the window other than the target, i.e. false positives.

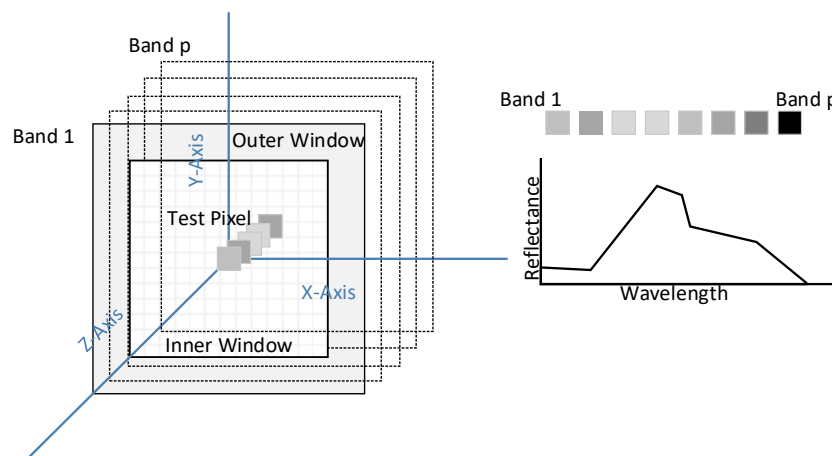


Figure 2-1 Double-concentric window for spectral anomaly detection

The aforementioned second approach uses a previously obtained signature of the target, which uniquely represents the target's reflection characteristics with respect to the spectral wavelengths. In order to conclude whether an acquired hyperspectral image involves a desired target, each pixel of the hyperspectral image is matched with the target signature and classified as a target or background. The existing approaches in the literature mostly achieve this task in two ways. The first approach treats each pixel without explicitly considering the background during the modelling and matching operation. Normalized cross correlation and spectral matched filter are typical representatives of this approach (Du et al., 2003; Ren and Chang, 2013; Matteoli, 2017). The second approach takes also the background into account by

modelling a target pixel as a linear mixture of target spectral signature and background spectral signature. The main methods in this group involve orthogonal subspace projection (OSP), adaptive matched subspace detection (AMSD), and desired target detection and classification algorithm (DTDCA). The second group methods using the background has provided a better detection accuracy compared to the first group (Ren and Chang, 2013; Du et al., 2003). Among these methods using background modelling, DTDCA has also verified as an effective method in the literature with its superior detection performances and more flexible background generation algorithm requiring no prior information about the acquired scene (Ren and Chang, 2013).

Spectral mixture analysis is a technique to resolve the constituent endmembers of a pixel spectrum based on the assumption that the overall spectra represents the combination of two or more samples in the observation pixel. This method is important to identify the spectral components of each pixel, known as endmembers, to produce corresponding abundance maps with inversion process. According to Keshava and Mustard (2002), the spectral unmixing techniques are grouped into two classes, which are linear and non-linear. The linear unmixing approaches assumes that the constituents of each pixels are spatially discrete and isolated from each other, while the non-linear unmixing presume all components are mixed with each other, presenting a greater challenge for their corresponding spectral extraction. It's imperative to note that the success of linear unmixing algorithms is extremely related to the accuracy of identification of all members, which is a part of the challenge, keeping in mind how complicated the mixing of surface can become. The validity of linear unmixing models are reported to be roughly about 3 – 5 % of absolute abundance of a material (Keshava and Mustard, 2002).

2.1.1 Anomaly Detection Algorithms

2.1.1.1 RX Algorithm

RX algorithm makes use of the Mahalanobis distance metric to calculate the likelihood ratios by normalizing the difference between the test pixel and the background to allocate the abnormalities in the acquired scene. Mahalanobis metric is utilized to determine the distance between the point cloud consisting of background pixels and the target pixel. Different from the Euclidean distance, the Mahalanobis distance takes also the shape of the clouds described with the covariance matrix into account (Malpica et al., 2011, Zare-Baghbidi and Humayouni, 2013). Given a pixel of the hyperspectral data cube, \vec{x} , the RX algorithm describes the abnormality of the pixel as:

$$\hat{\rho}_{RX}(\vec{x}) = (\vec{x} - \vec{\mu})^t \Sigma^{-1} (\vec{x} - \vec{\mu})$$

where $\vec{\mu}$ and Σ are defined as the estimated mean and covariance matrix of the background samples. Given the Equation (1), the algorithm calculates the abnormality of each pixel of the hyperspectral data cube and decides on the regions of anomalies. The RX method, which uses the whole image as a background, is then improved by defining the background within a local neighborhood surrounding each pixel. While the first case is regarded as the global RX method, the second case with the local neighborhood is called as local-RX in the literature.

2.1.1.2 Kernel RX Algorithm

Given two sets of observation belonging to different classes might not be linearly separable in many cases in pattern recognition. A suitable nonlinear transform, denoted as ϕ , applied to the observed data can make these given sets separable. However, this nonlinear transform (ϕ) is not always computationally feasible for a direct implementation.

The main idea in Kernel RX is to be able to find a suitable kernel function, $k(x, y)$, which enables to find the Mahalanobis distance between the target pixel and the

background in the transformed space without needing to convert these pixels into that domain. Given a transformed version of a pixel of the hyperspectral data cube, $\phi(r)$, the Kernel RX algorithm describes the abnormality of the pixel in the transformed domain as:

$$\partial_{RX}(\phi(r)) = (\phi(r) - \bar{\mu}_{b_\theta})^t \hat{C}_{b_\theta}^{-1} (\phi(r) - \bar{\mu}_{b_\theta})$$

where $\bar{\mu}_{b_\theta}$ and \hat{C}_{b_θ} are defined as the mean and covariance matrix of the background samples in the transformed domain.

In this study, we use the Gaussian Kernel for the implementation of kernel RX due to its superior performance reported in the literature. For a given two hyperspectral pixels, the Gaussian Kernel is defined as:

$$k(x, y) = \exp(-\|x - y\|^2 / c)$$

where c is a real constant.

2.1.2 Signature Based Detection Algorithms

2.1.2.1 Spectral Matched Filter

Matched filter is a well-known algorithm in hyperspectral image processing which uses the spectral signature of a desired target for detection. The filter is designed to minimize the average power of the filter output for the background components while maximizing the output of the filter for the target signature. The solution for such a problem description is given as:

$$w = \frac{\Sigma_s^{-1} s}{s^T \Sigma_s^{-1} s}$$

where w is the vector corresponding to matched filter coefficients, s is the spectral signature of the target, and Σ_s is the covariance matrix of the hyperspectral data. Given the Equation (4), the algorithm calculates the output of the matched filter for each pixel of the hyperspectral data cube and examine the output for the desired target.

2.1.2.2 Desired Target Detection and Classification Algorithm

Desired Target Detection and Classification Algorithm (DTDCA) (Ren, & Chang 2003, Du et al., 2003) models the background for the given hyperspectral image and eliminates the background components from the hyperspectral pixels. A matching is then performed between the remaining terms on the pixels and the spectral signature of the target for detection.

The algorithm models a hyperspectral pixel (r) as a linear mixture of target spectral signature, background components and noise:

$$r = t\alpha_p + K\gamma + n$$

In the equation, t is the target signature and K is the background matrix, whose columns consist of undesired background spectral signatures extracted from hyperspectral data cube.

In the first stage of the DTDCA algorithm, a background matrix from the hyperspectral image is generated and used to eliminate background components from the measured pixels, r (Du et al., 2003). In order to eliminate the background components from the pixels, the pixels given in Equation (5) are multiplied with an annihilator matrix, P_K , which is expressed as:

$$P_K = I - KK^\#$$

where $K^\#$ is the pseudo inverse of K and I is the identity matrix. After such a multiplication, Equation (5) returns into the following form:

$$P_K r = P_K t\alpha_p + P_K n$$

In the second stage of the DTDCA algorithm, the measured pixels, whose background components are eliminated, are matched with the target signature for detection.

2.1.2.3 Correlation/Normalized Correlation

Correlation and normalized correlation (NC) algorithms are applied to reveal the relation between the target spectra and the hyperspectral pixels. The algorithm matches

the test pixel in interest with each pixel of the data set with correlation or normalized correlation algorithms. The correlation between two hyperspectral vectors are given below.

$$Corr(x, y) = \sum_{j=1}^p x(j)y(j)$$

Where x corresponds to the spectral signature of the target and y represents each hyperspectral pixel of the tested image. p stands for the number of hyperspectral bands.

In the case of normalized correlation, the correlation equation is normalized with the norm of the vectors x and y :

$$NC(x, y) = \frac{\sum_{j=1}^p x(j)y(j)}{\sqrt{\sum_{j=1}^p x(j)^2 \sum_{j=1}^p y(j)^2}}$$

The resulting matrixes are mapped to a 2D image to show the detected area for the searched target.

2.1.2.4 Spectral Angle Mapping (SAM)

Spectral Angle Mapping (SAM) is an algorithm, which utilizes multi-dimensional n-D angle to match the target pixels to reference spectra. The method calculates a spectral similarity metric by simply calculating the angles between the spectra, which have the vector dimension of number of bands. For an n-D data cube, the spectral angel is calculated as follows:

$$x = \cos^{-1} \left(\frac{\sum_{i=1}^n s_i r_i}{\sqrt{\sum_{i=1}^n s_i^2} \sqrt{\sum_{i=1}^n r_i^2}} \right)$$

where s is target signature, r is reference signature. The algorithm attenuates illumination and albedo effects by concentrating on the trend of both spectra.

2.2 Unmixing Algorithms

Identification of hyperspectral pixel composition by defining the material signatures and their fractions has been a challenge for scientists in the last decade. An observed pixel of a hyperspectral data usually contains several materials or endmembers, which cause the scattered energy to show a mixed signature. Depending on the spatial resolution, a hyperspectral pixel of low-resolution image mostly requires unmixing to determine its components. Unmixing a hyperspectral pixel means to identify the components in each pixel, their spectral signatures with the corresponding abundance fractions. The combination of the statistically dependent signatures of the comprehended materials is either linear or non-linear fashion, which promote the unmixing techniques on high dimensional hyperspectral data sets (Li and Bioucas-Dias, 2008).

Among the proposed techniques, geometrical algorithms have been widely studied benefiting the convex nature of hyperspectral vectors. The aim of these methods is to extract endmembers located at the vertices of hyperspectral data by constraining the summation of abundance fractions to one with the assumption of the fractions are all positive. In such a fitting, the vertices of a simplex set, which covers the hyperspectral vectors, represent the endmembers for the hyperspectral data cube by taking advantage of the hyperspectral convex nature of the observed pixels (Li & Bioucas-Dias, 2008). The hyperspectral pixels inside this simplex are modeled as the linear combination of the representing endmembers.

The geometrical methods at this stage are separated into two categories with respect to the existence of the pure pixels in the data set. If there is at least one pure pixel for each endmember, the unmixing method outputs the vectors in the data set corresponding to vertices of the data simplex as endmembers (Li & Bioucas-Dias, 2008; Bioucas-Dias, 2009). In the case that pure pixel assumption is not fulfilled, which is usually encountered as spatial resolution decreases, the unmixing operation is comparably more challenging as all endmembers might not be represented with pure

pixels in the data set. As an alternative approach, fitting a minimum volume to the hyperspectral observation pixels is pursued to resolve this challenge.

2.2.1 Fast Autonomous Spectral Endmember Determination (N-FINDR)

N-FINDR method is one of the pioneer methods that achieve the unmixing of hyperspectral pixels by assuming the existence of pure pixels in the observed data. The method specifically interprets the pure pixels as the vertices of an N-dimensional scatter plot of observed pixels forming a convex cone. The volume of the simplex formed with such a selection of pure pixels as vertices is assumed as the largest possible volume that can be generated from the observed data (Winter, 1999).

In order to find the maximum volume simplex, N-FINDR first models the hyperspectral pixels as a linear combination of the endmembers:

$$y_i = \sum m_i s_j + n \quad \sum_k s_j = 1$$

Where $Y = [y_1, \dots, y_N] \in R^{p \times n}$ is matrix holding the spectral vectors $y_i \in R^p$ for $i = 1, 2, \dots, n$ in its columns of a hyperspectral data cube. The linear mixing model is defined as $M = [m_1, \dots, m_p] \in R^{p \times p}$ is the mixing matrix. m_i and p stands for the i^{th} endmember signature and number of endmembers respectively. $S \in R^{p \times n}$ is the abundance matrix, where S_{ij} stands for the fraction of i^{th} endmember at j^{th} pixel. The abundance fractions should be greater than zero and sum to 1 for each pixel, which is called as the probability simplex. The hyperspectral vectors y_i belong to a simplex set inside the vertices m_i for $i = 1, \dots, p$. Assuming the linear mixture model, the abundance proportions of a pixel (s_j) sum to one.

N-FINDR algorithm approximates the volume of a simplex as a proportion of the determinant of matrix of endmembers. The algorithm tries to find the maximum

volume which covers the maximum number of hyperspectral pixels with the constraint that the vertices of the simplex are the endmembers corresponding to purest pixels. The algorithm starts with a random set of pixels selected as the vertices and calculates the volume for the selection. This selection is updated when a larger volume is obtained until all the pixels are exhausted in the observed data.

The first advantage of N-FINDR is reported as the identification of pure pixels without any prior information, which simplifies the scope of the problem to a specific feature space. It also removes the obligation to perform atmospheric correction for radiance to reflectance conversion. On the down side, if there is not a complete pure endmember in the data cube, the algorithm assigns the least pixel as an approximation for the endmember. Another disadvantage arises when there is a mixed pixel with a higher brightness, which causes the iterations to be stuck in such points (Winter, 1999).

2.2.2 Vertex Component Analysis (VCA)

Vertex component analysis (VCA) is another pure pixel based method that requires the existence of at least one pure pixel for each endmember (Nascimento, 2015). The main difference of VCA algorithm compared to NFIDNR is to include a scaling factor, γ , into the modelling of observed hyperspectral pixels to account for the illumination differences due to surface topology:

$$r = x + n = M\gamma\alpha + n$$

where r , x , and n corresponds to the same terminology given for Eqn. (1).

In the given equations for (1) and (2), while the geometric place of an observation set, $S_x = \{x \in R^L : x = M\alpha, 1^T \alpha = 1, \alpha \geq 0\}$, corresponds to a simplex in an L-dimensional space, the geometric place of the observations with a scaling factor of γ , $C_p = \{r \in R^L : r = M\gamma\alpha, 1^T \alpha = 1, \alpha \geq 0, \gamma \geq 0\}$ is located in a convex cone. Therefore, the VCA algorithm first performs a perspective projection to project the observed data

to locate on a hyperplane, $r^T u = 1$. The rescaled data after such a projection forms a simplex $S_p = \{y \in R^L : y = r/r^T u, r \in C_p\}$. The u vector for the scaling is selected such that the $r^T u > 0$. In other words, the direction of u should not be orthogonal to any observation pixel to perform perspective projection. After the first projection of data, the VCA algorithm selects the extreme of the projected data as an endmember and then again projects the data onto an orthogonal direction to the selected endmember to extract the subsequent endmember as an extreme of the projected data. The algorithm runs iteratively in order to locate the endmembers to the extreme points of projection until all endmembers are elaborated. VCA method makes a significant contribution to literature as it accounts for the illumination changes for topographical variations and is found to give better or near performances compared to N-FINDR algorithm.

2.2.3 Minimum Volume Simplex Analysis (MVSA)

MVSA is proposed to unmix hyperspectral pixels for the cases when there is not any pure pixel in the observation set formed of only one material for each endmember. The idea of MVSA (Li and Bioucas-Dias, 2008) is to fit a minimum volume simplex to hyperspectral data set with a constraint that the abundance fractions of the endmembers forming each hyperspectral pixel has to be greater than zero and sum to one. The algorithm, as in the other geometric techniques, is founded on a linear model, where the signatures of the endmembers are linearly weighted with the abundance fraction matrix to constitute each hyperspectral pixel. The algorithm softens the positivity constraint of the abundance fractions by also allowing negative values to make the algorithm robust to outliers. However, the negativity is penalized with a hinge function which forces the negative abundance fractions to be as close as to zero. The algorithm initially assigns the endmembers as the endmembers resulted from the VCA algorithm to avoid convergence to a local minima, although such a selection might be far from optimal.

Let $Y = [y_1, \dots, y_N] \in \mathbb{R}^{p \times n}$ is matrix holding the spectral vectors $y_i \in \mathbb{R}^p$ for $i = 1, 2, \dots, n$ in its columns of a hyperspectral data cube. The linear mixing model is defined as

$$Y = MS \quad s.t : S \geq 0 \quad \mathbf{1}_p^T S = \mathbf{1}_n^T$$

Where $M = [m_1, \dots, m_p] \in \mathbb{R}^{p \times p}$ is the mixing matrix. m_i and p stands for the i th endmember signature and number of endmembers respectively. $S \in \mathbb{R}^{p \times n}$ is the abundance matrix, where S_{ij} stands for the fraction of i th endmember at j th pixel. The abundance fractions should be greater than zero and sum to 1 for each pixel, which is called as the probability simplex. The hyperspectral vectors y_i belong to a simplex set inside the vertices m_i for $i = 1, \dots, p$.

The optimization problem for MVSA algorithm is defined as finding the matrix of M which minimizes the simplex volume covering all the hyperspectral pixels in the observation set. The simplex volume in such a problem is approximated by the determinant of the matrix, M . With the given constraint of probability simplex in (1), the problem is given as:

$$M^* = \arg \min_M | \det(M) | \\ s.t : QY \geq 0 \quad \mathbf{1}_p^T QY = \mathbf{1}_n^T$$

where $Q = M^{-1}$.

After the modifications on the constraints, the optimization equation turns to the maximization of Q^* :

$$Q^* = \operatorname{argmax}_Q (\log | \det(Q) |) \\ s.t : QY \geq 0 \quad \mathbf{1}_p^T Q = q_m$$

where $\det(Q) = 1/\det(M)$ and $q_m = \mathbf{1}_N^T (Y_p)^{-1}$.

2.2.4 A Simplex Identification via Split Augmented Lagrangian (SISAL)

SISAL algorithm is again a minimum volume line of attack algorithm. Apart from the MVSA method, the positivity constraint are replaced by soft constraints called “hinge type” constraints. The hard positivity constraint enforces pixel vectors to be included the convex hull formed by endmember signatures. The hinge type soft constraint is applied with a regularization parameter, to penalize the high negative values. This constraint provides a robust algorithm for noise, outliers or poor initializations. The obtained problem is solved by a sequence of augmented Lagrangian optimizations (Bioucas-Dias, 2009). The algorithm is stated to outperform the other state of art techniques like minimum volume simplex analysis (MVSA) regarding with the run time.

Given the l as the number of spectral bands and p is the endmember number, with spectral signatures of $m_i \in R^l$ for $i = 1, 2, \dots, p$ where the algorithm necessitates the endmember number to be less than the number of the spectral bands (*i.e.* $l \geq p$) The algorithm is also founded on linear unmixing model, with the given constraints for minimum volume simplex algorithm, where the abundance fractions for each pixel are non-negative and sum to 1.

$$Y = MS \quad S \in S_p^n$$

Where Y is the spectral vectors, M is the mixing matrix holding endmember spectra and S is the abundance matrix. The volume minimization considering the p -dimensional basis (*i.e.* $p = l$), M is assumed as square and given $\det(M)$ is proportional to the volume of the simplex, the minimization function is:

$$M^* = \arg \min_M |\det(M)|$$

$$s.t : QY \geq 0 \quad \mathbf{1}_p^T QY = \mathbf{1}_n^T$$

where $Q = M^{-1}$.

$$Q^* = \operatorname{argmin}_Q (-\log |\det(M)|)$$

$$s.t : QY \geq 0 \quad 1_p^T QY = 1_n^T$$

where $\det(Q) = 1/\det(M)$.

This is a non-convex optimization problem with convex constraints. The optimization problem finally turns to:

$$Q^* = \operatorname{argmin}_Q (-\log|\det(M)| + \lambda \|QY\|_h)$$

$$s.t : 1_p^T Q = a^T$$

where $\|X\|_h = \sum_{ij} h(|X|_{ij})$ and $h(x) = \max\{-x, 0\}$ called hinge function. The term of

$\|QY\|_h$ penalizes the negative component of QY , proportional to their magnitude.

CHAPTER 3

APPLICATIONS OF ANOMALY AND TARGET DETECTION ALGORITHMS TO DETERMINE OIL SPILLS

Remote sensing for environmental assessment of oil spills is one of the developing paths in hyperspectral image analysis, which enable the designation of oil-contaminated regions. Multispectral and hyperspectral data present a great capability to discriminate oil contaminated regions by making the use of visible infrared (VIS) and short wave infrared (SWIR) bands. The extraction of pixel spectra of an oil-contaminated region from the high dimensional hyperspectral data cube provides the characteristics of the oil polluted area and can be utilized to identify the target over a vast region (Roper and Dutta, 2006). This phenomenon is also valid for the determination of the oil slick over water that is a major support for the environmental management to assess the mitigation of the oil spill and to take necessary precautions.

A detailed literature on the detection of oils spill by remote sensing techniques (i.e. hydrocarbons) is given in Chapter 1.4.1 (b). The necessity to determine the level of oil contamination in marine environment is highly significant considering its potential to spread over vast areas as well as reaching the coastal regions. In the case of an emergence of contamination on water medium, it's imperative to generate a remediation plan as soon as possible, which surely requires the determination of the extent and propagation direction in a timely manner. Salem and Kafatos (2002) conducted one of the earliest studies on investigating oil spills in water medium by utilizing hyperspectral remote sensing. Their study focuses on Chesapeake Bay area which has suffered from oil spill contamination events several times. The airborne imaging spectro-radiometer for Applications (AISA) is utilized to determine spillages in the bay area, to predict the spread direction and flow rate and to identify the severity of the spills on the coastline. Spectral angle mapping (SAM) technique is performed to match the extracted oil signature to image pixels, followed with a thresholding

operation. In the study, the ground truthing is implemented with the help of pictures taken on the day of the event and the capability of spectrum matching over supervised classification is emphasized for determining oil slicks over the water surface. The pioneering studies conducted by Salem and his colleges have encouraged researchers to investigate novel methodologies to determine oil slicks over the complex water medium. With the advancements on the hyperspectral sensors, target detection and anomaly detection algorithms for identifying oil slicks on ocean surface has been focused by several researchers, especially after the oil platform explosion in Gulf of Mexico, 2010 (Alam and Sidike, 2012; Zare-Baghbidi and Humayouni, 2013). Following these studies, hyperspectral unmixing algorithms are applied on hyperspectral images collected over oil-polluted water medium, which is also supported by laboratory measurements to build a database for different type of oils such as crude oils, heavy fuel oils or light petroleum products. The findings indicate the complexity of extracting endmembers in the real case marine environment due to susceptibility of spectrum to change depending on the sea bottom or sea state conditions. It's further mentioned that the methodology is successful to determine oils spills for the studied areas, only being successful to map abundance fractions on currently contaminated regions where only one endmember corresponds to oily areas.

With regard to the extant literature, this chapter focuses on measuring the performance of focused target detection and anomaly detection algorithms for the case of Gulf of Mexico (Alam and Sidike, 2012; Zare-Baghbidi and Humayouni, 2013). The ability of the algorithms in determining the oily regions as well as removal of existing noise on raw data is thoroughly assessed. For this purpose, the algorithms are run without any preprocessing operations.

3.1 Utilized Data and Methodology

In the experiment, we utilize two hyperspectral data sets. The first set, AVIRIS Data set, is collected by NASA after the Deep Horizon Oil platform explosion between May

and October, 2010, in the Gulf of Mexico (AVIRIS, 2015). The radiance spectra collected with AVIRIS instrument, which is the first operational hyperspectral sensor, is aimed to be utilized for examining the constituents of the Earth's surface and atmosphere according to the specific absorption and scattering properties of molecules. The imagery has a high spatial resolution of 7.6 m with 224 bands between 360–2500 nm.

In order to perform a comparison with the literature, the same hyperspectral data sets in the experiments utilized in the research paper of Zare-Baghbidi and Humayouni (2013) are selected. This study utilizes three different anomaly detection techniques, to identify several targets in interest, including detection of oil spills in Gulf of Mexico. The utilized AVIRIS image is acquired from the Gulf of Mexico on May 17, 2010 (Ren and Chang, 2003) in radiance units. For comparison purposes, this image is downloaded from AVIRIS Data Portal https://aviris.jpl.nasa.gov/alt_locator/, which is a publicly available resource for AVIRIS data. A focus region with a spatial size of 179×199 has been clipped from the image for the implementation of the methods in consideration with the subset area in Baghbidi and Humayouni (2013).

As the second data set in the experiments, we utilize hyperspectral data obtained from Gulf of Mexico with SPECTIR sensor on June 6, 2010 in radiance units. The data is publicly available in <http://www.spectir.com/free-data-samples/>. The data cube has a comparatively higher spatial resolution of 2.2 m with 360 spectral bands between 360–2500 nm (SPECTIR, 2015).

This study incorporates two different approaches, namely anomaly detection methods and signature based target detection methods, utilized in hyperspectral image analysis to investigate the oil spill coverage occurred after the explosion of Deepwater Horizon oil platform in April 2010. Utilizing the abovementioned data sets, the methods for anomaly detection are selected as RX, Local-RX, and Gaussian Kernel-RX algorithms, whereas the spectral matched filter (SMF) and desired target detection and

classification algorithm (DTDCA) are utilized for signature based target detection methods. The performance of the selected methods is evaluated with respect to the localization of the targets, noise elimination capability and quantification of the present target abundance with a proper contrast.

3.2 Experimental Results and Comparisons

We implement the three anomaly detection methods and two signature based target detection methods on the mentioned two data sets. The utilized data are inputted to the algorithms without any preprocessing and dimension reduction operation to fairly examine the performance of oil spill detection with the raw hyperspectral radiance data among different methods. As there is no provided ground truth for the data sets, the obtained results are visually evaluated with respect to the localization of the targets, noise elimination capability, and quantification of the present target abundance with a proper contrast. Both anomaly detectors and signature-based methods are compared with each other as well as within themselves.

For a better understanding, the original data sets and their corresponding anomaly detection algorithm outputs in the study of Zare-Baghbidi and Humayouni (2013) are given in Figure 3-1 and Figure 3-2. In reference to these outputs, the performance evaluation of the applied algorithms in our study is implemented taking into account the delineated oil spill pixels, which are shown in white color in the output images of Zare-Baghbidi and Humayouni (2013), as well.

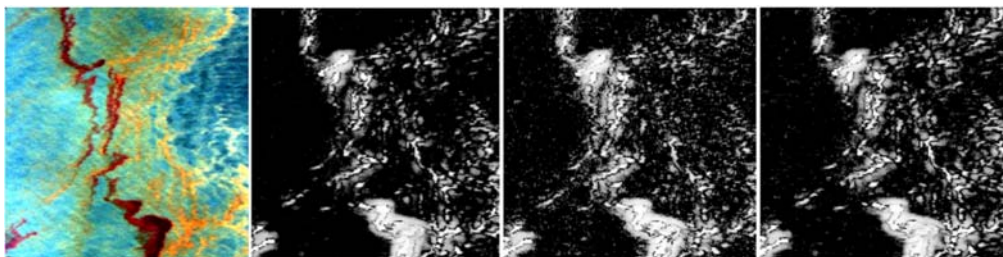


Figure 3-1 AVIRIS image and anomaly detection algorithm outputs (Zare-Baghbidi and Humayouni, 2013)

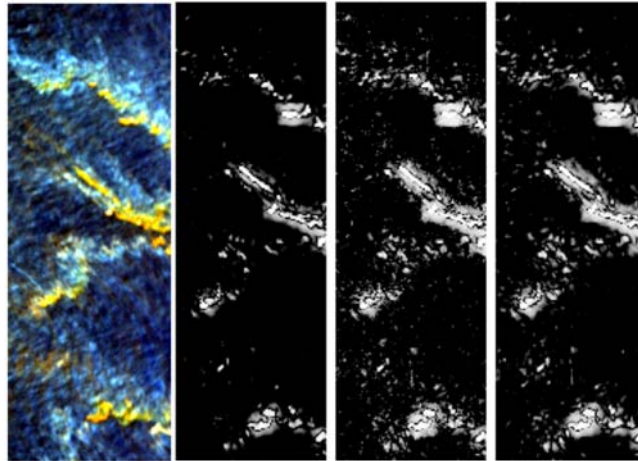


Figure 3-2 SPECTIR image and anomaly detection algorithm outputs (Baghbidi and Humayouni, 2013)

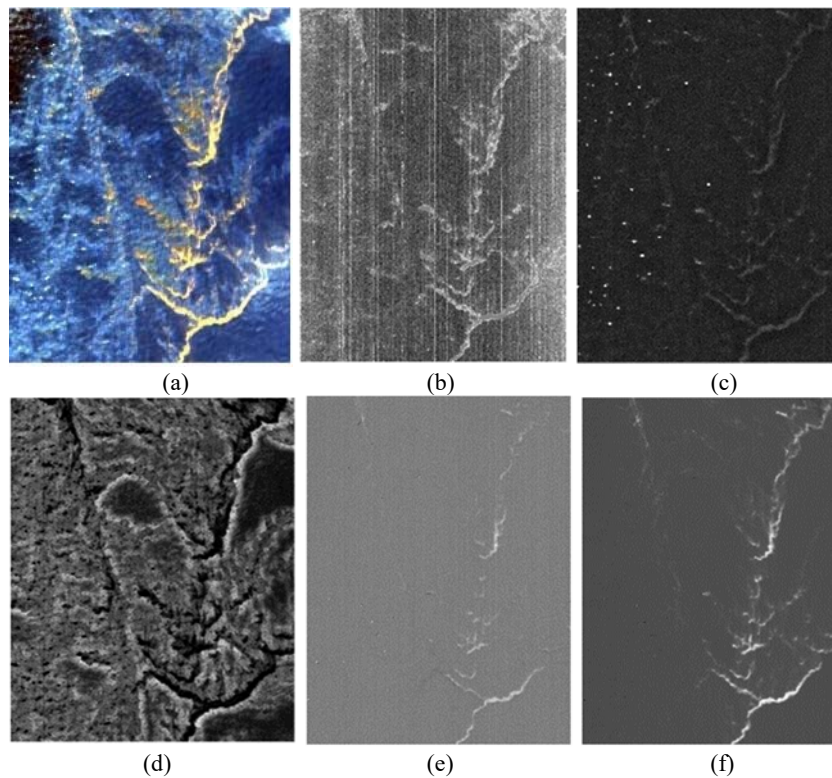


Figure 3-3 Algorithm Results on SPECTIR Imagery a) True Color Composite b) Global RX c) Local RX d) Gaussian RX e) SMF f) DTDCA

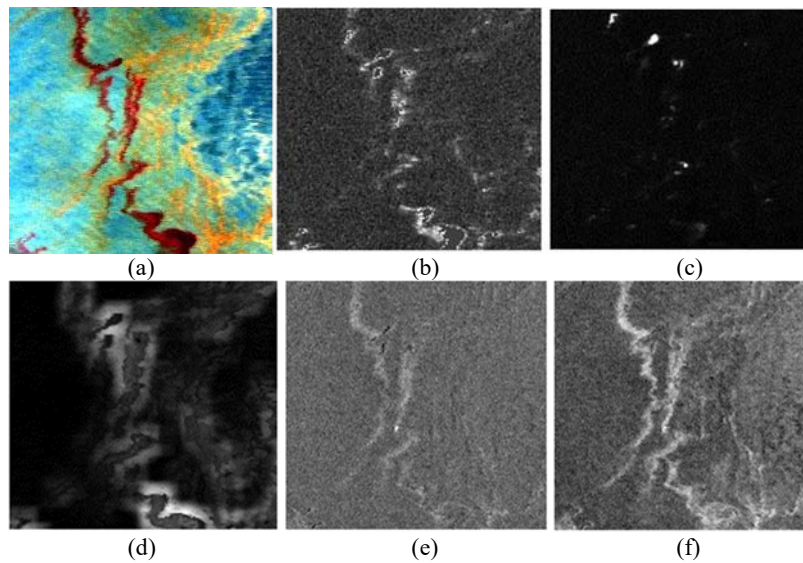


Figure 3-4 Algorithm Results on AVIRIS Imagery a) True Color Composite b) Global RX c) Local RX d) Gaussian RX e) SMF f) DTDCA

Figure 3-3 and Figure 3-4 illustrate the results of the implemented algorithms in this study for AVIRIS and SPECTIR data sets, respectively. Among the presented results for the three anomaly detection algorithms (Figure 3-3 - (b, c, d) and Figure 3-4 -(b, c, d)), the results for the global RX is suffering from noisy components both emerging in the form of individual spikes and vertical lines. As some of the hyperspectral bands could be very noisy, the effect of these bands to the global RX algorithm is severely degrading the performance. This degradation is partially suppressed for the case of local RX with the eliminated vertical lines on the results, although the spike noises can still be observed. The Gaussian RX, on the other hand, eliminates both the vertical lines and spike noises. However, the disadvantage of Gaussian RX besides its high computational time is its inability to properly catch the right contrast for the target abundance at every time. The proper visualization of the target abundance on the obtained results requires a fine tuning of the parameters utilized in the Gaussian RX, such as the size of the kernel window as well as the variance of the fitted distribution.

Signature based target detection methods on the other hand (Figure 3-3-(e, f) and Figure 3-4-(e, f)) have revealed a significant performance in noise elimination compared to the anomaly detection methods. Both the vertical lines and the spike

noises are eliminated on the illustrated outputs. In addition, the visual interpretation of the outputs also reveal that signature based algorithms provide a good contrast regarding the quantity of oil slicks for both images as illustrated in Figure 3-5- (a, b). Going from blue to the red color, the change in the abundance of the oily regions is well observed on the output images. It is also concluded that among the signature based target detection methods, DTDCA is better than the SMF method in both locating the oil spill regions and showing its abundance with a good contrast.

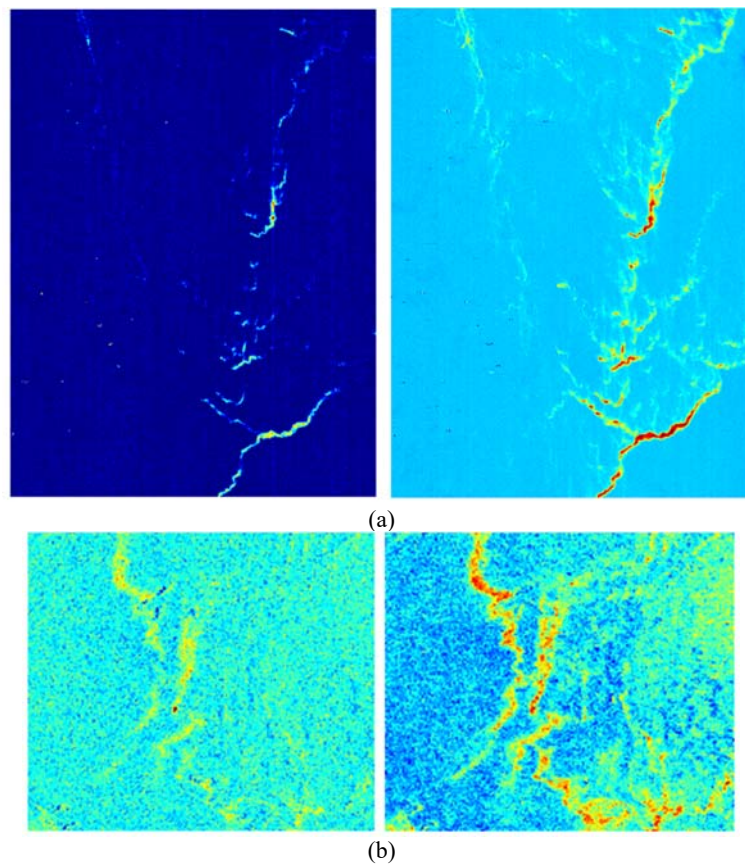


Figure 3-5 SMF (left image) and DTDCA (right image) Results on (a) SPECTIR Imagery and (b) AVIRIS Imagery

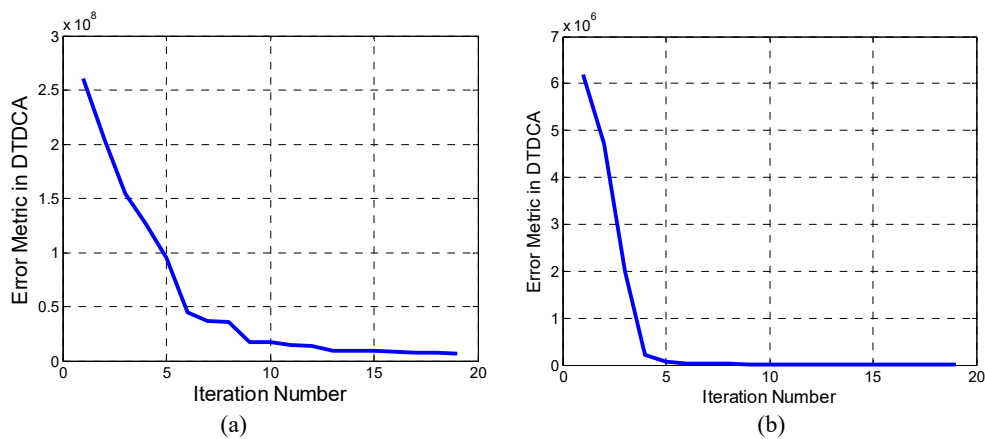


Figure 3-6 DTDCa Error Metrics (a) SPECTIR (b) AVIRIS

In Figure 3-6, we present the change of the error terms with the numbers of iteration in DTDCa algorithm for both imageries. The error term is saturated after reaching to a point, which indicates that the given number of iteration is sufficient to filter out the target oil components from the water forming the background in the acquired scenes. To further elaborate on the delineated oil spill pixels, after a thresholding operation, the radiance signatures of water surface with and without oils is plotted. By this way, discriminative features of oil radiance spectral fingerprints are investigated. Figure 3-7 illustrates the regions of oil spills in white color.

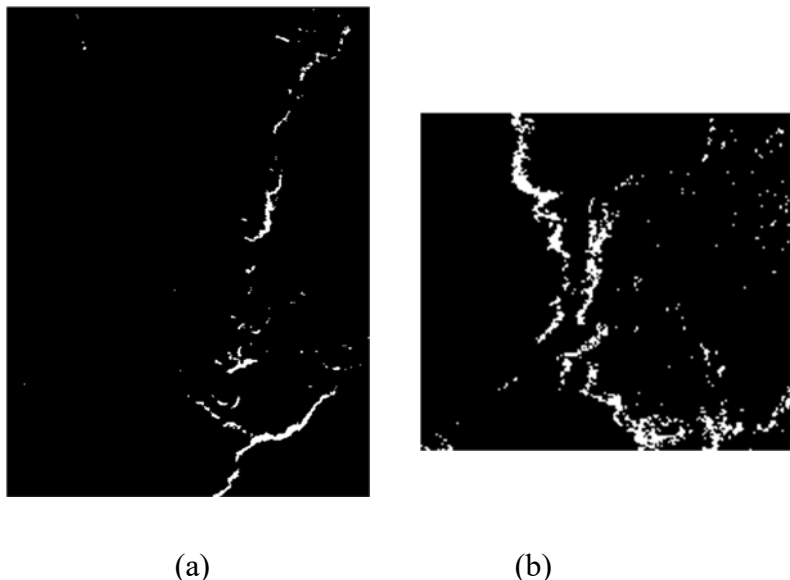


Figure 3-7 Oil bearing pixels, shown in white color, after thresholding operation (a) SPECTIR (b) AVIRIS

The plotted signatures reveals the higher capability of SPECTIR data to resolve the spectrum due to its high spectral resolution. It resolves the features of the signatures in a more detailed manner compared to AVIRIS extracted signatures. Although it's hard to differentiate specific absorption features of oil bearing pixels due to water, carbon dioxide and ozone absorptions in the radiance signature, relatively higher radiance values, particularly in VNIR region, are observed in the signatures extracted for both images, especially in SPECTIR data cube. Having said that, the absorption depth of the pixels with oil content is expectedly deeper than the regular water radiance spectrum. Furthermore, it is important to note that the radiance signatures of oil-bearing pixels and the non-oil bearing ones are gathered within their belonging groups, which actually proves their separability from each other. The two groups are more distinctive in SPECTIR data showing a significantly different trajectory, which is not the case for AVIRIS image. The signatures have a common continuum unlike the SPECTIR ones that is attributed to the lower spectral and spatial resolutions of the AVIRIS data cube. All of these outputs supports the susceptibility of oil spectrum depending on its thickness, sea bottom and sea state conditions.

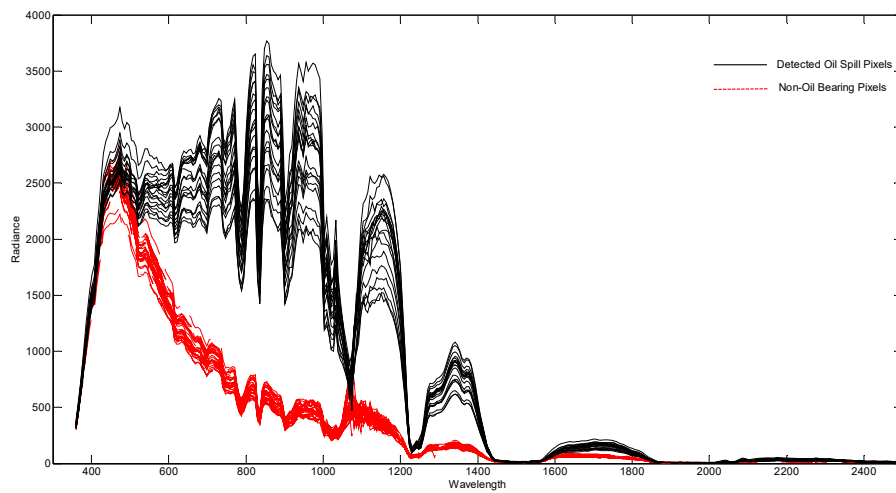


Figure 3-8 Radiance signatures of pixels with and without oil content (SPECTIR)

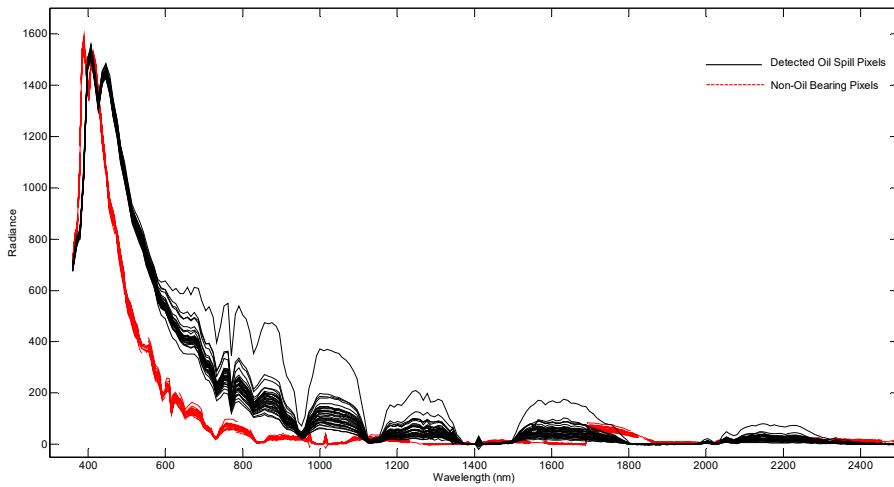


Figure 3-9 Radiance signatures of pixels with and without oil content (AVIRIS)

According to the overall experimental comparisons, the results indicate the superiority of signature based methods over anomaly detectors in eliminating the noise, detecting the contaminated regions, and showing the abundance of pollution. In particular, DTDCa algorithm gives the best results among all the compared methods with its background elimination algorithm, which effectively filters out the undesired components from the observed data before the matching with the target signature.

CHAPTER 4

MAPPING HYDROCARBON INDUCED ANOMALIES WITH HYPERSPECTRAL TECHNIQUES

In this section, signature based detection algorithms and hyperspectral unmixing methods in detection of hydrocarbon microseepage anomalies are compared. Among the unmixing algorithm outputs, the extracted signature, i.e. endmember that is angularly closest to the reference spectra is selected and its abundance map is utilized as a baseline for performance comparison. The experiments indicate that SISAL algorithms give out the closest signature to reference/ground truth spectra between the designated band intervals of hydrocarbon signatures with an error value of 0.05, outperforming all unmixing algorithms, MVSA, VCA and N-FINDR respectively. Knowing the fact that the extracted signature is angularly closest to the reference hydrocarbon spectral samples, the abundance map of SISAL is employed as a baseline to measure the similarity among the other algorithms, with Euclidean metrics accordingly. The experiments support the findings and assessment of the first phase of the study with the results of DTDCa and MF outperforms the traditional Crosta techniques by locating the microseepage patterns along the mitigation pathways with a better contrast, following the success of unmixing algorithms. On the other hand, pure pixel based unmixing algorithms, N-FINDR and VCA, as well as Correlation and Normalized Correlation have not been able to map the searched target with a visible distinction, with an exemption of VCA merely highlighting the main pathway of the hydrocarbon seepage. It is concluded that unmixing algorithms can be more effective than signature based algorithms and conventional methods for the detection of microseepage-induced anomalies.

As mentioned earlier, to map hydrocarbon microseepage regions utilizing two main sets of algorithms, signature based algorithms and unmixing algorithms. Signature based algorithms require a prior knowledge about the spectral characteristics of the

target, which can either be a single spectrum or a subspace defining it, in order to determine the possible locations. Unmixing algorithms, on the other hand, are unsupervised techniques that are used to identify the components in each observation pixel of a data cube, their spectral signatures with the corresponding abundance fractions. In this paper, ASD spectrometer data collected from the field (Avcıoğlu, 2010) and an ASTER image of the study area located in the Southeastern Anatolia, are compiled for the analysis. After the atmospheric correction of the image, the spectral signatures collected from the field are resampled to be used for running the algorithms. As a baseline for the comparisons, first the well-known traditional technique for hydrocarbon-induced alteration mapping called Crosta technique is implemented. The Crosta technique utilizes principal component transformation to obtain eigenvectors to highlight the target material in consideration with its spectral properties. This baseline method is compared with signature based target detection methods which are selected as vector correlation, normalized correlation (NC), spectral matched filter (Hwon & Nasrabadi, 2004) and desired target detection algorithm (DTDCA) (Ren & Chang, 2003). From the simplest to the most sophisticated, while correlation and normalized correlation is calculating vector similarities between the ASD signatures and captured pixel spectra, spectral matched filter and DTDCA utilize also the background information by using the covariance and the spectral signatures of the background. In addition to the supervised signature based methods, four different hyperspectral unmixing algorithms are applied to the data cube for hydrocarbon induced alteration mapping. As an unsupervised approach, unmixing algorithms result in several abundance maps together with their spectral signatures (i.e. endmembers), providing another measure to evaluate the performances of the resultant maps. N-FINDR (Winter, 1999), Vertex Component Analysis (VCA) (Nascimento, 2005), Minimum Volume Simplex Algorithm (MVSA) (Li & Bioucas-Dias, 2008) and Simplex Identification via Split Augmented Lagrangian (SISAL) (Bioucas-Dias, 2009) are the hyperspectral unmixing methods applied in this research. Not only applications of advanced spectral signature algorithms but also hyperspectral unmixing techniques in the context of microseepage induced anomaly detection

contribute to the literature significantly with this novel methodology. The in-group and between group comparisons of these methods further serve as an improvement of hydrocarbon microseepage mapping, with an overall performance evaluation between the state of art algorithms and traditional Crosta technique.

4.1 Utilized Data and Methodology

In this section, we aim to evaluate the performances of signature-based algorithms and hyperspectral unmixing methods to map hydrocarbon microseepage related alterations. The selected data for the analysis is the multispectral ASTER image of the region. Only the visible and shortwave infrared region of the image is utilized, with a prior resampling of the SWIR bands to 15-meter resolution. Following that, the image is atmospherically corrected and clipped to the study region, Gemrik Anticline. In the first part of the study, besides the signature based algorithms, we apply the well-known traditional CROSTA technique to map the hydrocarbon microseep regions, which also was applied in a previous study as a baseline (Avcioglu, 2010). In the second part, the unmixing algorithms are also applied to the atmospherically corrected dataset to determine the success of the endmembers extracted from this multispectral scene to delineate the hydrocarbon microseepage regions. The endmembers, which are restricted to the maximum band number of the data cube, are utilized to produce abundance maps. The acquired endmembers are compared with the spectral signature of the reference microseep regions collected during the fieldwork using spectral angle mapping algorithm (Avcioglu, 2010). As a result of this comparison, angularly closest endmember to the ASD reference spectrum, which is resampled to ASTER resolution, is assigned as the one corresponding to hydrocarbon microseeps. The error terms are also regarded as a performance indicator. The abundance map corresponding to the minimum error endmember is employed as a reference to comprehend the performance of the signature based algorithms as well.

4.2 Experimental Results

In this study, we investigate the performance of two groups of algorithms, i.e. signature based methods and unmixing techniques, to determine their performance for hydrocarbon microseepage mapping. In the following subheadings, we evaluate the algorithms outputs within their belonging groups as well as between groups for mapping the hydrocarbon microseepage locations in our study area.

a) Comparative Results – Signature Based Methods

For a fair comparison in the experiments, no post processing operation was applied on the resulting target abundance maps. In order to differentiate the target pixels and get a better visualization of the microseepage regions, color map ‘jet’ with an increasing content of the target from blue to red is utilized. The collected spectral signatures from the reference valley is shown in Figure 4-1 (a), with the resampled ones to ASTER spectral resolution in Figure 4-1 (b).

Figure 4-2 (a, b, c, d, e, f) shows the algorithm outputs for each of the method with the reference valley of the collected spectral samples. The outputs of the signature-based algorithms seem to be compatible with the traditional technique CROSTA except for the correlation/normalized correlation results. According to the acquired microseepage maps, the hydrocarbon locations are much more profound in signature-based techniques with an enhanced contrast, presenting an extra information about the content of microseeps as well. Considering the distinguishability of the searched target from the background, DTDCA is regarded as a much more reliable algorithm as it removes the background components from the test pixels before the matching operation compared to SMF. As mentioned earlier, the correlation algorithm is only successful at separating the anticline from the whole region that covers the delineated patterns by the compared techniques. Unfortunately, normalized correlation removes the target region completely, even for the case of anticline region.

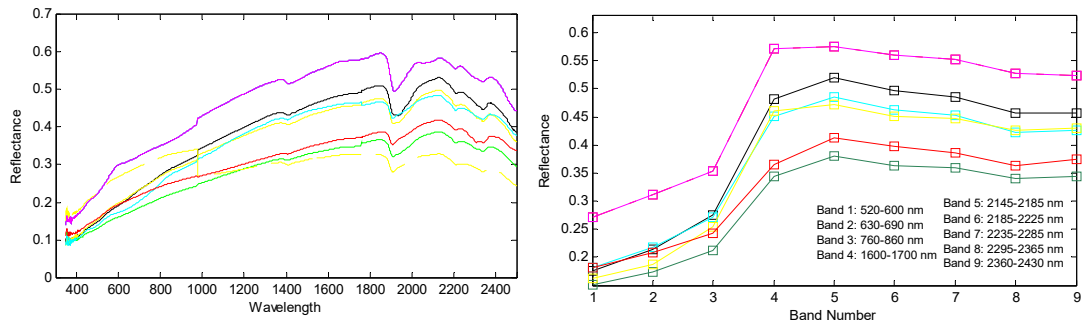


Figure 4-1 a) Spectral Signatures of Hydrocarbon Microseepage Samples Collected with ASD b) Signature Resampled to ASTER Spectral Resolution

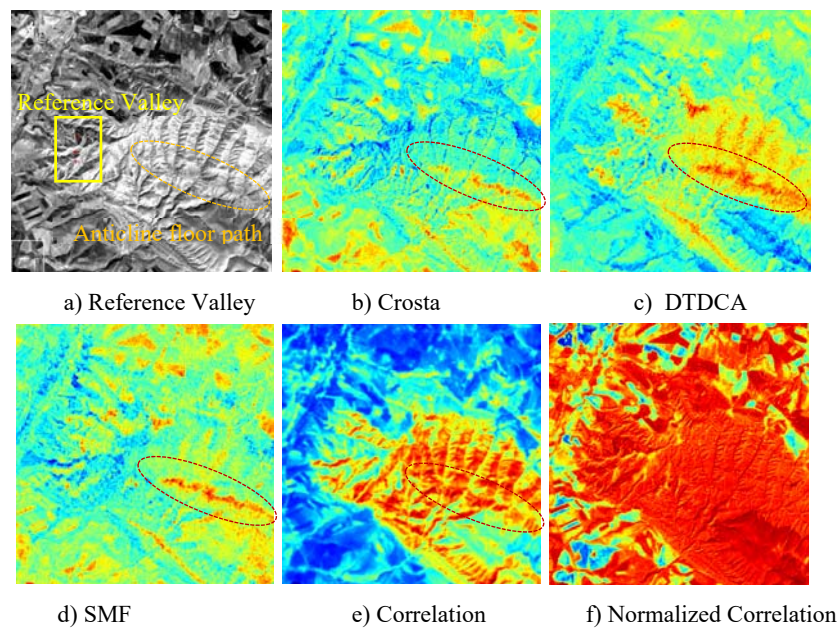


Figure 4-2 Signature Based Target Detection Algorithm Outputs

The implementation of the signature-based algorithms gives encouraging results for hydrocarbon microseepage detection with signature based target detection methods. DTDCa and SMF algorithms stand as the most promising ones regarding with the outputs of the traditional technique CROSTA and correlation/normalized correlation methods.

b) Comparative Results -Unmixing Methods

A comparison and performance evaluation of selected unmixing algorithms is presented. Pure pixel based algorithms, N- FINDR and Vertex Component Analysis (VCA) as well as the algorithms selected for the cases of the violation of pure pixel assumption, the Minimum Volume Simplex Analysis (MVSA) and Simplex Identification via Split Augmented Lagrangian (SISAL) are evaluated for their capability to delineate microseepage regions. As stated earlier, unmixing algorithms results in endmembers (i.e. spectral profiles of each constituent) as well as the regarding abundance maps for each endmember. As a result of the unmixing application, the acquired nine endmembers are analyzed to differentiate the angularly closest signature to collected spectra from the field to select the microseepage related endmember, using spectral angle mapping method. This method results in the errors between each endmember and the reference signature collected from the microseepage field. For this particular case, we propose a methodology to track the errors regarding with a certain interval of the shortwave infrared region of ASTER image, knowing the fact that the hydrocarbon absorption bands are closely related to that region, especially considering the absorption band of $1.73\mu\text{m}$ which is a unique characteristics band for the calculation of hydrocarbon index (Kuhn et al.,). Figure 4-3 illustrates the output endmembers of each unmixing algorithm with the reference signature collected from the field and the spectral range evaluated to measure the algorithm outputs.

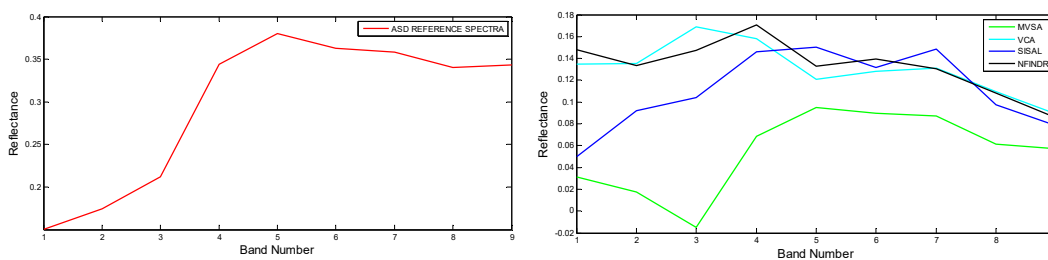


Figure 4-3 Endmember outputs corresponding to the microseepage regions

Although the trend of the extracted spectral signatures especially differs in visible region, the algorithm outputs show a significant compatibility along the SWIR Bands 4-7, covering the range of 1650-2260 nanometers for all endmembers corresponding to microseepage regions. This inference is supported with spectral angle mapping techniques mentioned earlier, resulting in the error terms related to the microseepage endmember of each unmixing algorithm and reference spectrum. In addition to delineating a specific region along a known path of seepage of all algorithm abundance fractions, the error terms calculated using the reference signature and microseepage endmembers point out the outperforming unmixing algorithm among the others. Table 1 shows the error terms of each endmember with reference spectrum, minimum values corresponding to microseepage fraction in the study area. The results reveal that SISAL algorithm outperforms all algorithms with a minimum error term of 0,05 compared to the utilized unmixing techniques. The abundance fractions corresponding to microseepage endmember of each unmixing algorithm is also given in Figure 4-4. As a representative sample, all abundance maps corresponding to each endmember of SISAL algorithm is illustrated in Appendix A.

Table 4-1 Error terms calculated using the reference signature and extracted endmembers with SAM algorithm

ALGORITHMS	ENDMEMBERS								
	1	2	3	4	5	6	7	8	9
NFINDR	0.23	0.24	0.16	0.19	0.15	0.14*	0.28	0.17	0.23
VCA	0,24	0,15	0,19	0,15	0,22	0,18	0,28	0,13*	0,17
MVSA	2,98	0,08*	0,22	0,63	2,66	0,73	0,37	0,12	0,18
SISAL	1,65	0,12	0,21	0,05*	2,73	0,30	2,58	0,14	1,25

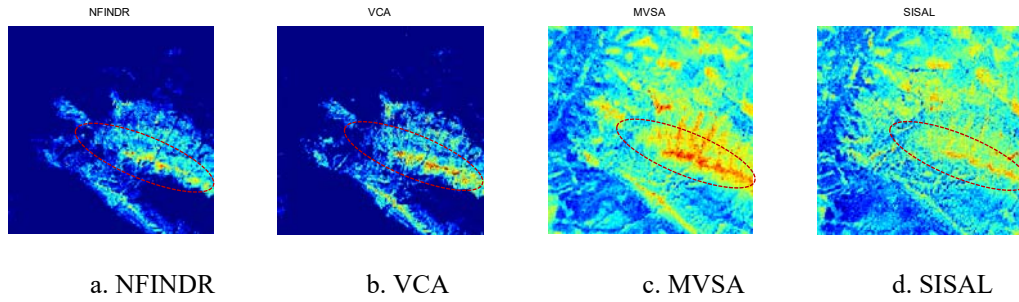


Figure 4-4 Abundance fractions corresponding to microseepage endmember of each unmixing algorithm

All unmixing algorithms except for the N-FINDR technique highlight the fractions related to microseepage regions along the known path of seepage. The red pixels depict the highly concentrated regions with a decreased content to blue color. N-FINDR algorithm promotes the anticline region, which is highly distinguishable with visible spectrum. Comparing the other three techniques, the lineament of microseepage can be traced along a path in Gemrik anticline with high contents. The output fractions of MVSA and SISAL algorithm seem vastly compatible with difference in contents, pointing out the same lineaments. The VCA algorithm, on the other hand, eliminates the background other than MVSA & SISAL, highlighting only the pure pixels covering the main microseepage path.

c) Signature Based Methods vs. Unmixing Algorithms

The algorithm results have been compared within each group in Section 5.1 and Section 5.2 so far. This part of the study aims to perform an assessment considering all acquired outputs to make a fair comparison. According to the in group assessments of signature based techniques, Spectral Match Filter (SMF) and Desired Target Detection Algorithm (DTDCA) give outputs that are highly similar with the traditional Crosta technique visually. We utilize the ASD spectra of the collected samples as a ground truth to select a baseline map among unmixing algorithm outputs with the help of angular metrics. Moving from this point, a simple Euclidean metric, $L2 Norm$, is selected to measure the similarity of each image pair, SISAL abundance map as the

baseline, as well as comparing both foreground and background discrimination of acquired outputs; foreground being the microseep regions. The expected metric should be minimized for the similar outputs indicating the compatibility between foreground and background.

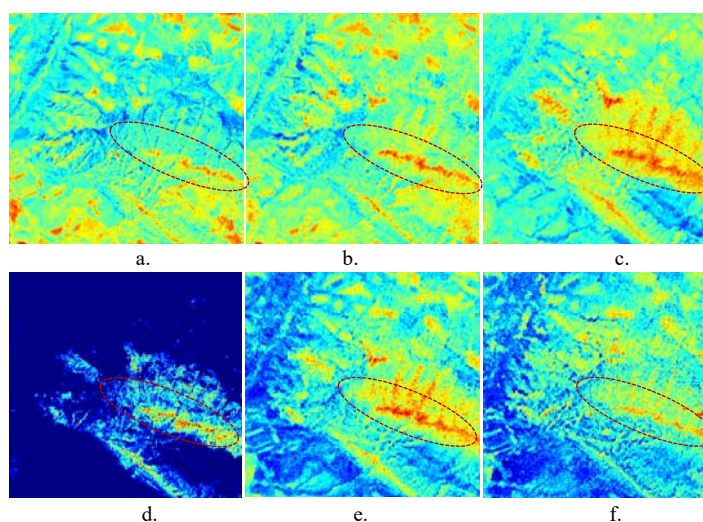


Figure 4-5 The algorithm outputs a) Crosta b) SMF c) DTDCA d)VCA e)MVSA f)SISAL

Table 4-2 Root Mean Square Error Metrics between SISAL and other algorithms

	CROSTA	DTDCA	SMF	VCA	MVSA	N-FINDR
SISAL	0.1950	0.1391	0.1927	0.3550	0.0942	0.2948

Table 4-2 demonstrates the results of the error metrics. Evaluating the acquired outputs of unmixing algorithms, the error term related to the VCA algorithm is the highest amongst the other results. This expected effect is interpreted as a result of pure pixel assumption of the VCA algorithm, which ignores composite spectrum to select the endmembers. The same interpretations are also viable for the N-FINDR algorithm, which has the second highest error values. The error value for the MVSA is the closest to the SISAL among all the algorithms, which is proportional to its spectral angle error to ground truth signature. When all applied unmixing abundance maps are investigated, it is concluded that the pure pixel based algorithms output pixels, efficiently pointing out the microseepage pathway along the syncline path, as it is

executed with pure pixel endmembers. This pathway is identified as a common lineament for all algorithms. The SISAL and the MVSA are much more efficient in mapping the abundances of the hydrocarbon seeps with minimum spectral errors within the range of designated band intervals. These two methods also have a potential to highlight the other anomaly pixels rather than the migration pathway along the anticline, as they are operated when the pure pixel assumption is violated. The signature based target detection algorithms, which are visually compatible with unmixing algorithm results with some variances in the study area, have well-matched error metrics with the visual assessments as well. The DTDCAs are regarded as the most successful algorithms among the signature based techniques, followed by the SMF and Crosta subsequently. The background elimination of the DTDCAs supports these findings with the removal of background components before the signature matching operation.

The experiments indicate that advanced spectral detection techniques have a great potential to reveal hydrocarbon microseepage induced anomalies. The presented results of signature based target detection techniques, as an in-group assessment, successfully highlight the hydrocarbon microseepage locations other than the correlation and the normalized correlation algorithms. Compatibility of signature based target detection algorithm results is observed with the traditional Crosta technique for allocating the microseep regions with a better contrast, which provides better understanding about the content of the searched target. The results have also shown a good match with the field based research performed by Avcioğlu (2010), which forms a base for the utilization of signature based techniques in the region. The unmixing algorithms, giving an opportunity for performance evaluation as well as additional abundance maps, give more resourceful results compared to the signature based target detection methods. The implemented algorithms in this study also delineate the prominent clay alterations, which were emphasized in the study of Avcioğlu (2010). Having the bands abundantly utilized for mapping clay alteration in mind (Band 4 to Band 7 corresponding to 1600-2285 nm), SISAL algorithm is

regarded to present the most trustworthy results, with the closest endmember to reference signature in the specified band intervals among all the algorithms. According to the RMSE values and the endmember trends, SISAL is followed by the MVSA technique, which can also be seen visually. Furthermore, the N-FINDR and the VCA algorithms are found to be successful only for promoting the pixels in the anticline region, blurring the background other than the anticline. These results are explained by the fact that both algorithms belong to pure pixel based group, which exploit overall pixel spectrum to select endmember representing the microseepage-induced alterations. This study presents the capability of hyperspectral unmixing techniques, which are performed without any prior knowledge of the searched target spectra (i.e. endmember), on a multispectral data cube not only to resolve the hydrocarbon induced components but also to produce abundance maps with related error metrics. It is further inferred that the proposed methodology reveals a comprehensive understanding of output maps with the additional error calculation stage.

CHAPTER 5

MAPPING TOPOGRAPHICAL ANOMALIES FOR AN ABANDONED COAL MINE

Coal production and utilization has been a significant factor on environmental pollution. Carbon dioxide emissions due to burning coal is one of the forthcoming problems regarding with it. According to the yearly report of Turkey Electricity Generation Company report published in 2012, fossil fuel related carbon dioxide emissions have increased % 115 in the last 39 years, reaching at levels of thirty million tons. Coal's share within this emission has also amplified % 152 corresponding thirteen million tons, which is % 43 of the total carbon dioxide emission. Together with the air pollution levels, soil pollution is another impact of coal mining operations and thermal plants. The researchers has been studying on this important issue, especially with the state of art technologies in recent years. The correlation between the coal mining activities and heavy metal contaminations (cadmium, copper, lead, zinc) around the mine site as well as contamination in stream sediments are presented in the literature (Li et al., 2014; Wong, 2003). The acidic mine effluents carrying high levels of cationic ions such as calcium, magnesium, potassium or heavy metals dominated precipitations around the abandoned coal mining area in spite of the reclamation activities.

At the end of 2012, the power generation by coal power plants is reported to be 12.5 GW and it corresponds too % 22 of the total power generated in Turkey. The local coal production provides 8613 MW energy, which cover 15,3 % of the reported value (Electricity Generation Company Reports, 2012). Unfortunately, the physical or chemical properties of produced coals in Turkey has not been collected and stored in government organizations properly. That's why, a database regarding to the characteristics of each establishment could not be attained or generated. However,

considering its share in energy production, the requirement for matching the environmental legislations on the supervision of mining activities stands as a must.

The environmental sustainability of mining operations, which is a great challenge that comprises of minimizing the impacts on the surrounding environment, requires state of the art methodologies and tools to reduce the anticipated effects. The main purpose of this section is to determine the anomalies regarding with the coal mining operations in an abandoned coal mine site in central Anatolia by multi-temporal image analysis of Landsat 4-5 surface reflectance data. A well-known anomaly detection algorithm, Reed-Xioli (RX), which calculates square of Mahalanobis metrics to calculate the likelihood ratios by normalizing the difference between the test pixel and the background to allocate anomaly pixels, is implemented across the time series. The performance of the algorithm is also quantified with Receiver Operating Characteristics (ROC) curves and precision-recall graphs to quantify its capability on Landsat Thematic Mapper (TM) multispectral image series.

Despite having a great potential to reveal detailed information on earth surface, availability of hyperspectral scenes for public use can be either extremely hard or quite costly. As the acquisition of hyperspectral images is challenging or comparably expensive, this study is motivated to determine the performance of well-known hyperspectral anomaly detection algorithm, Reed-Xioli (RX), on multispectral images of Landsat 4-5 Surface Reflectance data, which are currently provided as new products by Unites States Geological Survey (USGS). In the scope of the methodology, available and reliable images before-during-post mining activities are downloaded considering the noise & cloud covers of each of them. An intermittent temporal series of reflectance imagery set between the years of 1985-2011 are utilized for the analysis.

5.1 Utilized Data and Methodology

Landsat Thematic Mapper 4 and 5 (TM4 and TM5) multispectral data sets are selected for tracing temporal change in the abandoned coal-mining region. The study area is located in Central Anatolia, in the city of Çankırı. Mining operations have lasted 18 years starting from 1987, which were completely ceased in the late 90s. In addition, having known the operational life of the mine and there were no actions taken in the region for mine reclamation & rehabilitation, this mine site is a good candidate which would serve to the purpose of this research. United States Geological Survey (USGS) started to release higher-level products of Landsat 4-5 scenes at the end of 2014, which was acquired between 1982-2012, including surface reflectance products, Top-of-Atmosphere reflectance and NDVI images. Availability of this application ready historical dataset is regarded as invaluable for pursuing the motivation of this study in order to be able to monitor the transformation in the terrestrial environment of mine site. The surface reflectance data is publicly available via <http://earthexplorer.usgs.gov/>, while the users have to fill out an order form to acquire TOA reflectance and NDVI images through <https://espa.cr.usgs.gov/>. The technical properties of utilized Landsat TM images are given in Table 1 (Taylor, 2017).

Landsat TM surface reflectance data is delivered without the Band 6, which covers the thermal region among the other bands. After the acquisition of images, the delivered bands are stacked to form the data cubes of six bands (Bands of 1-2-3-4-5-7), and the focus area around the abandoned coal mining site is subsetting from the whole region. Both global RX and local RX anomaly detection algorithms are implemented across the time series to identify the pixels standing out against the defined background. The high score anomaly pixels in the output image sets are selected using multi-thresholding technique based on the Otsu method as the technique presents extra information of segmentation metric for performance evaluation. After generating the high score anomaly score matrixes for each year, the common indexed anomaly pixels are plotted to make an inference about their attained scores across the years. Furthermore, in order to measure the performance of the algorithms, Receiver

Operator Characteristics Curves (ROC Curve) and Precision-Recall Curves (Davis and Goadrich, 2006) are plotted temporally. Figure 5-1 illustrates the followed steps of methodology in detail.

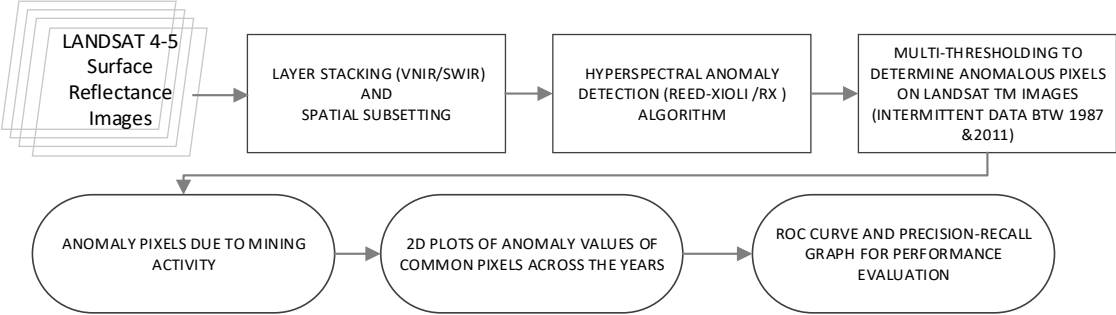


Figure 5-1 The Flowchart of the Methodology

5.2 Experimental Results and Comparisons

The algorithm computes anomaly scores of each pixel vector of the data cube and highlights the irregularities with respect to point cloud in consideration. The global RX method models the background by including all observation pixels, that would mostly regarded as insufficient to catch the anomalies. Moving from this point, a local definition for background modeling with a double concentric window to single out distinguished pixels is proposed for a better performance. In this case, the background pixels are selected within a certain boundary covering around the test pixel. A double concentric sliding window is created for defining either of the variables, i.e. test pixel and background matrix. The proposed application to compute local neighborhood to find anomaly pixels is called as local-RX algorithms in the literature (Nasrabadi, 2014).

In line with this information, algorithm performances are calculated utilizing well-known ROC Curve and Precision-Recall plots (Davis and Goadrich, 2006). ROC curves and precision-recall graphs are commonly utilized for evaluating binary classification problems in machine learning. The former depicts the relation between the number of pixels classified correctly and the number of falsely classified negative

observations; while the latter shows the relation between the number of instances classified correctly and number of correctly classified samples out of the positive sample set. These two methods can be used interchangeably, though the precision recall curves are referred as providing more trustworthy results with a highly skewed data set (Davis and Goadrich, 2006). It is also noted that these two graphs are highly interconnected, which means a dominating curve in ROC space is only possible when it shows the same tendency in precision-recall space. The required counts of the selected anomaly pixels for each year based on whether or not they fall in mine layout regions are computed according to the equations given below.

$$\text{TruePositiveRate} = \text{TruePos} / (\text{TruePos} + \text{FalseNeg})$$

$$\text{FalsePositiveRate} = \text{FalsePos} / (\text{FalsePos} + \text{TrueNeg})$$

$$\text{Precision} = \text{TruePos} / (\text{TruePos} + \text{FalsePos})$$

$$\text{Recall} = \text{TruePosRate} = \text{TruePos} / (\text{TruePos} + \text{FalseNeg})$$

The experimental results in time series reveal high score anomalies quite compatible with the mine development. According to the visual comparisons, the anomaly scores are allocated in the open-pit, coal storage, excavations & area of disturbances of the land as well as the dumpsites throughout multi-temporal images, which reveal the differentiations on earth surface across the years. The annual change rates of the anomaly pixel values are also found to relate to the nature of alterations in the land, as the pre-mining images ensures to evaluate the deviations of the expected anomaly scores in the land even before the mining operations start. Global RX algorithm outputs visualized with a jet color map, scores increasing from blue to red, is presented in Figure 5-2. Although the detected high score pixels can vary across the temporal scale, it can be visually interpreted that they tend to stabilize starting from the end of 90s, coinciding the end of active mining activities. With the knowledge of each image is acquired in different seasons of the year and times of the day, this variation, which

would potentially create a basis for dynamic threshold requirement, is presumed earlier.

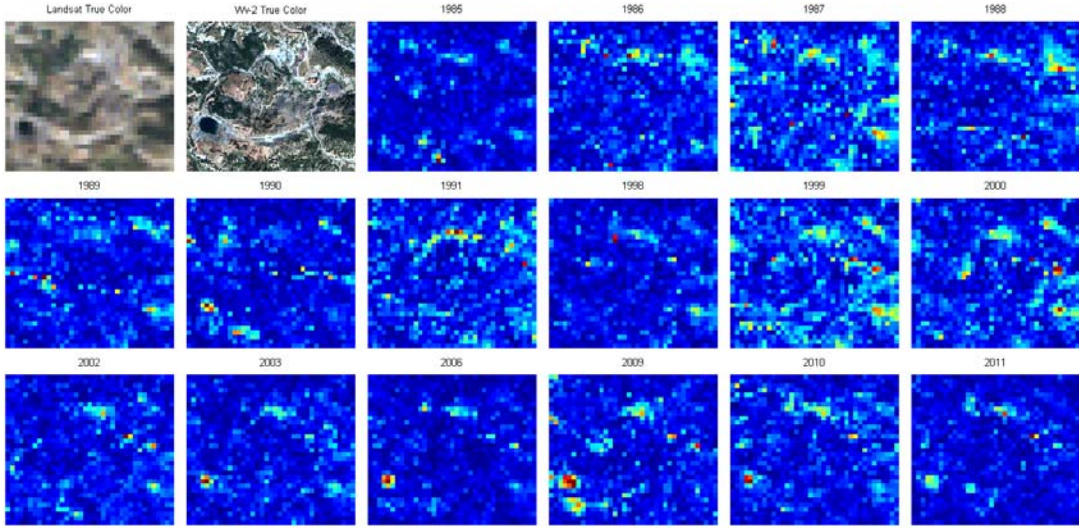


Figure 5-2 RX Anomaly Algorithm Outputs in Multi-Temporal Landsat Images

The high score anomaly pixels in the global RX output image sets are selected using multi-thresholding technique with the help of Otsu method, which also provides an additional segmentation metric to indicate the effectiveness of applied threshold value for each image in time series. The calculated mean threshold value computed with Otsu method for the time series is 0.20, with an overall effectiveness of 0.60. Figure 5-3 shows a high resolution image of the mine site with its layout (Figure 5-3.a), together with the selected high score pixels as a result of the thresholding operation in image 2011 (Figure 5-3.b).

The pixels over the selected average threshold value are successfully pointed out in the experiments, which then utilized to form anomaly matrices regarding with each year. With the score values increasing from blue to red, the chosen pixels are marked with a red circle in Figure 4.b. Furthermore, in order to interpret the rate of change in the anomaly values in time series, common indexed scores are stored in a new variable and plotted against each other. For a better understanding, 2011 image is selected as baseline representing the latest condition of mine site and it is compared with the

anomaly scores in each image within the temporal scale. Four plots exemplifying the relations within the mine life is carefully chosen among the data set for demonstrative purposes (Figure 5). Although the calculated anomaly scores may differ in temporally, it is observed that they tend to show a linear behavior as of the mining operations are ceased in the late 90s. This relation is completely random with the anomaly scores before and during the mining operations. Moving from this point, the coefficient of determination values of each pair of anomaly scores is calculated to quantify the relationship within the time series. These scores also support the tendency of the common anomalies getting a linear trend during the last decade, after the mining activities are finished.

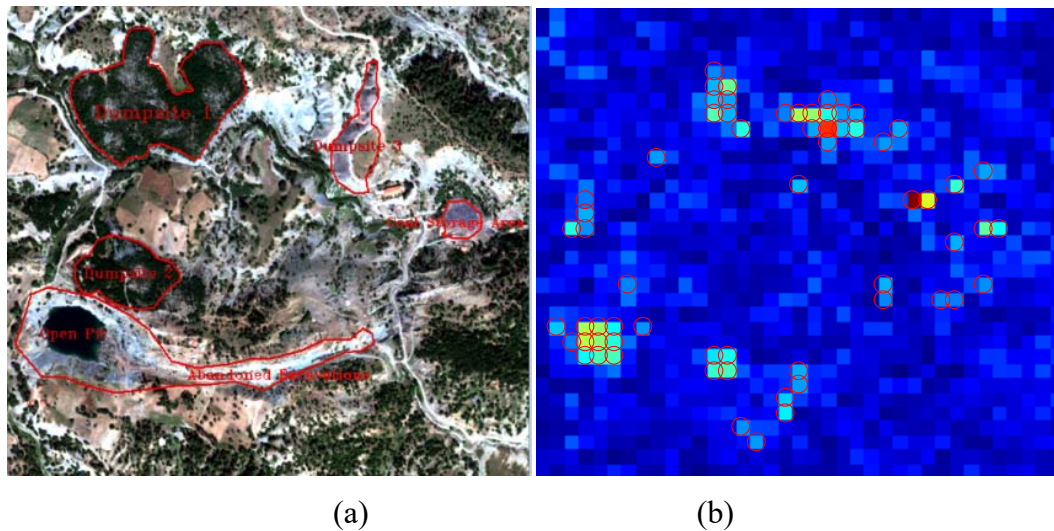


Figure 5-3 a) True Color Image - 2011 b) Global RX Output with high score anomaly pixels- 2011

Furthermore, ROC curves and precision-recall graphs of anomaly output maps across the years are drawn respectively, which can be seen in Figure 5-4. The figure illustrates the performance graphs for the last 6 years (2002-2011) for a better visualization. The success rate incrementally increases along the focused timeline, reaching positive trends only after the mining operations end. The arrow direction points the escalation in the success of the algorithms as the years increase from 2002 to 2011, from light blue to dark.

In evaluating these performance curves, ideally the precision recall graph is expected to get closer to upper right corner, while ROC curve is to upper left. As we investigate the graphs closely, the improvement of the algorithms is prominent in the time series. The latest image, 2011, has the most successful rates in accordance with the both performance evaluators, demonstrating highest lines in both ROC curve and precision recall graphs. The overall increasing tendency in performance rates can vastly be attributed to the land use stability reached after the mining activities were stopped. As the operations going on, the calculated anomaly scores and their locations change on yearly basis as the mine development progress continues, which is also recognized in anomaly score scatter plots of different image pairs.

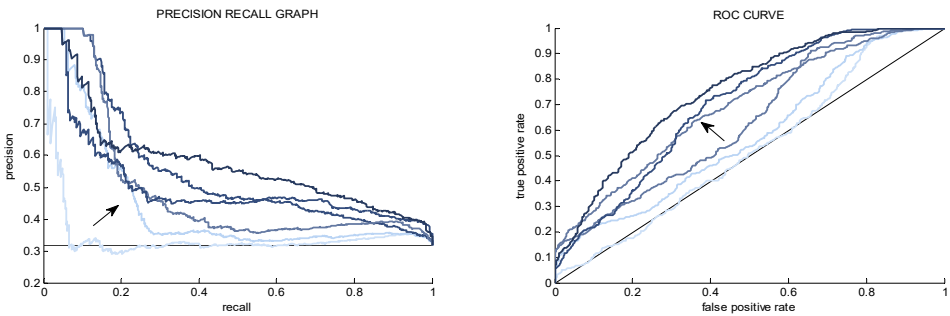


Figure 5-4 ROC Curves of Anomaly Detection Outputs

In the selected subset area focusing on the mine site, the experiments with local RX algorithm unfortunately generate salt and pepper effect in anomaly outputs, with pixels highlighted in almost every applied window size. This is most probably due to the existence of several local maxima points in the input data sets that could not be repressed in 30-meter spatial resolution Landsat 4-5 pixels. In the light of this information, these results are not included as a part of experimental results section.

In order to validate the acquired outputs, a new unsupervised probabilistic algorithm based on calculation of local mutual information over the joint superpixels, obtained by an over-segmentation process, is utilized (Taşkesen et al., 2017). The algorithm is applied on co-registered image sets to produce change maps by making use of mutual information calculation on joint histograms. Despite the low spatial resolution of

Landsat data, the algorithm is able to identify the open pit area, dumpsite, abandoned openings and coal storage unit by assigning higher scores (white pixels, shown in red squares) on the image couple of before (1985) and after (2011) the mining operations.

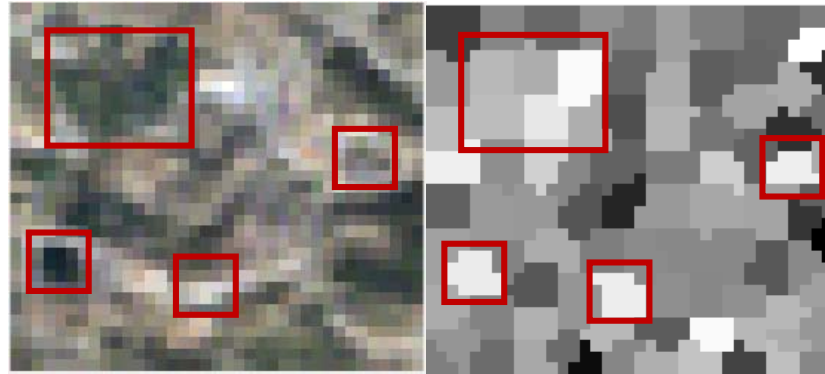


Figure 5-5 Landsat True Color (321) Image and Unsupervised Change Detection Output
(Taşkesen et al., 2017)

To sum up, this study is an attempt to resolve the deviations due to mining activities in an abandoned coal mining area in central Anatolia, demonstrating the changes on earth surface over a time spectrum with the help of newly released Landsat 4-5 Reflectance data provided by USGS, by ruling out the illumination effects for change detection. The conducted experiments reveal especially the profound land use – land cover change in the field in time series, pointing out some critical regions that need an immediate rehabilitation action. Presenting such an invaluable potential to observe the anomalies in a multi-temporal fashion, Landsat reflectance images seem to be resourceful in determining the abnormalities with a great contrast despite its spatial resolution limitations. From the point of mine development process as well as the post-mining monitoring activities, remote sensing analysis provides an opportunity to record the change during the mine life. This potential is even more significant in the case of abandoned mine sites in order to be able to prepare well-grounded reclamation plans.

CHAPTER 6

MAPPING SECONDARY IRON MINERALS FOR DETERMINING ACID MINE DRAINAGE POTENTIAL FOR AN ABANDONED COAL MINE

Sentinel 2 is a multispectral imaging satellite launched by European Space Agency (ESA) in 23 June 2015 for the purpose of supporting Copernicus Land Monitoring studies. It consists of 13 spectral bands, including three different spatial resolution band groups, i.e. four bands – 10 meters, six bands – 20 meters and three bands – 60 meters. It is planned to be complimentary to Landsat and Spot Missions with its coverage and high frequency image acquisition in differing scales. Its application field has already covered spatial planning, monitoring land resources, soil and water as well as observing coastal areas and so on. The availability of high-frequency/high resolution temporal data provides the opportunity to produce land-cover maps, land-change detection maps and monitoring geophysical variables in a determined time sequences (Sentinel 2 User Handbook, 2015).

Among the other products, Sentinel 2A - Level-1C product, which is utilized in the scope of this thesis, is provided as ortho-images in Universal Transverse Mercator (UTM) Projection and World Geodetic System 84 (WGS84) datum. The Level-1C product is delivered with cartographic coordinates, each coordinate referring to upper left corner of the pixel in interest, orthorectified by digital elevation models. The delivered per pixel radiometric measure is Top Of Atmosphere (TOA) reflectance, accompanied with required parameter for reflectance to radiance conversion. As mentioned earlier, Level-1C products comprised of three different ground sampling distances (10, 20 and 60 m) contingent with differing inherent spectral band resolution (Sentinel 2 User Handbook, 2015). Spatial and radiometric resolutions of Sentinel 2A is given below in Table 6.

Table 6-1 Sentinel 2A Spectral Band Properties

Spatial Resolution (m)	Band Number	S2A	
		Central Wavelength	Bandwidth
10	2	496.6	98
	3	560	45
	4	664.5	38
	8	835.1	145
	5	703.9	19
	6	740.2	18
20	7	782.5	28
	8a	864.8	33
	11	1613.7	143
	12	2202.4	242
	1	443.9	27
60	9	945	26
	10	1373.5	75

Multispectral images and hyperspectral images are both capable of mapping specific absorption features in the spectrum, depending on the spectral resolution, the location of the multispectral bands in question and the bandwidth of the absorption characteristics. This capability leads researchers to focus on new methodologies to map diagnostic mineral absorption features as well as identification of minerals utilizing band ratios, producing new indexes. Sentinel 2 spectral band are designed to covering narrower widths in order to avoid the contamination due to atmospheric effects, most importantly water vapor. In addition, the band 8a, having a 33 nm width, is specifically designed to detect the iron oxide contents, whose diagnostic absorption is a reflectance minimum congruent with this band, around 900 nm (Sentinel 2 User Handbook, 2015).

According to Murphy et al. (2014), iron-bearing minerals exhibit diagnostic absorption features around 900 nm due to crystal field or electronic absorption characteristics of ferric ions. The electrical processes of transition metals (i.e., Fe, Cu, Co, and Cr), which actually demonstrates the energy state of orbital electrons, induces the observable absorption characteristics in the region of 0.4 μm to 1.3 μm (i.e. electronic

region). On the other hand, OH-, H₂O, NH₄⁺, SO₄⁻ ions are responsible for the absorption features in the vibrational region, which is between 1.3-2 μm in the electromagnetic spectrum (Hunt, 1977; Swayze et al., 2000).

Hunt (1977) explains further that the most frequently exhibited features in the visible and near-infrared (VNIR) region spectra of minerals, rocks and soils are indicators of iron in different forms. As common in all transition elements, the energy levels of an ion located in a solid changes depending on its interaction with the surrounding crystal field. Here, the valence state of the ion (Fe²⁺ or Fe³⁺), coordination number and the occupied symmetry of the site determines the position of the aforementioned energy levels (Hunt, 1977). Stoner et al. (1979) also specify the existence of broad bands at 0.7 and 0.9 μm due to high concentrations of ferric iron existence, with an additional remark about a comparative decrease in content as the bandwidth gets sharper.

Mielke et al. (2004) state that the most common secondary iron minerals, which are also associated with mine wastes and acid mine generation (i.e. goethite, hematite and jarosite) have also a minimum reflectance absorption around 900 nm, which is explained in detail by Clark, 1999. The ubiquitous nature of iron oxides, hydroxides and sulfides make them special for researchers as well as their special characteristics in VNIR region. As can be seen in Figure 6-1, larger grain sizes exhibit broader reflections together with a shift to longer wavelengths and saturation. The 900 nm absorption feature is emphasized as a common property as to iron bearing minerals, which is due to similar electronic absorption features in the visible and near-infrared.

Spectral signature examples secondary iron minerals are given in Figure 6-2, showing the absorption feature at 900 nm. Although hematite seems to have a sharper absorption feature compared to others, particle size distribution might influence this differentiation. Ferrihydrite is also an iron oxide, with similar overall characteristics to Orange precipitate in the reflectance spectrum, before continuum removal or scaling.

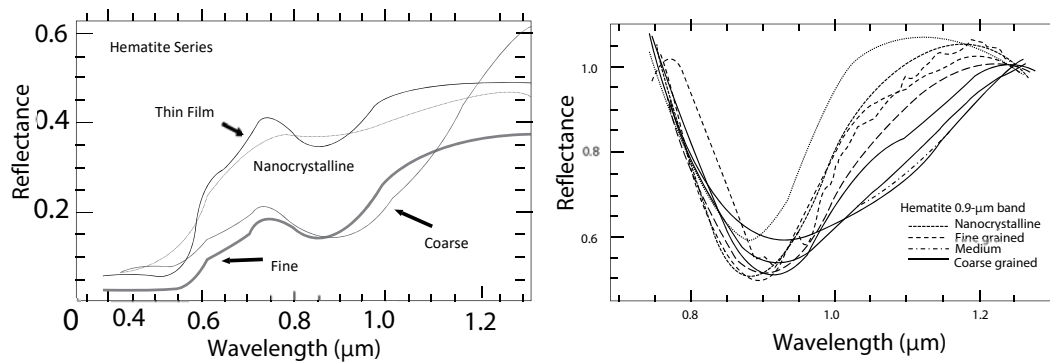


Figure 6-1 Hematite Spectra and 900 nm Absorption Feature for Different Grain Sizes (Clark, 1999)

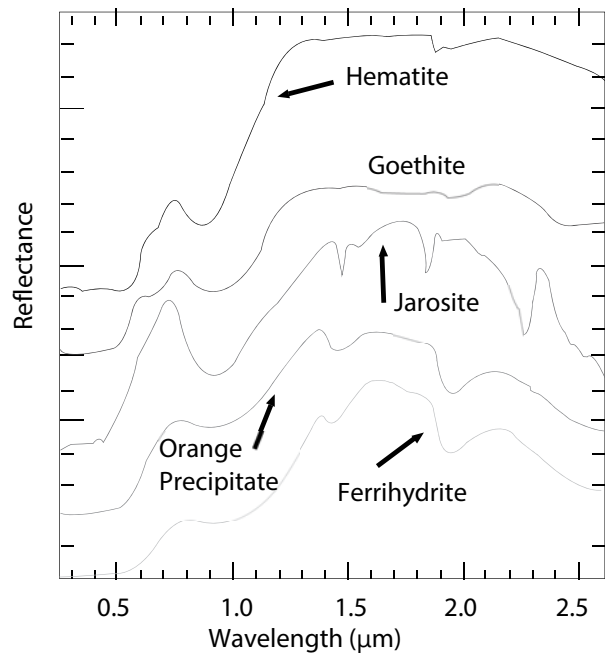
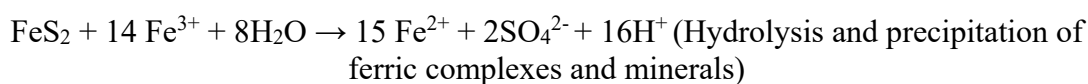


Figure 6-2 Spectral Fingerprints of Secondary Iron Minerals (Clark, 1999)

In addition, Figure 6-2 also illustrates the jarosite, an iron sulfate, having a narrow absorption near 0.43 μm , with another diagnostic absorption feature at 2.27 μm because of a mixing effect of OH stretch and Fe-OH bend.

Coal mining operations are regarded as one of the most significant sources of acid mine drainage (AMD) or acid rock drainage (ARD) among the other mining activities,

due to the inherent iron sulfate contents. According to the conducted studies by Rose et al. (2013), the sulfuric acid generation caused by sulfide mineral oxidations (more commonly pyrite) together with iron sulfates is regarded as the main reason for the toxic drainage in the mining area. The oxidation reactions are triggered in the existence of water and oxygen to generate acidic drainage, which are then transported depending on the topographical conditions. The primary sources of AMD are mentioned as mine rock dumps, mine tailings, open pit and underground mining areas and drains originating from overburden piles even in rehabilitated areas (Akçıl ve Koldaş, 2005). It's also important to note that the aforementioned reactions are facilitated and accelerated by bacteria present in the environment, affecting the rate of acidic drainage generation drastically. According to Dold (2010), pyrite oxidation takes place in certain stages, which is also effective for secondary iron minerals' formation, determined by the geochemical conditions of the environment. This sequence occurs with the metastable secondary products ferrihydrite, and goethite, followed by more stable secondary jarosite, and hematite depending on the geochemical conditions (Bigham et al., 1996). The chemical equations take place in the following order:



After the oxidation of the sulfide minerals in the first stage, the ferrous ions are oxidized to produce ferric ions, which actually will be primary oxidant of pyrite in the third stage. These reactions are accelerated in acidic environment, especially with the pH values lower than 3 (Dold, 2010). Furthermore, the metal ions in the system also hydrolyzed in the surrounding acidic environment, because the water molecules start to act as proton acceptors. Espana et al. (2005), also emphasizes the presence of iron and aluminum bearing minerals such as schwertmannite, jarosite, ferrihydrite, goethite, hematite, basaluminite, jurbanite, gibbsite in the acid mine drainage systems,

as indications of the growth kinetics of hematite and goethite that are much smaller than schwertmannite, ferrihydrite and jarosite.

6.1 Utilized Data and Methodology

The objective of this study is to develop a new methodology to produce Fe-bearing mineral indicator maps to determine potential acid mine producing regions in an abandoned coal mining area, with the help of Sentinel 2 imagery. Among the mentioned secondary iron minerals (i.e. goethite, jarosite, ferrihydrite, hematite etc.), hematite is selected as the mineral indicator to be focused as it's the only one revealed during laboratory testing. It is obvious that mapping pyrite minerals would be much more direct, but considering its lack of distinctive spectral fingerprints hampered by secondary mineral coatings, the direct detection with spectral techniques is not possible. The distinguishing characteristics of iron oxides, hydroxides or sulfates make them favorable for spectral detection that can be used as indicators for tracing acid mine drainage sources.

In this research hyperspectral unmixing algorithms are performed to produce secondary iron mineral (hematite) indicator maps which is detected in the soil samples collected from the study area. It's important to note that these samples are not collected from the sources of AMD or river beds, as they were collected for investigating chemical and physical properties of the soil in the same mining area, for a previous study (Soydan, 2013). Nevertheless, detection of hematite still provides sufficient evidence for a possible risk or existence of AMD in the mining field.

The methodology consists of two major steps:

- i- Investigating the applicability of 900 nm absorption feature by validation both with the hematite signature acquired from USGS Spectral Library and collected ASD Spectral Signatures.

ii- Application of two geometric unmixing algorithms to Sentinel-2 Image

The details of the followed procedure which is also demonstrated in Figure 6-3, is listed below in two main stages (1-6) and (7-10). In the first stage (1-6), the steps for parabola fitting are given, and the second stage consists of the steps of application of unmixing algorithm.

1. Sentinel-2 Images are downloaded through *glovis.usgs.gov*
2. The data is resampled to three different spatial resolutions, which are 5, 30 and 60 meters.
3. The first nine VNIR bands are stacked for the further analysis on the data cube.
4. The hematite signature is downloaded from USGS Spectral library. The absorption feature around 900 nm is remodeled given the methodology in van der Werff and van der Meer (2015).
5. The spectral samples collected from the field are also examined for the absorption parameter and the fit of the suggested model by van der Werff and van der Meer (2015).
6. The fitted model is revised iteratively according to the previous steps.
7. The unmixing algorithms, SISAL and MVSA are applied on the satellite data.
8. The resulting nine endmembers are investigated for the diagnostic absorption band of hematite, which corresponds to the spectral region 750 – 950 nm region, with Spectral Angle Mapping (SAM) Algorithm.
9. The abundance maps are produced for the output endmembers with an additional vegetation mask application step, as in van der Werff and van der Meer (2015) to be on the safe side.
10. The abundance map corresponding to the minimum SAM error in the absorption region is designated as the target map.

The selection of SISAL and MVSA ((Li & Bioucas-Dias, 2008; Bioucas-Dias, 2009) is due to their comparative success to other unmixing and signature based methods for hydrocarbon induced alteration detection in Chapter 4.

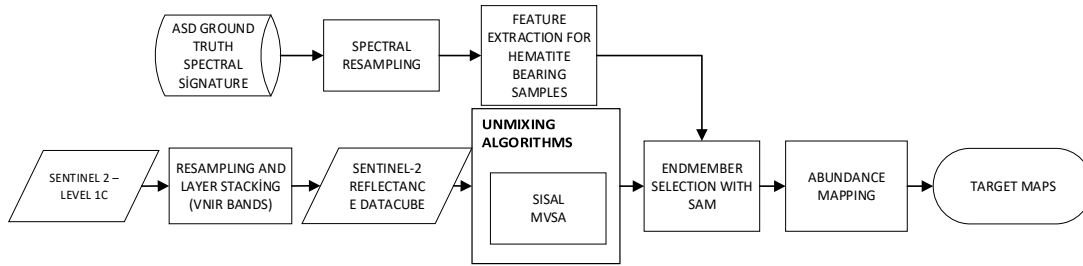


Figure 6-3 Flowchart of the Methodology

6.1.1 Validation with ASD Library Spectra and Laboratory Analysis

Band 8a of Sentinel-2 image is specifically designed to capture the iron bearing secondary mineral absorption feature with its narrow bandwidth and band center located at 865 nm. The proposed model is mainly working as the band ratio images, making use of the prior and latter bands around the absorption feature, but providing a continuum along the defined wavelength interval as in hyperspectral sensing.

The validation is performed by both using USGS Hematite spectra and ASD spectra collected from the region by following the model proposed by van der Werff and van der Meer (2015). In their study, the authors propose to fit a second-degree polynomial for identifying the minimum of the spectrum as well as its depth. The convexity of the fitted parabola proves the existence of the absorption and produces the minimum wavelength/feature depth parameters for a synthetic Sentinel-2 image of The Cabo de Gata volcanic field, covering a region of metamorphic minerals such as kaolinite, alunite or iron rich montmorillonites.

In order to determine the absorption feature, the authors applies the parabola fitting technique to calculate the minimum iron absorption feature using the following equations:

$$w_x = ax^2 + bx + c, w_{\min} = -\frac{b}{2a}$$

where

w_x is interpolated reflectance value at position x

x is wavelength position in nm;

a and b are coefficients of the parabola function, and

w_{min} is the interpolated wavelength position at minimum reflectance.

The USGS validation is replicated by utilizing the same set of secondary iron bearing minerals, which are reported to be associated with acid mine drainage in mine sites. As mentioned earlier, the results of hematite is given for convenience, considering the XRD laboratory experiment results. For the purposes of the study, the location of minimum absorption feature is regarded adequate and effective.

Figure 6-4, gives the USGS hematite spectra resampled to Sentinel-2 spectral resolution with the fitted parabola:

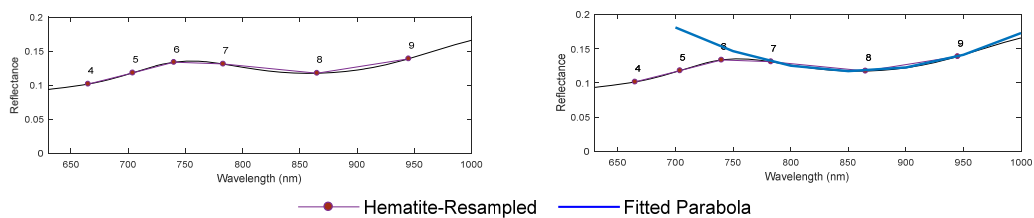


Figure 6-4 Hematite Spectral Signature with Fitted Model

Hematite
Min.Wavelength
835.92

As explained in Stoner et al. (1979) the existence of broad bands reaching from 0.7 to 0.9 μm also points out the high content ferric iron. As the absorption feature gets narrower, the relative concentration is decreased. Considering that the focus of the study is an abandoned cola mining area rather than a metal mine or mine tailing, the absorption band is expected to be relatively narrow in reference to pure hematite spectral fingerprint. For this reason, the validation operation is implemented on the spectra of soil samples collected from the abandoned mine field.

Figure 6-5 illustrates ASD Spectra of Soil Samples on which XRD Analysis Performed on six soil samples. Table 6-2 demonstrates the results of the XRD analysis on these samples. The iron absorption feature is distinguished even visually in the four samples for which XRD analysis proved the presence of hematite. The absorption characteristics of the iron bearing samples are utilized to adjust the parabola model to Band 7, Band 8a and Band 9 for optimized fitting. As in the study of van der Werff and van der Meer (2015), the minimum wavelengths are observed between 800 – 900 nm intervals for the hematite bearing spectra, while the other two samples exhibit a straight line rather than a parabola, which confirms the lack of the mineral. The difference in the optimized bands with regard to van der Werff and van der Meer (2015)’s study is attributed to the fact that the content of iron bearing minerals in the study area is comparatively far less than pure mineral spectra or a metal mine.

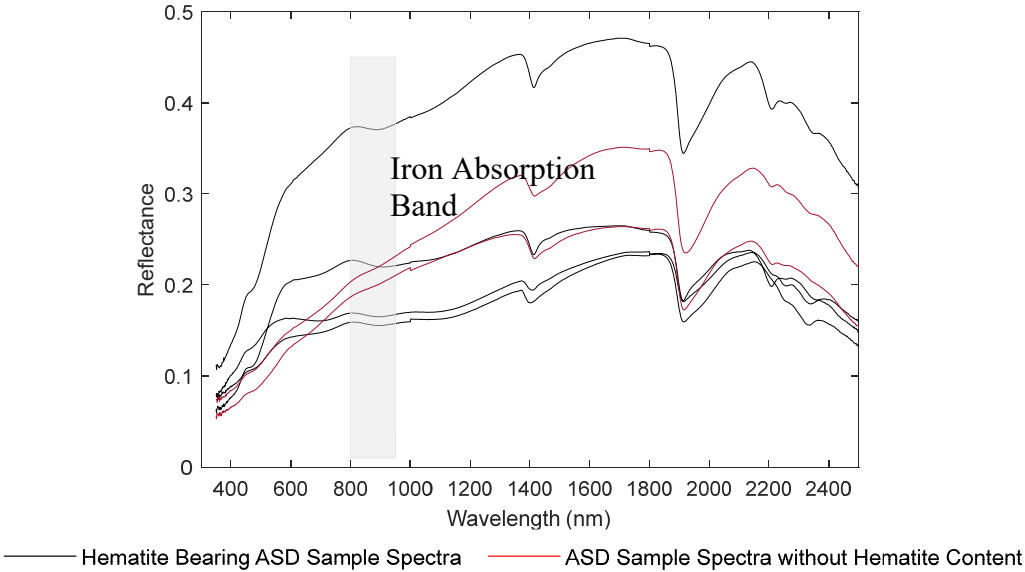
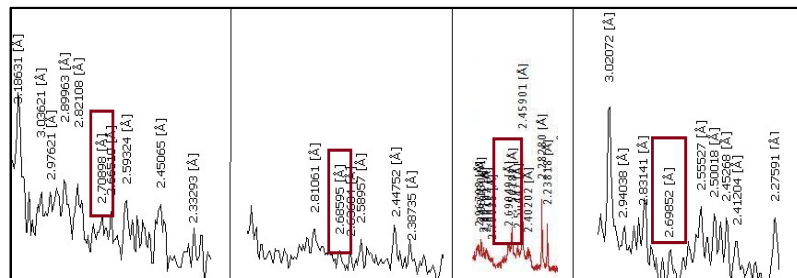


Figure 6-5 ASD Spectra of Soil Samples on which XRD Analysis Performed

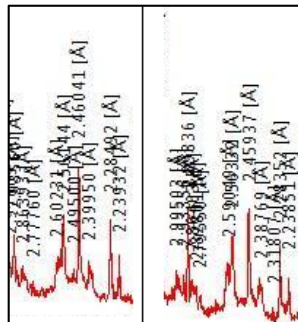
Table 6-2 XRD Laboratory Experiment Results

XRD Mineral Laboratory Experiment Results	
Sample 5	Smectite, Chlorite, Feldspar, Serpentine, Quartz, Hematite
Sample 7	Smectite, Chlorite, Illite, Quartz, Amphibole, Hematite
Sample 10	Chlorite, Quartz, Mica (Illite), Feldspar, Serpentine, Hematite
Sample 18	Chlorite, Quartz, Feldspar, Serpentine, Mica, Calcite
Sample 23	Chlorite, Quartz, Feldspar, Mica, Dolomite
Sample 31	Chlorite, Mica(Illite), Smectite, Calcite, Feldspar, Hematite

In Figure 6-6 and Figure 6-7 below, the XRD laboratory analysis outputs and the models with parabola fitting are given. According to the experimental results, the hematite mineral is proven to be differentiated taking the 700-900 nm iron absorption band in consideration. Given the validation of the model, compiled with both spectrally resampled library spectra and ASD spectra, the potential of Sentinel-2 images to map secondary iron minerals are confirmed in the context of identifying potential acid mine drainage localities in the abandoned coal mine site.



a) Samples with secondary iron minerals (Hematite)



b) Samples without secondary iron minerals

Figure 6-6 XRD Results of Soil Samples

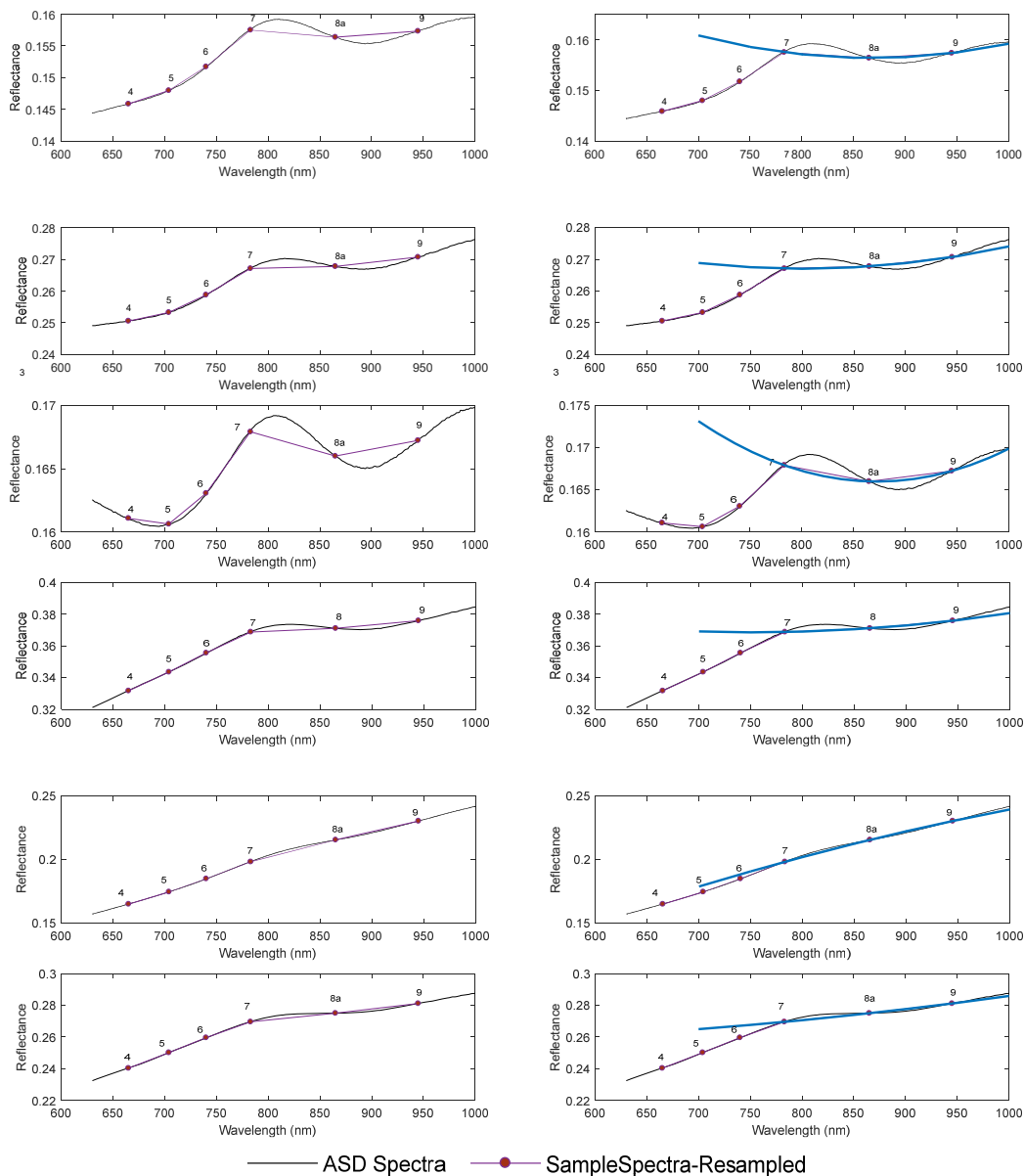


Figure 6-7 The Parabola Model Fitted to ASD Spectral Samples of Soils

The fact that resampled spectral samples exhibit the iron absorption characteristics in VNIR region encourages advanced applications for feature mapping using Sentinel-2 satellite images. Accordingly, Sentinel-2 image of the mine area, which is publicly available via glovis.usgs.gov is downloaded for further analysis. In the next section, the experimental results will be elaborated by following the two major stages of methodology, which are validation of USGS hematite signature and spectra of

collected samples, and creating abundance maps by means of unmixing algorithms. The details for each major stage is listed in Section 6.1.

6.2 Experimental Results of Implementation of Unmixing Algorithms

The aim of implementing the unmixing algorithms is to attempt to extract the spectral endmember, which has the iron absorption feature. This endmember is then utilized for abundance mapping that corresponds to hematite bearing locations.

The downloaded Sentinel-2 image is resampled to three different spatial resolutions, in compliance with its inherent bands before inputting to unmixing algorithms. With this operation, it is aimed to observe the effect of varying ground sampling distances on produced maps. As described earlier in Section 6.1, the acquired endmembers are investigated for the iron absorption feature in VNIR region by utilizing Spectral Angle Mapping (SAM) algorithm. The abundance map corresponding to endmember, which has the minimum error, is selected as the secondary iron mineral bearing (hematite) target map.

According to the resulting error terms, Sisal algorithms consistently performs better as shown in Table 6-3, for each resolution in comparison with MVSA technique as shown in Table 6-4. It's evident from the both algorithm results that minimum error is achieved for the endmember acquired from the 5 meter resolution data set. Although an incremental escalation in error terms is observed for MVSA outputs as the spatial resolution increases, for SISAL outputs this consistency is lacked. However, in overall assessments, with error terms lower than 0.1, SISAL results in better outputs, exhibiting the high similarity in the tendency of the reference spectrum and extracted endmembers. This relative superior performance of SISAL to MVSA can be due to is the replacement of positivity constraint with “hinge type” soft constraints.

Having decided which endmember resulted in high similarity with reference spectrum, the parabola fitting technique is additionally performed on each endmember, just to determine the compatibility of minimum wavelength of the simulated model with the USGS hematite signature.

Table 6-3 Spectral Angle Errors [Extracted Endmembers (SISAL) and USGS Hematite Spectra]

SAM Errors	SISAL ENDMEMBERS								
	1	2	3	4	5	6	7	8	9
Sentinel-5m	0.455	2.759	2.441	0.493	0.388	0.056*	0.383	0.482	0.428
Setinel-30m	0.323	0.503	0.405	0.075*	2.879	0.463	0.435	0.433	2.352
Sentinel-60m	2.672	0.450	0.462	0.428	0.489	0.450	0.132	0.060*	0.442

Table 6-4 Spectral Angle Errors [Extracted Endmembers (MVSA) and USGS Hematite Spectra]

SAM Errors	MVSA ENDMEMBERS								
	1	2	3	4	5	6	7	8	9
Sentinel-5m	0.422	0.426	0.536	2.853	0.370	0.390	0.105*	0.452	2.386
Setinel-30m	0.483	0.395	0.185*	0.407	0.397	0.444	2.964	0.575	2.404
Sentinel-60m	0.508	0.234*	2.791	0.440	1.146	0.538	0.438	0.332	1.605

Unfortunately, unmixing algorithms applied on the Sentinel-2 multispectral data cube are not able to resolve overall spectrum completely. However, these algorithms consistently demonstrated the ability to capture the spectral variation between 660 – 945 nm in one of the endmembers, which is related to secondary iron bearing minerals. Besides, calculated minimum wavelength positions are located between 800- 900 nm as one would expect to be consistent with the model parameter descriptions by van der Werff and van der Meer (2015), as well as the replicated output with the method in consideration. This analysis resulted in 835.92 nm as the minimum wavelength for USGS hematite mineral spectra. Figure 6-8 illustrates the extracted endmembers for each spatial resolution for SISAL and MVSA algorithms in the first column and iron absorption band related interval in the second (right) column. This portion demonstrated in the second column in Figure 6-8 is then used in Figure 6-9 to show parabola fitting for capturing absorption feature due to iron content for each endmember.

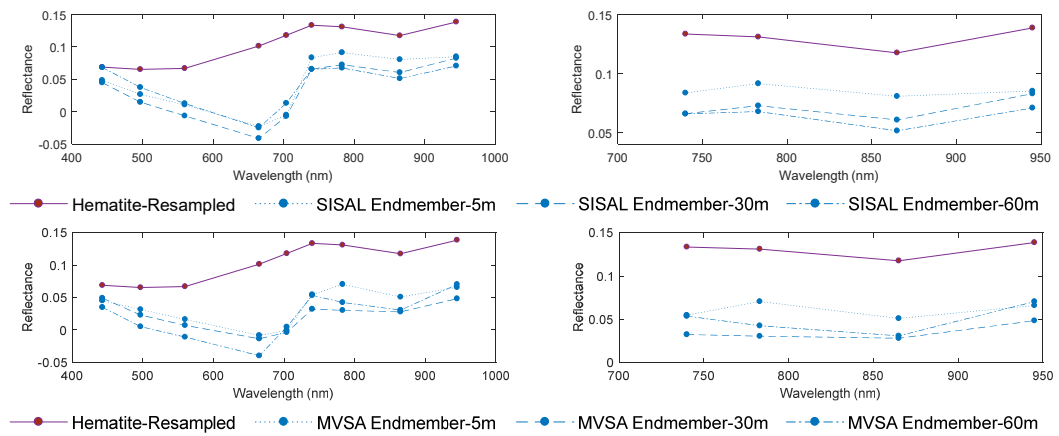


Figure 6-8 Hematite spectra resampled to Sentinel-2 resolution with the endmembers with minimum errors (Left column: Overall spectrum, Right column: Iron absorption bands, 745-945 nm)

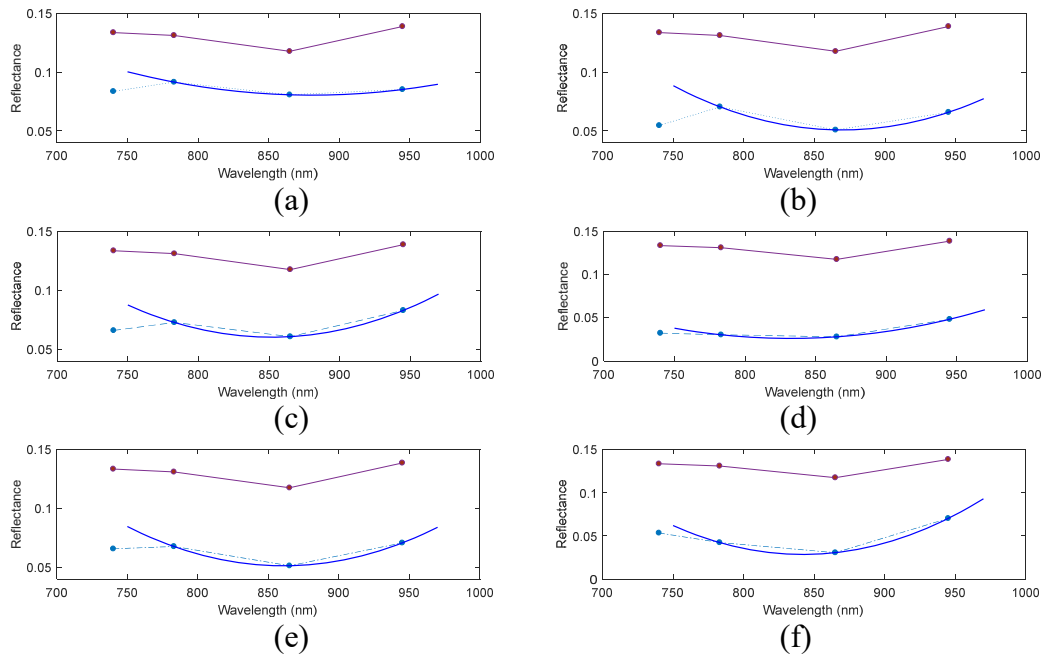


Figure 6-9 Parabola fitting techniques for capturing absorption feature due to iron content for each endmember Left Column: Sisal Endmembers, Right Column: Mvsa Endmembers a) 5-m b) 30-m c) 60-m

Table 6-5 Minimum Wavelengths For Extracted Endmembers

ENDMEMBERS	SISAL	MVSA
	Min.Wavelength	Min.Wavelength
Sentinel-5m	880.74	869.42
Setinel-30m	851.21	832.34
Sentinel-60m	860.53	842.17

The abundance mapping for the selected endmembers is performed with fully constrained least squares on pixels, which takes non-negativity and sum to one constraints into consideration (A representative sample illustrating all abundance maps of SISAL-30 meter outputs, without NDVI application, is given in Appendix B). That is, each pixel's assigned abundance value should be positive and added to a total value one. The abundance maps are produced for both methods and each resolution one by one with an attempt to investigate the compatibility between the algorithm outputs. Another motivation is, again, to understand the spatial resolution effect on the generated outputs, how they relate to each other and pattern consistency keeping the mine layout in mind.

Focusing on the complications due to vegetation mentioned in van der Werff and van der Meer (2015) and the impurities it might cause in pixels, Normalized Difference Vegetation Index (NDVI) mask is applied to exclude any effect on produced target abundance map considering the incapability of the unmixing algorithms to resolve overall spectrum. The vegetation index is defined as follows: the pixels having and index between 0 – 0.3 is preserved in the target maps as suggested in van der Werff and van der Meer (2015).

$$NDVI = \frac{NIR - VIR}{NIR + VNIR} ; NDVI = \frac{Band\ 8 - Band\ 4}{Band\ 8 + Band\ 4}$$

It's important to note that the dump sites which were afforested during an unfinished rehabilitation activity had to be excluded due to high vegetation indices, although their assigned pixel values are at the higher upper quantile of the histogram. The estimated content is distributed between 0 – 0.1 for the maps of 5-meter resolution, 0 – 0.07 for

the maps of 30-meter resolution and 0 – 0.15 for the maps of 60-meter resolution for both algorithms. The resulting maps for 5-meter and 30 meter ground sampling distance show high compatibility, demonstrating a linear behavior with each other. However, the outputs for 60-meter resolution doesn't show this correlation. In addition, the visual assessments prove that the pixels of higher content show a high compatibility with each other as well.

The results indicate the variation of pixel contents are also matching with each other, especially for the higher spatial resolutions. That's why, they are regarded as more trustworthy than the 60-m outputs. Furthermore, given the calculated minimum absorption location of each extracted endmember, 30-m outputs seem to be closer to the hematite reference spectra's compiled minimum wavelength, which makes them a better approximation for the calculated iron contents. Figure 6-13 illustrates the examined algorithm outputs, content increasing from blue to red together with the total iron amounts of soil samples collected from the region. The laboratory measurements of the soil samples for heavy metals are conducted with Inductive Coupled Plasma (ICP) analysis. In addition iron content, several heavy metals (i.e. copper, manganese, zinc, lead, nickel chromium, arsenic and molybdenum) are also measured to calculate the enrichment ratios regarding these trace elements.

The mine layout consists of three dumpsites, open pit and abandoned excavations and coal storage area, which is shown in Figure 6-10. The main streams passing through the mining area are also shown in the mine layout, following a path from west to east. Within the perspective of this research, the total iron amounts are also illustrated with graduated symbols. According to the measured contents, it's obvious that the iron amount is higher in the samples collected around the units of mine layout, while it is quite low in the samples outside of it. The increase in content along the accumulated main stream should also be noted.

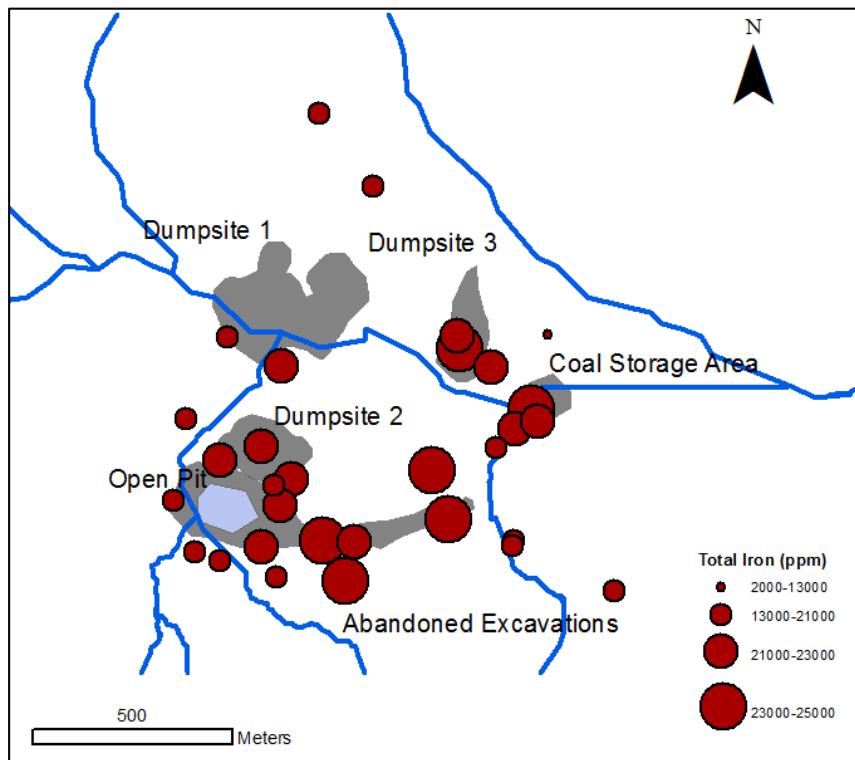


Figure 6-10 Mine layout with total iron content

As mentioned earlier, in addition to iron content, ICP analysis is conducted to measure some trace metals as well. For evaluating their current levels and contamination potential, the measured minimum values for each of them are regarded as background. After calculating the mean values, the enrichment ratio is calculated by simply dividing it to minimum (background). The results indicate the significant deviation of average iron amounts from the minimum, which is followed by the lead levels. The copper, manganese, nickel, chromium and arsenic have twice as much the measured minimum amount as well. In Appendix C, the detailed information of each sample is given in detail. In Figure 6-11, the calculated enrichment factors are illustrated.

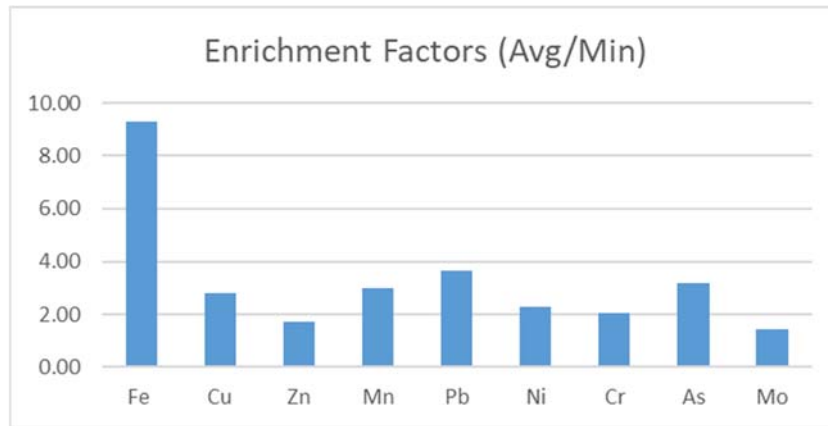


Figure 6-11 Enrichment factors of measured heavy metals

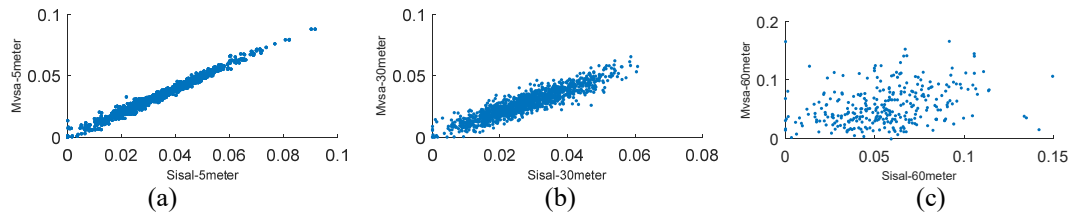


Figure 6-12 Unmixing algorithm output plots (a) 5-m (b) 30-m(c) 60-m

Figure 6-13 illustrates the algorithm outputs with the prepared mine layout. The pixels with red (darker) color shows the high hematite content. In line with the measured iron levels, relatively higher amounts of hematite is observed at the lower edges of dumpsites and coal storage area along with the main streams. Both unmixing method gives out compatible result for differing spatial resolutions that declines as the spatial resolution decreases (Figure 6-12).

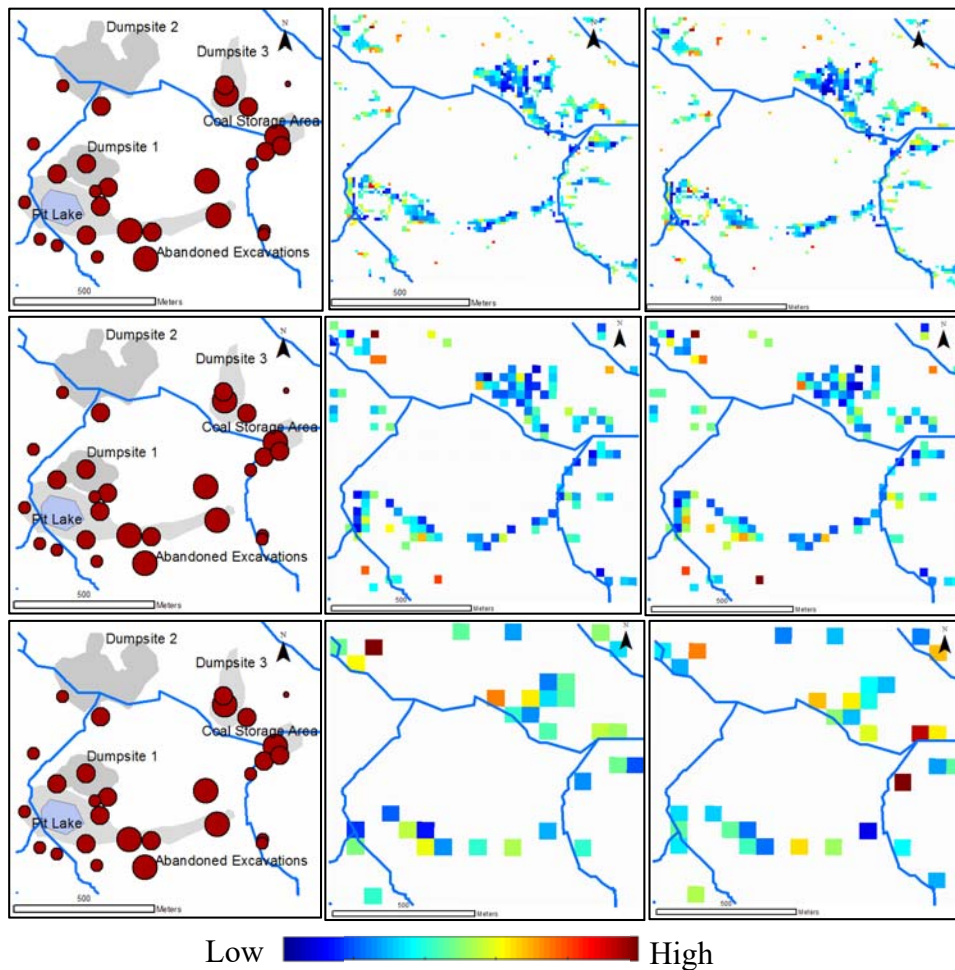


Figure 6-13 Abundance Maps Representing the Iron Bearing Spectral Endmember (First Row: 5-m, Second Row: 30-m, Third Row: 60-m)

In this section, a new methodology for mapping secondary iron minerals is proposed with Sentinel-2 image. During the validation procedure, both XRD laboratory analysis and the parabola fitting technique by van der Werff and van der Meer (2015) are performed for determining the minerals associated for mine waste monitoring, inspired by Mielke et al., 2014 and van der Werff and van der Meer (2015). Conducted laboratory experiments prove the presence of hematite in the collected soil samples, which makes hematite mineral of a target interest. The hematite signature downloaded from the USGS is utilized as the spectral fingerprint to replicate the parabola fitting algorithm proposed by van der Werff and van der Meer (2015), which then further applied to the spectral samples of collected soil samples. After the validation process,

the spectral unmixing algorithms are applied to the Sentinel-2 images of differing ground sampling distances, in order to select the endmember exhibiting the same spectral absorption feature around 900 nm with hematite. Spectral angle mapping algorithm is compiled to measure the trend of the characteristic absorption feature for each endmember and reference spectrum, to select the one with minimum error. The resulting endmember with minimum error metrics is utilized to produce the corresponding hematite abundance maps. Considering any effect due to vegetation affecting the success of the algorithms, an NDVI mask is also applied for being on the safe side on the generated outcomes. The methodology, applied to Sentinel-2 VNIR 5m – 30m and 60 m data cubes, reveals hematite compatible contents for the applied unmixing techniques of SISAL and MVSA. Both techniques perform better for the images of 5-m and 30-m spatial resolution with a higher compatibility.

To conclude, Sentinel-2 imagery proves its capability not only for mapping iron related parameters, but also its potential for generating iron content maps, which is highly significant for mine monitoring activities. Hyperspectral unmixing algorithms are found to be successful to extract the endmember exhibiting the well-known iron absorption parameter around 900 nm during the experiments with the multispectral Sentinel -2 imagery. The high revisit time of the satellite, its availability together with its optimized band for capturing the iron absorption stand as an invaluable source for future research.

CHAPTER 7

CONCLUSION AND RECOMMENDATIONS

7.1 Conclusions

In this thesis, hyperspectral anomaly detection and target detection algorithms for contamination mapping, with a driving force on developing a new methodology for environmental problems related to coal mining operations is investigated. Considering the data limitations and the resemblance of chemical structures of hydrocarbons and carbon bearing materials, the algorithm performances are tested and optimized for detecting oil spills and hydrocarbon induced surface alterations. In the view of the developed methodologies and their ability to discriminate hydrocarbon induced abnormalities both in water and soil media, the global anomaly detection algorithm's performance for designating topographical changes in the landscape is examined in a temporal manner. In order to understand whether the utilized techniques have the ability to reveal the secondary iron minerals inducing the existing acid mine drainage problems in the study area, unmixing algorithms are applied to a new satellite image, Sentinel-2, which points out the hematite minerals in the mine site. Accordingly, the unmixing outputs are compared with each other to disclose their compatibility with each other by means of the multispectral Sentinel-2 image of different ground sampling distances.

Following key conclusions can be drawn from this study:

- For oil spill detection on water surface, anomaly detection methods are able to highlight the target pixels without removing the noise components, except for Gaussian-RX (GRX) algorithm. However, it has the disadvantage of high computational times and not properly catching the right contrast for the target abundance at every time. A fine-tuning, such as the size of the kernel window

and distribution variation parameter, is required to be optimized for proper visualization with Gaussian RX algorithm.

- Signature based methods, on the other hand, eliminates all noises providing a good contrast to highlight the quantity of oil slicks for both hyperspectral images. In the algorithm outputs, the change in the abundance of the oily regions is well observed. It is also concluded that among the signature based target detection methods, Desired Target Detection Algorithm (DTDCA) performs better than the Spectral Match Filter (SMF) method in both locating the oil spill regions and showing its abundance with a good contrast. This outcome is reasoned with the removal of the undesirable signals prior to matching operation in DTDCA.
- Unmixing algorithms applied for determining hydrocarbon-induced alterations on ASTER image reveals its effectiveness to delineate surface alterations in the study area. With their capacity to extract the representative endmembers, unmixing algorithms present the ability for ground truth comparisons with the reference spectra collected from the field as well as validation.
- Among the four different algorithms applied for hydrocarbon alteration mapping, SISAL and MVSA outperforms pure-pixel based N-FINDR and VCA algorithm due to the low spectral/spatial resolution of ASTER data set. Despite suppressing out the background pixels, pure pixel based methods are able to point out the microseepage pathway along the syncline path. This is due their assumption that there is at least one pure pixel representing each endmember in the image.
- The calculated error metrics is of a paramount value to make overall assessments about in-group and between group performances. This metric discloses the high performance of DTDCA algorithm in comparison to other

signature based and traditional methods, even better than pure-pixel based algorithms.

- The Global RX algorithm applied on Landsat reflectance images on the abandoned coal mining area demonstrates its capacity to produce change maps, putting forward the major mine layout components such as the open-pit, coal storage area, excavations & area of disturbances of the land as well as the dumpsites throughout multi-temporal images. In spite of the variations of high score pixels across the temporal scale, it can be interpreted via ROC curves that they tend to stabilize after the end of active mining activities. From the perspective of mine development process as well as the post-mining monitoring activities, the analysis provides an opportunity to record the change during the mine life, by ruling out the illumination factors of the acquired images. This potential is even more significant in the case of abandoned mine sites in order to be able to prepare well-grounded reclamation plans.
- The methodology proposed by making use of Sentinel-2 image for mapping secondary iron minerals (which are related to acid mine drainage problems in mining sites) establishes the capacity of unmixing algorithms to differentiate the iron absorption feature among the extracted endmembers. The ability of the methodology for not only mapping iron related parameters, but also generating iron content maps is regarded as highly critical for mine monitoring activities. In addition to its specific band for capturing iron absorption feature, the frequent data acquisition and public availability makes Sentinel – 2 data appealing for upcoming researches.
- In evaluating the masked abundance map, which corresponds to iron bearing endmember, total iron contents measured in laboratory environment with ICP analysis are mapped in graduated symbols. After the geo-registration process, the compatibility between the high content pixels of Sentinel – 2 abundance maps and the total iron levels is observed. In addition, it is important to note

that higher iron amounts are observed within the mine layout, which is simply proved by the calculated enrichment factors.

- Keeping in mind the prediction and validation issues in geo-information analysis, this study contributes to literature by setting a benchmark in a time and cost effective fashion, minimizing the labor-intensive field works.

7.2 Recommendations

Although the dissertation makes a significant contribution to the literature to comprehend the detection techniques by means of integrating hyperspectral and multispectral image analysis, several improvements can be made by the following:

- By making use of the publicly available Sentinel – 2 data, a new project adapting the proposed methodology for mapping iron bearing minerals can be implemented over the lignite mines with acid mine drainage problem (referred in Ministry of Environmental Affairs report).
- Considering the major data availability obstacle for this study, and lack of budgets, a hyperspectral scene of the focused mine area could not be acquired. If possible, it is recommended to obtain a hyperspectral image to analyze the algorithm performances. The laboratory measurements conducted within this thesis are of a significant resource if such a goal is pursued.
- Depending on a regular access to a spectrometer, analytical observations of the contaminant agent in interest in a controlled environment is strongly suggested. With the existence of both reference spectra and hyperspectral images, a proper approach for separating the contaminant’s fingerprint would be more efficient and successful.

- As more practical and efficient means for contamination mapping, using portable spectrometers to gather information from the area of interest provides significant evidence for detecting hot spots that requires further investigation.
- By setting benchmarks with the collected spectral data, a more practical and time efficient monitoring can be implemented for both oil spill and acid mine drainage sites, that might be an aid for preventing propagation of existing contamination agents.

REFERENCES

- Alam, M. S., & Sidike, P.(2012). Trends in oil spill detection via hyperspectral imaging. 7th International Conference on Electrical and Computer Engineering, Dhaka, 2012, pp. 858-862.doi: 10.1109/ICECE.2012.6471686
- Akçıl, A., & Koldaş, S. (2006). Acid mine drainage (AMD): causes, treatment and case studies. *Journal Of Cleaner Production*, 14(12-13), 1139-1145. <http://dx.doi.org/10.1016/j.jclepro.2004.09.006>
- Alpers, C. N., Blowes, D. W., Nordstrom, D. K., Jambor, J. L. 1994. Secondary minerals and acid-mine water chemistry. In *Short Course Handbook on Environmental Geochemistry of Sulfide Mine Wastes*, Waterloo, Ontario, May 1994. Mineralogical Association of Canada. p. 247-270.
- Andreoli G., Bulgarelli B., Hosgood B., Tarchi D. (2007). Hyperspectral Analysis of Oil and Oil-Impacted Soils for Remote Sensing Purposes. Retrieved from <http://publications.jrc.ec.europa.eu/repository/handle/JRC36875>
- Atzberger, C. (2002). Soil optical properties – A review. University of Trier, Remote Sensing Department, Tech. Rep. D-54286, Trier, Germany.
- Avcioğlu, E. (2010). Hydrocarbon Microseepage Mapping via Remote Sensing for Gemrik Anticline, Bozova Oil Field, Adiyaman, Turkey. Ankara.
- AVIRIS Data Portal 2006-Present.(2015). aviris.jpl.nasa.gov. Retrieved 5 May 2015, from https://aviris.jpl.nasa.gov/alt_locator
- Baumgardner, M.F., Sylva, L.F., Biehl, L.L. and Stoner, E.R. (1985). Reflectance properties of soil. *Advances in Agronomy*, 38, 1-44. <https://doi.org/10.1016>
- Ben-Dor, E., Chabrillat, S., Demattê, J. A. M., Taylor, G. R., Hill, J., Whiting, M. L., & Sommer, S. (2009). Using Imaging Spectroscopy to study soil properties. *Remote Sensing of Environment*, 113, S38–S55. <https://doi.org/10.1016/j.rse.2008.09.019>
- Bian, Z., Inyang, H., Daniels, J., Otto, F., & Struthers, S. (2010). Environmental issues from coal mining and their solutions. *Mining Science and Technology (China)*, 20(2), 215-223. [http://dx.doi.org/10.1016/s1674-5264\(09\)60187-3](http://dx.doi.org/10.1016/s1674-5264(09)60187-3)
- Bioucas-Dias, J. (2009). A Variable Splitted Augmented Lagrangian Approach to Linear Spectral Unmixing. *IEEE*.

- Bolat, A. (2012). Adıyaman İli Kuzeyinin Jeolojisi ve Petrol Potansiyeli. Adana.
- Borgys, D., Kasen, I., Achard, V., & Perneel, C. (2012). Comparative evaluation of hyperspectral anomaly detectors in different types of background. SPIE Algorithms and Technologies for Multispectral, Hyperspectral, and Ultraspectral Imagery XVIII. Maryland.
- Clark, R. (1999). Spectroscopy of Rocks and Minerals, and Principles of Spectroscopy. speclab.cr.usgs.gov. Retrieved from <https://speclab.cr.usgs.gov/PAPERS.refl-mrs/refl4.html#section1.2>
- Cloutis, E. A. (1994). Spectral Reflectance Properties of Carbon-Bearing Materials. *Icarus*, 107(2), 276–287. <https://doi.org/10.1006/icar.1994.1023>
- Cloutis, E. A. (2003). Quantitative characterization of coal properties using bidirectional diffuse reflectance spectroscopy. *Fuel*, 82(18), 2239–2254. [https://doi.org/10.1016/s0016-2361\(03\)00209-6](https://doi.org/10.1016/s0016-2361(03)00209-6)
- Cozzolino, D., & Morón, A. (2003). The potential of near-infrared reflectance spectroscopy to analyse soil chemical and physical characteristics. *Journal of Agricultural Science*, 140(1), 65-71. <http://dx.doi.org/10.1017/s0021859602002836>
- Crosta, A., De Souza Filho, C., Azevedo, F., & Brodie, C. (2003). Targeting key alteration minerals in epithermal deposits in Patagonia, Argentina, using ASTER imagery and principal component analysis. *International Journal of Remote Sensing*, 24(21), 4233-4240.
- Daqi Xu, Guoqiang Nil, Tao Jiang, Lili Jiang, & Mingmin Chi. (2007). Integration of field work and hyperspectral data for oil and gas exploration. 2007 IEEE International Geoscience and Remote Sensing Symposium. <http://dx.doi.org/10.1109/igarss.2007.4423524>
- Davis, J. and Goadrich, M. (2006). The relationship between precision-recall and roc curves. *Proceedings of the 23 rd International Conference on Machine Learning*, 233-240
- Dirk Borghys, Ingebjorg Kåsen, Veronique Achard, & Christiaan Perneel. (2012). Comparative evaluation of hyperspectral anomaly detectors in different types of background.
- Dold, B. (2014). Evolution of Acid Mine Drainage Formation in Sulphidic Mine Tailings. *Minerals*, 4(3), 621–641. <https://doi.org/10.3390/min4030621>

- Du, Q., Ren, H., & Chang, C. (2003). A comparative study for orthogonal subspace projection and constrained energy minimization. *IEEE Transactions On Geoscience And Remote Sensing*, 41(6), 1525-1529. <http://dx.doi.org/10.1109/tgrs.2003.813704>
- EO-miners European Commission under the Environment Theme of the 7th Framework Programme for Research and Technological Development. (2013). *Eo-miners Final Report: Earth Observation for Monitoring and Observing Environmental and Societal Impacts of Mineral Resources Exploration and Exploitation*.
- Elowitz, M. (2015). What is Imaging Spectroscopy (Hyperspectral Imaging)? [markelowitz.com](http://www.markelowitz.com) Retrieved from: <http://www.markelowitz.com/Hyperspectral.html>
- Fischer, C., & Busch, W. (2002). Monitoring of environmental changes caused by hard-coal mining. In M. Ehlers (Ed.), *Remote Sensing for Environmental Monitoring, GIS Applications, and Geology*. SPIE. <https://doi.org/10.1117/12.453691>
- Freeman, H. (2003). Evaluation of the use of hyperspectral imagery for identification of microseeps near Santa Barbara, California. *Virginia*.
- Fu, B., Zheng, G., Ninomiya, Y., Wang, C., & Sun, G. (2007). Mapping hydrocarbon-induced mineralogical alteration in the northern Tian Shan using ASTER multispectral data. *Terra Nova*, 19(4), 225-231.
- He, Z., Deng, X., & Ai, S. (2014). Hydrocarbon Micro-seepage Anomalies Detection Algorithm Based on FPCS for Hyperspectral Remote Sensing Data. *Applied Mechanics and Materials*, 596, 457-462.
- Hörig, B., Kühn, F., Oschütz, F., & Lehmann, F. (2010). HyMap hyperspectral remote sensing to detect hydrocarbons. *International Journal of Remote Sensing*, 1413-1422.
- Hunt, G. (1977). Spectral signatures of particulate minerals in the visible and near infrared. *GEOPHYSICS*, 42(3), 501-513. <http://dx.doi.org/10.1190/1.1440721>
- Hunt, G., & Ashley, R. (1979). Spectra of altered rocks in the visible and near infrared. *Economic Geology*, 74(7), 1613-1629. <http://dx.doi.org/10.2113/gsecongeo.74.7.1613>
- Hwon, H., & Nasrabadi, N. (2004). Hyperspectral Target Detection Using Kernel Spectral Matched Filter. *IEEE Computer Society Conference on Computer Vision and Pattern Recognition Workshops (CVPRW'04)*.

- Irene C. Montero S., George H Brimhall, Charles N. Alpers, Gregg A. Swayze. (2005). Characterization of waste rock associated with acid drainage at the Penn Mine, California, by ground-based visible to short-wave infrared reflectance spectroscopy assisted by digital mapping. *Chemical Geology*, Volume 215, Issues 1–4, 2005, Pages 453–472. <https://doi.org/10.1016/j.chemgeo.2004.06.045>.
- Izawa, M. R. M., Applin, D. M., Norman, L., & Cloutis, E. A. (2014). Reflectance spectroscopy (350–2500nm) of solid-state polycyclic aromatic hydrocarbons (PAHs). *Icarus*, 237, 159–181. <https://doi.org/10.1016/j.icarus.2014.04.033>
- Rimstidt, J. D. & Vaughan, D. J. (2014). Acid Mine Drainage. Retrieved July 3, 2017, from <http://elementsmagazine.org/departments/mineralogy-matters/>
- Serranti, S., & Bonifazi, G. (2016). Hyperspectral imaging and its applications. In F. Berghmans & A. G. Mignani (Eds.), *Optical Sensing and Detection IV*. SPIE. <https://doi.org/10.1117/12.2234976>
- Johnston, D., Potter, H., Jones, C., Rolley, S., Watson, I., & Pritchard, J. (2008). Abandoned mines and water environment. Environment Agency.
- Jose M. Molero, Ester M. Garzón, Inmaculada Garcia, & Antonio J. Plaza. (2012). Anomaly detection based on a parallel kernel RX algorithm for multicore platforms. *Journal of Applied Remote Sensing*, 6, 061503-6–11.
- Karathanassi, V. (2014). Spectral Unmixing Evaluation for Oil Spill Characterization. *International Journal of Remote Sensing Applications*, 4(1), 1. <https://doi.org/10.14355/ijrsa.2014.0401.01>
- Keating, M. (2001). Cradle to grave: the environmental impacts from coal. Clean Air Task Force.
- Khan, S. (2006). Mapping Alteration Caused by Hydrocarbon Microseepages in Patrick Draw area Southwest Wyoming Using Image Spectroscopy and Hyperspectral Remote Sensing. Houston : Department of Geosciences, University of Houston.
- Keshava, N., & Mustard, J. F. (2002). Spectral unmixing. *IEEE Signal Processing Magazine*, 19(1), 44–57. <https://doi.org/10.1109/79.974727>
- Khan, S., & Jacobson, S. (2008). Remote sensing and geochemistry for detecting hydrocarbon microseepages. *GSA Bulletin*, 120(1/2), 96-105.

- King, T., & Clark, R. (1989). Reflectance Spectroscopy (0.2 to 20 microns) As An Analytical Method For The Detection of Organics. First International Symposium: Field Screening Methods for Hazardous Waste Site Investigations (pp. 485-488). EPA.
- Kopačková, V., Chevrel, S., Bourguignon, A., & Rojík, P. (2012). Application of high altitude and ground-based spectroradiometry to mapping hazardous low-pH material derived from the Sokolov open-pit mine. *Journal Of Maps*, 8(3), 220-230. <http://dx.doi.org/10.1080/17445647.2012.705544>
- Kruse, F., Lefkoff, A., Boardman, J., Heidebrecht, K., Shapiro, A., Barloon, B., & Goetz, A. (1993). The Spectral Image Processing System (SIPS) Interactive Visualization and Analysis of Imaging Spectrometer Data. *Remote Sensing of Environment*, 145-163.
- Kühn, F., Oppermann, K., & Hörig, B. (2004). Hydrocarbon Index-an algorithm for hyperspectral detection of hydrocarbons . *International Journal of Remote Sensing*, 25(3), 2467-2473.
- Landsat Surface Reflectance Level-2 Science Products | Landsat Missions. (2017). [Landsat.usgs.gov](https://landsat.usgs.gov). Retrieved 12 July 2017, from <https://landsat.usgs.gov/landsat-surface-reflectance-high-level-data-products>
- Li, J., & Bioucas-Dias, J. (2008). Minimum Volume Simplex Analysis: A Fast Algorithm to Unmix Hyperspectral Data. *IEEE*.
- Madhavi, T., Kalpana, M. S., Patil, D. J., & Dayal, A. M. (2011). Evidence for a relationship between hydrocarbon microseepage and trace metal anomalies: an implication for petroleum exploration. *Geosciences Journal*, 15(2), 197–206. <https://doi.org/10.1007/s12303-011-0015-y>
- Malpica, J., Alonso, M., & Rodriguez, B. (2011). Some Techniques for Anomaly Anomaly Detection in Hyperspectral Imageries. *ASPRS 2011 Annual Conference*.
- MicroImages Introduction to Hyperspectral Imaging. (2012). [microimages.com](http://www.microimages.com). Retrieved from: <http://www.microimages.com/documentation/Tutorials/hyrspec.pdf>
- Mielke, C., Boesche, N., Rogass, C., Kaufmann, H., Gauert, C., & de Wit, M. (2014). Spaceborne Mine Waste Mineralogy Monitoring in South Africa, Applications for Modern Push-Broom Missions: Hyperion/OLI and EnMAP/Sentinel-2. *Remote Sensing*, 6(8), 6790–6816. <https://doi.org/10.3390/rs6086790>

- MINEO Project. (2003). Assessing and monitoring the environmental impact of mining activities in Europe using advanced Earth Observation techniques. European Community Under the Information Society Technology Program.
- Monalokis, D., Lockwood, R., Cooley, T., & Jacobson, J. (2012). Is There a Best Hyperspectral Detection Algorithms? Proceedings of SPIE.
- Monalokis, D., Marden, D., & Shaw, G. (2003). Hyperspectral Image Processing for Automatic Target Detection Applications. Lincoln Laboratory Journal, 4(1).
- Murphy, R. J., & Monteiro, S. T. (2013). Mapping the distribution of ferric iron minerals on a vertical mine face using derivative analysis of hyperspectral imagery (430–970nm). ISPRS Journal of Photogrammetry and Remote Sensing, 75, 29–39. <https://doi.org/10.1016/j.isprsjprs.2012.09.014>
- Naim, A., & Alsharhan, A. (1997). Sedimentary Basins and Petroleum Geology of the Middle East. Amsterdam: Elsevier Science B.V.
- Nascimento, J. (2005). Vertex Component Analysis: A Fast Algorithm to Unmix Hyperspectral Data. IEEE Transactions on Geoscience and Remote Sensing, 43(4).
- Nasrabadi, N. (2014). Hyperspectral Target Detection. IEEE Signal Processing Magazine, 34-44.
- Petrovic, A., Khan, S., & Chafetz, H. (2008). Remote detection and geochemical studies for finding hydrocarbon-induced alterations in Lisbon Valley, Utah. Marine and Petroleum Geology, 25, 696-705.
- Reed, I., & Yu, X. (1990). Adaptive multiple-band CFAR detection of an optical pattern with unknown spectral distribution. IEEE Transactions on Acoustics, Speech, and Signal Processing, 38(10), 1760-1770
- Ren, H., & Chang, C. (2003). Automatic spectral target recognition in hyperspectral imagery. IEEE Transactions On Aerospace And Electronic Systems, 39(4), 1232-1249. <http://dx.doi.org/10.1109/taes.2003.1261124>
- Riaza, A., Buzzi, J., García-Meléndez, E., Vázquez, I., Bellido, E., Carrère, V., & Müller, A. (2011). Pyrite mine waste and water mapping using Hymap and Hyperion hyperspectral data. Environmental Earth Sciences, 66(7), 1957–1971. <https://doi.org/10.1007/s12665-011-1422-0>

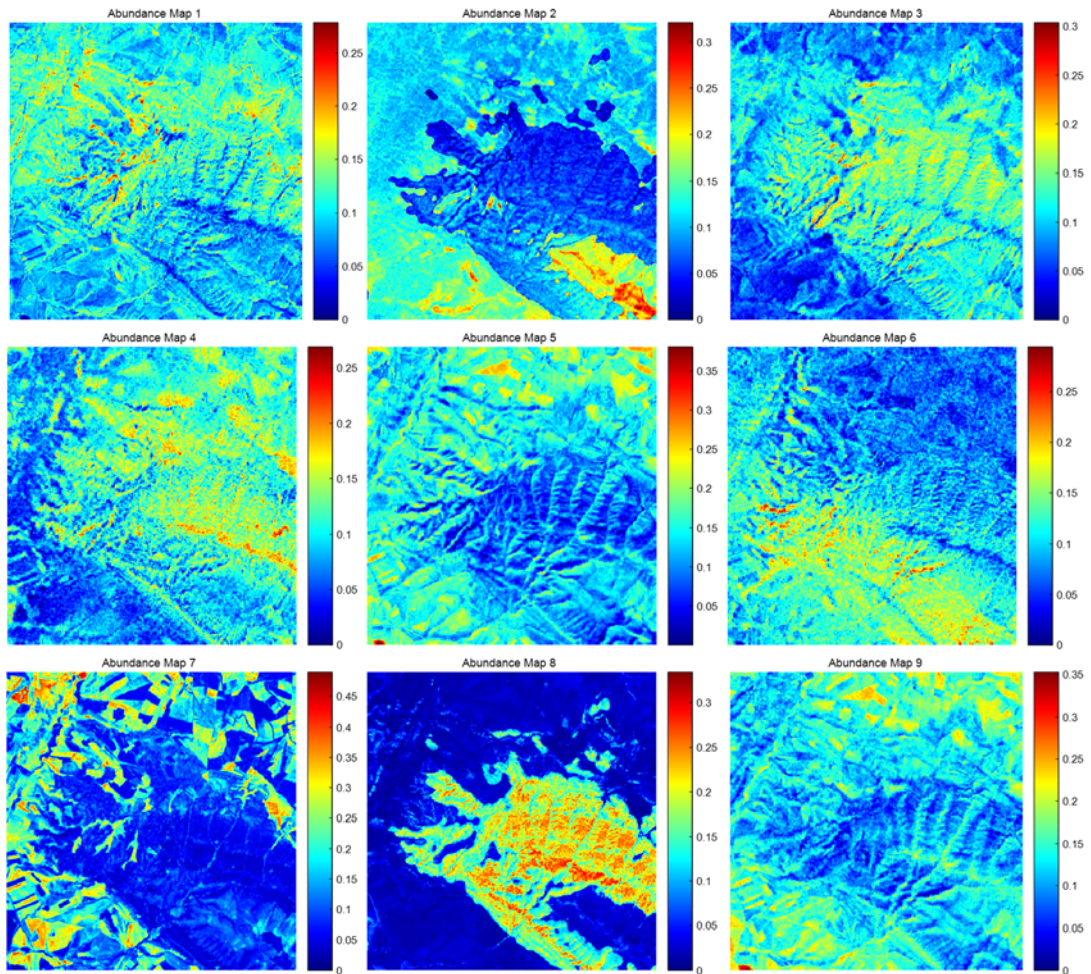
- Richter, N., Staenz, K., & Kaufmann, H. (2008). Spectral unmixing of airborne hyperspectral data for baseline mapping of mine tailings areas. *International Journal of Remote Sensing*, 29(13), 3937–3956. <https://doi.org/10.1080/01431160801891788>
- Roper W.E. & Dutta S. (2006). Oil Spill and Pipeline Condition Assessment using Remote Sensing & Data Visualization Management Systems. Freshwater Spills Symposium 2006.
- Rycroft, M. J. (2013). Electromagnetic Radiation Principles and Concepts as Applied to Space Remote Sensing. In *Handbook of Satellite Applications* (pp. 667–681). Springer New York. https://doi.org/10.1007/978-1-4419-7671-0_38
- Salati, S., van Ruitenbeek, F., van der Meer, F., & Naimi, B. (2014). Detection of Alteration Induced by Onshore Gas Seeps from ASTER and WorldView-2 Data. *Remote Sensing*, 6, 3188-3209.
- Salem F. and Kafatos P.M. (2001). Hyperspectral image analysis for oil spill mitigation. *Proc. ACRS 2001—22nd Asian Conference on Remote Sensing*, vol. 1, 748–753, November 5–9. SPIE Algorithms and Technologies for Multispectral, Hyperspectral, and Ultraspectral Imagery XVIII (Vol. 8390, p. 83902J–8390–12). Retrieved from <http://dx.doi.org/10.1117/12.920387>
- Salem F., Kafatos M., El-Ghazawi T., Gomez R., Yang R. (2002). Hyperspectral image analysis for oil spill detection. *Aviris Proceedings of the Airborne Visible/Infrared Imaging Spectrometer Workshop 2002*. Retrieved from <https://aviris.jpl.nasa.gov/proceedings>
- Sánchez España, J., López Pamo, E., Santofimia, E., Aduvire, O., Reyes, J., & Baretino, D. (2005). Acid mine drainage in the Iberian Pyrite Belt (Odiel river watershed, Huelva, SW Spain): Geochemistry, mineralogy and environmental implications. *Applied Geochemistry*, 20(7), 1320-1356. <http://dx.doi.org/10.1016/j.apgeochem.2005.01.011>
- Schumacher, D. (1996). Hydrocarbon-Induced Alteration of Soils and Sediments. In D. Schumacher, & M. Abrams (Eds.), *Hydrocarbon migration and its nearsurface expression* (pp. 71-89).
- Sentinel-2 European Space Agency (ESA). (2015). Sentinel-2 User Handbook. Retrieved from https://sentinels.copernicus.eu/web/sentinel/user-guides/document-library/-/asset_publisher/xlslt4309D5h/content/sentinel-2-user-handbook

- Shi, P., Bihong, F., & Ninomiya, Y. (2010). Mapping Hydrocarbon Seepage-Induced Anomalies in the Arid Region, West China Using Multispectral Remote Sensing. *International Archives of the Photogrammetry, Remote Sensing and Spatial Information Science*. Tokyo.
- Smailbegovic, A., Gray, K., Johnson, K., Murphy, V., & Holbrook, R. (2009). Spectroscopic and hyperspectral evaluation of possible hydrocarbon occurrences in estuarine sediments, North Charleston, South Carolina, USA. In *2009 First Workshop on Hyperspectral Image and Signal Processing: Evolution in Remote Sensing*. IEEE. <https://doi.org/10.1109/whispers.2009.5289037>
- SpecTIR Advanced Hyperspectral & Geospatial Solutions. (2015). Spectir.com. Retrieved 8 February 2015, from <http://www.spectir.com/free-data-samples>
- Swayze, G. A., Clark R.N., Pearson, R.M., and Livo, K.E. (1996) Mapping acid generating minerals at the California Gulch Superfund Site in Leadville, Colorado using imaging spectroscopy, *Summaries of the Sixth Annual JPL Airborne Earth Science Workshop, JPL Publication 96-4, vol.1, March 4-8, p. 231-234*. Retrieved from https://aviris.jpl.nasa.gov/proceedings/workshops/96_docs/34.PDF
- Swayze, G. A., Smith, K. S., Clark, R. N., Sutley, S. J., Pearson, R. M., Vance, J. S., Roth, S. (2000). Using Imaging Spectroscopy To Map Acidic Mine Waste. *Environmental Science & Technology*, 34(1), 47-54. <https://doi.org/10.1021/es990046w>
- Taşkesen B., Beşbınar B., Koz A., Alatan A. (2017). Aşırı Bölütleme ve Ortak Bilgi ile Uydu Görüntülerinde Güdümsüz Değişiklik Tespiti. 25. Sinyal İşleme ve İletişim Uygulamaları Kurultayı, 15-18 May 2017, Antalya.
- Taylor, M. (2017). NASA Landsat Science. [Landsat.gsfc.nasa.gov](https://landsat.gsfc.nasa.gov). Retrieved 10 July 2017, from <https://landsat.gsfc.nasa.gov/about/technical-information>
- Twinning Project Report. (2014). Technical Assistance for Mining Waste Management Project. Ministry of Environmental Affairs of Turkey.
- van der Meer, F., van Dijk, P., van der Werff, H., & Yang, H. (2002). Remote sensing and petroleum seepage: a review and case study. *Terra Nova*, 14, 1-17.
- Velez-Reyes, M. (2007). Hyperspectral Imaging or Imaging Spectroscopy: An Overview. cohemis.uprm.edu. Retrieved from http://cohemis.uprm.edu/prysig/pdfs/pres_mvelez07.pdf

- Viscarra Rossel, R., Bui, E., de Caritat, P., & McKenzie, N. (2010). Mapping iron oxides and the color of Australian soil using visible–near-infrared reflectance spectra. *Journal of Geophysical Research*, 115(F4). <http://dx.doi.org/10.1029/2009jf001645>
- Winkelmann, H. (2005). On the Applicability of Imaging Spectrometry for the Detection and Investigation of Contaminated Sites with Particular Consideration Given to the Detection of Fuel Hydrocarbon Contaminants in Soil. (Unpublished doctoral dissertation). Faculty of Environmental Sciences and Process Engineering, Brandenburg University of Technology, Cottbus, Germany.
- Winter, M. (1999). N-FINDR: an algorithm for fast autonomous spectral end-member determination in hyperspectral data. *SPIE Imaging Spectrometer*. Denver, Colorado.
- Yazar, B. (2009). Adıyaman-Kahta Güneyi (Çalgan-Karaköprü-Alıdağ) Mardin Grubu Karbonatlarının Yeraltı Jeolojisi ve Petrol İmkanlarının İncelenmesi. Ankara.
- Zare-Baghbidi, M., & Homayouni, S. (2013). Fast hyperspectral anomaly detection for environmental applications. *Journal of Applied Remote Sensing*, 7(1), 073489. <http://dx.doi.org/10.1117/1.jrs.7.073489>

APPENDIX A

SISAL ALGORITHM - REPRESENTATIVE ABUNDANCE MAPS FOR HYDROCARBON MICROSEEPAGE – (ASTER)



APPENDIX B

TRACE ELEMENT LEVELS OF COLLECTED SOIL SAMPLES

X	Y	Z	Iron (CP)	Copper (CP)	Zinc (CP)	Manganese (CP)	Lead (CP)	Nickel (CP)	Chromium (CP)	Arsenic (CP)	Molybdenum (CP)
34.07838	40.76637	1234.7	23012.40	32.03	49.68	829.08	1.59	359.40	274.68	11.84	6.49
34.07734	40.76550	1245	20237.05	25.74	42.15	377.45	1.54	170.62	118.39	4.33	3.24
34.07781	40.76341	1262	19165.45	28.11	45.87	824.05	3.91	64.41	55.19	2.46	2.79
34.07327	40.76340	1299	19997.10	39.30	49.95	811.19	3.37	137.68	72.52	<DL	1.88
34.07216	40.76344	1297	24235.65	70.92	67.98	458.22	5.68	155.26	116.47	5.43	2.29
34.07093	40.76425	1304	21087.95	31.05	49.90	476.35	4.38	126.65	86.89	5.15	2.55
34.07072	40.76470	1310	20014.20	26.01	43.38	452.28	2.16	138.19	120.55	3.18	2.94
34.07036	40.76558	1297	21244.45	32.64	54.37	567.49	4.70	135.09	88.28	4.73	2.53
34.06914	40.76527	1290	22526.35	34.56	56.38	550.89	5.27	154.58	104.66	5.11	2.59
34.06777	40.76439	1290	19768.00	47.61	71.45	294.75	3.74	187.66	109.32	1.36	2.48
34.06838	40.76322	1301	20987.00	30.17	48.77	556.55	4.80	134.86	96.97	4.08	2.42
34.06910	40.76302	1295	19510.400	34.31	50.04	462.20	3.85	139.64	76.54	1.47	1.94
34.07858	40.76609	1233.6	21991.650	37.36	57.84	451.33	4.64	167.46	110.40	3.12	2.58
34.07589	40.76390	1272	23269.750	49.52	63.84	593.07	6.93	137.55	95.90	5.68	2.55
34.07309	40.76341	1291.5	21387.350	30.69	53.21	587.75	3.44	140.89	133.27	4.32	2.82
34.07033	40.76333	1279	21824.650	44.02	56.88	609.84	5.03	133.77	85.20	2.25	3.08
34.07079	40.76264	1302	20626.200	27.32	49.19	476.74	3.11	151.96	130.87	4.22	3.24
34.07127	40.76483	1312.8	22125.350	27.87	58.47	431.90	52.39	163.76	124.99	5.83	3.12
34.07541	40.76499	1287.3	24545.700	42.13	72.24	645.57	6.12	146.52	126.11	6.58	2.70
34.07627	40.76773	1264	23440.600	43.21	67.4	513.30	6.51	130.05	96.56	7.07	2.75
34.07623	40.76802	1264.3	22044.400	46.8	63.25	302.66	6.63	129.41	80.61	3.12	2.78
34.07281	40.76255	1302	24345.000	34.19	53.99	279.36	3.11	135.53	188.9	4.92	2.22
34.07719	40.76731	1258.2	21964.200	35.75	57.35	469.96	5.14	143.48	113.63	1.83	2.21
34.07790	40.76591	1236	22455.000	38.55	61.05	554.39	4.2	181.91	139.62	3.61	2.48
34.07778	40.76328	1269	18914.750	12.5	34.3	475.63	<DL	89.48	147.41	3	2.46
34.08076	40.76225	1273	21610.450	24.23	47.79	523.78	1.8	162.4	154.55	3.39	2.54
34.07948	40.76436	1280.5	22649.200	42.63	65.48	581.19	6.38	127.91	88.33	<DL	2.69
34.07887	40.76803	1290.1	2255.900	40.98	62.98	270.43	9.75	87.55	69.29	6.79	2.49
34.07669	40.76965	1281.3	23092.750	33.19	55.55	471.72	4.44	129.68	132	5.96	2.45
34.07378	40.77141	1299.6	18854.850	28.58	31.92	168.73	2.4	75.07	79.35	6.04	2.87
34.07220	40.77304	1298.9	19372.600	29.27	45.06	541.99	3.17	133.49	95.38	<DL	2.14
34.06964	40.77111	1297.2	22419.150	40.26	58.07	521.11	4.79	174.88	118.76	2.84	2.63
34.06929	40.76795	1265.2	19939.850	27.82	51.23	501.73	4.02	127.1	87.26	3	2.42
34.06942	40.76806	1261.8	20567.550	27.65	48.47	466.69	2.87	161.9	122.04	2.97	2.38
34.07101	40.76740	1268	22611.700	34.84	55.74	719.11	3.56	170.32	129.35	4.48	3.08
34.06815	40.76624	1268.4	20879.150	23.04	48.72	396.4	2.18	153.14	118.6	2.31	2.85

CURRICULUM VITAE

PERSONAL INFORMATION

Surname, Name: Soydan, Hilal
Nationality: Turkish
Email: soydan.hilal@gmail.com

EDUCATION

Degree	Institution	Graduation
PhD	METU Mining Engineering	2017
MS	METU Mining Engineering	2013
BS	METU Mining Engineering	2010

WORK EXPERIENCE

Fulbright Scholar, Researcher, Remote Sensing Laboratory of Lamont Doherty Earth Observatory, Columbia University in the City of New York, USA, 2016 – 2017.

Research Assistant, Middle East Technical University, Assistantship of Rock Mechanics, Reclamation and Mine Closure, Mine System Analysis, Mine Design Courses, November 2010 -2017.

Researcher, Middle East Technical University, Scientific Research Project, Investigation of Archeological Remains with Hyperspectral Images, 2015 - 2016
Researcher, HAVELSAN/ ANKARA, Advanced Imaging Techniques, Hyperspectral Image Analysis, April 2014 – 2016.

Researcher, Middle East Technical University Center for Image Analysis, Hyperspectral Image Analysis and Algorithm Development, August 2014 - 2016
Researcher, Santez Project, Hyperspectral Image Processing and Object Classification, April 2013 – 2015.

Researcher, Middle East Technical University, Scientific Research Project, Identification of Asphalt Characteristics with Hyperspectral Images, 2013 – 2015.

Researcher, Cayeli Copper Enterprises Project, Landslide Susceptibility Assessment of Cayeli Region with GIS Analysis and Numerical Analysis, Rize, 2012-2014.

Internship in Underground Mining Operations, Çayeli Copper Enterprises-Inmet Mining, Rize – Turkey, 2007.

Intern at Gold Processing Plant, Tuprag Metal Mining Company- Eldorado Gold Corporation, Usak – Turkey, 2008

FOREIGN LANGUAGES

Advanced English, Intermediate Russian

PUBLICATIONS

1. Hilal Soydan, H. Şebnem Düzgün, Evaluation of Soil Moisture Content Using Aster and Worldview 2 Imageries, IEEE International Geoscience and Remote Sensing Symposium (IGARSS) 2014.
2. Hilal Soydan, Alper Koz, H. Şebnem Düzgün, and A. Aydın Alatan, A Comparative Study of Hyperspectral Anomaly and Signature Based Target Detection Methods for Oil Spills, Submitted to IEEE WHISPERS 7th Workshop on Hyperspectral Image and Signal Processing 2015.
3. Hilal Soydan, H. Şebnem Düzgün, Analysis of Land Use Land Cover Changes for an Abandoned Mine Site, Submitted to IEEE International Geoscience and Remote Sensing Symposium (IGARSS) 2015.
4. Okan Bilge Özdemir, Hilal Soydan, Yasemin Yardımcı, H. Şebnem Düzgün, Signature Based Vegetation Detection with Hyperspectral Images, Submitted to IEEE SIU Signal Processing and Communication Applications 2015.
5. Alper Koz, Hilal Soydan, H. Sebnem Duzgun, Aydin Alatan, A Local Extrema Based Method on 2D Brightness Temperature Maps For Detection of Archaeological Artifacts, IEEE International Geoscience and Remote Sensing Symposium (IGARSS) 2016.
6. Hilal Soydan, Alper Koz, H. Sebnem Duzgun, Aydin Alatan, Total Carbon Mapping With Hyperspectral Unmixing Techniques, IEEE WHISPERS 8th Workshop on Hyperspectral Image and Signal Processing 2016.
7. Hilal Soydan, Alper Koz, H. Sebnem Duzgun, Spatio-Temporal Anomaly Detection For Environmental Impact Assessment: A Case of an Abandoned Coal Mine Site in Turkey, Submitted to SPIE Optics & Photonics Proceedings 2017.
8. Hilal Soydan, Alper Koz, H. Şebnem Düzgün, Identification of Hydrocarbon Microseepage Induced Alterations with Spectral Target Detection and Unmixing Algorithms, (Submitted to International Journal of Applied Earth Observation and Geoinformation, 2017)